

VINÍCIUS GERMANOS CLEANTE

**An Investigation into Harvesting Energy from Sleeper
Vibration Due to a Passing Train**

**Uma Investigação sobre Extração de Energia a partir de Vibração no
Dormente devido a um Trem Passante**

**Ilha Solteira
2019**

An Investigation into Harvesting Energy from Sleeper Vibration Due to a Passing Train

**Uma Investigação sobre Extração de Energia a partir de Vibração no
Dormente devido a um Trem Passante**

Vinícius Germanos Cleante

Thesis presented to the Faculdade de Engenharia - UNESP - campus of Ilha Solteira as part of the requirements for obtain the title of Doctorate in Mechanical Engineering.

Knowledge area: Solid Mechanics.

Prof. Dr. Michael John Brennan

Adviser

Prof. Dr. Gianluca Gatti

Co-adviser

FICHA CATALOGRÁFICA

Desenvolvido pelo Serviço Técnico de Biblioteca e Documentação

C623a Cleante, Vinícius Germanos.
An investigation into harvesting energy from sleeper vibration due to a passing train uma investigação sobre extração de energia a partir de vibração no dormente devido a um trem passante / Vinícius Germanos Cleante. -- Ilha Solteira: [s.n.], 2019
146 f. : il.

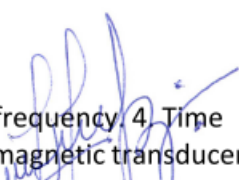
Tese (doutorado) - Universidade Estadual Paulista. Faculdade de Engenharia de Ilha Solteira. Área de conhecimento: Mecânica dos Solos, 2019

Orientador: Michael John Brennan

Co-orientador: Gianluca Gatti

Inclui bibliografia

1. Sleeper vibration. 2. Train vibration. 3. Trainload frequency. 4. Time waveform replication. 5. Compensator filter. 6. Electromagnetic transducer. 7. Linear energy harvester.



João Josué Barbosa
Serviço Técnico de Biblioteca e Documentação
Diretor Técnico
CRB 8-5642

CERTIFICADO DE APROVAÇÃO

TÍTULO DA TESE: An Investigation into Harvesting energy from Sleeper Vibration due to a Passing Train

AUTOR: VINÍCIUS GERMANOS CLEANTE

ORIENTADOR: MICHAEL JOHN BRENNAN

COORIENTADOR: GIANLUCA GATTI

Aprovado como parte das exigências para obtenção do Título de Doutor em ENGENHARIA MECÂNICA, área: Mecânica dos Sólidos pela Comissão Examinadora:

Prof. Dr. MICHAEL JOHN BRENNAN 
Departamento de Engenharia Mecânica / Faculdade de Engenharia de Ilha Solteira - UNESP

Prof. Dr. DOUGLAS DOMINGUES BUENO 
Departamento de Matemática / Faculdade de Engenharia de Ilha Solteira - UNESP

Prof. Dr. JOAO ANTONIO PEREIRA 
Departamento de Engenharia Mecânica / Faculdade de Engenharia de Ilha Solteira - UNESP

Prof. Dr. CARLOS DE MARQUI JUNIOR 
Departamento de Engenharia de Materiais, Aeronáutica e Automobilística / Universidade de São Paulo/São Carlos

Prof. Dr. PAULO JOSÉ PAUPITZ GONÇALVES 
Departamento de Engenharia Mecânica / Faculdade de Engenharia de Bauru

Ilha Solteira, 05 de dezembro de 2019

ACKNOWLEDGEMENT

I would like to thank Professor Mike Brennan for his guidance in this Thesis. His support, advices and questions were helpful for the development of this Thesis. I am truly thankful for your teachings.

I would like to thank my parents, Cleiton and Maria, my sister, Mariana, and my nephew, João Vítor. There are no words to describe how grateful I am. Their support and motivations, mainly at the difficult moments, encouraged me to follow the way to achieve my goals.

I would like to thank Professor Gianluca Gatti for his co-supervision. Also, for the period of my research internship in the Università della Calabria. Your support and discussions had a significant contribution to this Thesis.

I would like to thank my friends from the Group of Intelligent Materials and Systems (GMSInt) and from the Mechanical Engineering Department in Ilha Solteira. I also would like to thank some special friends, Andreyson and Carol, Bruce, Oscar and Lucas Rangel and Lucas Rhea for their support and friendship.

Finally, I would also like to thank the Coordination for the Improvement of Higher Education Personnel (CAPES) for the scholarship during the PhD, Finance Code 001. Also, part of this work was conducted during a visiting scholar period at Università della Calabria sponsored by the Capes Foundation within the Ministry of Education, Brazil (PDSE, grant 19/2016).

*“Somewhere, something incredible is waiting
to be known.”*

Carl Sagan

ABSTRACT

The advances in microelectromechanical systems to power supply devices for monitoring the structural integrity, mainly for applications in remote areas or with difficult access, have made energy harvesting from ambient vibration a highly researched topic. Although several electromechanical mechanisms have been proposed for applications in a variety of fields, harvesting energy from railway track vibrations is relatively new, and only a small amount of research is ongoing in this topic. This thesis aims to determine the factors that govern the sleeper vertical vibration induced by a passing train, develop a methodology to emulate this vibration in a laboratory-based system and to derive a model of a load resistance attached to a linear electromagnetic transducer to determine the optimum energy harvested. The study shows the importance of knowing the vibration behaviour of the sleeper in order to tune the energy harvester to the correct excitation frequency. A comparison between piezoelectric and electromagnetic transducers is performed using a two-port network model to determine which transducer performs better for low frequency vibration. To emulate sleeper vibration due to a passing train using an electrodynamic shaker, a compensator filter is designed to remove the system dynamics. An analytical investigation into the energy dissipated by a load resistance attached to an electromagnetic transducer when subject to a time-limited base excitation, which may include the transient and steady-state responses, is carried out and compared with numerical analysis. This is validated with an experimental test in the laboratory-based system. This work has shown that in order to harvest the maximum energy from the vibrating source, the electromagnetic transducer must operate in the transient regime and its natural frequency should be tuned to the frequency with the largest acceleration amplitude. This was found to be achieved only using an ideal transducer. When the device is operating in a regime which may include or be only the steady-state, due to the internal coil resistance or, mainly, due to the mechanical damping, the transducer may perform better when the natural frequency is tuned to the frequency with the largest velocity amplitude. For the case studied in this work, from the sleeper vertical vibration induced due to the passage of an Inter-city train travelling at Steventon site, the 3rd trainload frequency has the largest velocity amplitude and the 7th trainload frequency has the largest acceleration amplitude.

Keywords: Sleeper vibration. Train vibration. Trainload frequency. Time waveform replication. Compensator filter. Electromagnetic transducer. Linear energy harvester.

RESUMO

Avanços em sistemas micro eletromecânico para fornecer energia à dispositivos para monitoramento de integridade estrutural, principalmente para aplicações em áreas remotas ou de difícil acesso, fez de extração de energia a partir de vibrações contidas no ambiente um tópico de pesquisa em destaque. Apesar de que diversos mecanismos eletromecânicos já foram propostos em uma variedade de aplicações, extração de energia à partir de vibrações em linhas férreas é, relativamente, novo e somente algumas pesquisas estão sendo realizadas sobre esse tópico. Esta Tese busca determinar os fatores que governam a vibração vertical do dormente induzida devido a passagem de um trem, desenvolver uma metodologia para emular esta vibração em um sistema em laboratório e derivar um modelo para um transdutor linear eletromagnético com uma carga resistiva acoplada. O estudo mostrou a importância de conhecer o comportamento vibracional do dormente de modo a sintonizar o extrator de energia com a frequência correta de excitação. Uma comparação entre transdutores piezoelétrico e eletromagnético é realizado utilizando um modelo quadripolo para determinar qual transdutor tem um melhor desempenho para vibrações em baixa frequência. Para emular a vibração do dormente devido a passagem de um trem em um agitador eletrodinâmico, um filtro compensador é projetado para remover a dinâmica do sistema. Uma investigação analítica da energia dissipada pela carga resistiva acoplada à um transdutor eletromagnético quando sujeito a excitação na base de tempo limitado, no qual possa incluir as respostas transiente e permanentes, é realizada e comparada com a análise numérica. Isso é validado com um experimento em um sistema em laboratório. Neste trabalho foi mostrado que para extrair à máxima energia de uma fonte de vibração, o transdutor eletromagnético deve operar no regime permanente e a sua frequência natural deve ser sintonizada com a frequência com a maior amplitude de aceleração. Foi mostrado que isso só ocorreria se um transdutor ideal fosse utilizado. Quando o dispositivo opera em um regime que possa incluir ou ser somente o regime estacionário, devido aos efeitos da resistência interna da bobina ou, principalmente, devido ao fator de amortecimento mecânico, o transdutor possa operar melhor quando sua frequência natural fosse sintonizada com a frequência com a maior amplitude de velocidade. Para o caso estudado neste trabalho, a partir da vibração vertical do dormente induzida devido a passagem de um Inter-city 125 viajando em Steventon, a 3ª frequência de carga do trem possui a maior amplitude de velocidade e a 7ª frequência de carga do trem possui a maior amplitude de aceleração.

Palavras chaves: Vibração do dormente. Frequência da carga do trem. Replicação da forma da onda no tempo. Filtro compensador. Transdutor eletromagnético. Extrator de energia linear.

LIST OF FIGURES

Figure 1	(a) example of the railway track structure; (b) a simplified model of the track structure consisting of an Euler-Bernoulli infinite beam on a Winkler foundation subject to a concentrated load; and (c) example of the load applied by each wheel of a carriage.	33
Figure 2	Sleeper vibration due to the passage of one wheel (blue solid line, —) one bogie (red dash dot line, - · -); and one carriage (black dotted line, · · ·). The column (a) is the time history (at the top there is another axis corresponding to the non-dimensional position); and (b) normalized spectrum for: (i) displacement; (ii) velocity; and (iii) acceleration.	37
Figure 3	Sleeper vertical vibration induced by an Inter-city 125 at speed of 200 km/h: (a) velocity, ••• (blue dotted line) is the full time-history, — (red solid line) is a period corresponding to the passage of a single carriage (at the top of the graph there is an axis indicating the carriages: P ₁ and P ₂ are the power cars and 1-8 are the passenger carriages); (bi-iii) zoom-in of the comparison of displacement, velocity and acceleration, respectively, between measurement (blue solid line, —) and model (black dashed line, •••); and (c) comparison between Fourier coefficients of sleeper vertical acceleration of measurement (blue circle, ●); standard deviation range from the eight passenger carriages (red line, —); and model (black square, □).	39
Figure 4	Comparison of sleeper vertical vibration between measurement (blue solid line, —) and model (black dotted line, •••) due to the passage of: a) Pendolino at speed of 200 km/h; b) Supervoyager at speed of 202 km/h; c) Turbostar at speed of 103 km/h; and d) Electrostar at speed of 109 km/h. (i) denotes displacement; (ii) velocity; and (iii) acceleration.	42
Figure 5	Comparison between Fourier coefficients of sleeper vertical acceleration of measurement (blue circle, ●); and model (black square, □) for: (a) Pendolino at 195 km/h; (b) Supervoyager at 202 km/h; (c) Turbostar at 103 km/h; and (d) Electrostar at 109 km/h.	43
Figure 6	Sleeper non-dimensional vertical acceleration spectrum, for $\alpha = 20$ normalized by the maximum amplitude of one wheel induced deflection due to the passage of: one	

	wheel, red solid line —; one bogie (divided by two), blue dashed line - -; one carriage (divided by four), green thin line -; and infinite train of carriages, black circle ○. The curves were scaled to fit the same envelope.	46
Figure 7	Sleeper non-dimensional vertical acceleration spectrum normalized by the maximum amplitude of one wheel induced deflection due to the passage of: one wheel, red solid line —; one bogie (divided by two), blue dashed line - -; one carriage (divided by four), green thin line -; and infinite train of carriages, black circle ○. The curves were scaled to fit the same envelope. (a) softer support stiffness, $\alpha = 14.7$; and (b) stiffer support stiffness, $\alpha = 28$	47
Figure 8	The combination of a base-excited SDOF mass-spring-damper system.	50
Figure 9	Example of a force excited SDOF mass-spring-damper system.	51
Figure 10	Example of the non-dimensional device impedance (a) and mobility (b) for two different mechanical damping ratio: $\zeta_m = 0.001$ (blue solid line, —); and $\zeta_m = 0.1$ (red dotted line, ···). The black dash-dot line, - · -, is the mass line and the black dashed line, - - -, is the stiffness line.	53
Figure 11	Schematic of a two-port model of a transducer	54
Figure 12	The equivalent electrical circuit of the transducer connected to an electrical load.	55
Figure 13	Equivalent mechanical model for the transducer connected to an electrical load.	57
Figure 14	Example of an electromagnetic energy harvesting transducer.	64
Figure 15	Energy harvester subject to time-limited harmonic excitation.	66
Figure 16	Normalized electrical energy dissipated by the load resistance as a function of ζ_R for $\pi n \zeta_{eq} \gg 1$ ($\zeta_m = 0.2$, $\zeta_{R_0} = 0.008$ and $n = 56$). Red dashed line, - - -, is the asymptote given by $\hat{E}_{elec} \approx \frac{\pi n \zeta_R \zeta_{R_0}}{\zeta_m}$; black dotted line, ···, is the asymptote given by $\hat{E}_{elec} \approx \frac{\pi n \zeta_{R_0}^2}{\zeta_R (\zeta_m + \zeta_{R_0})^2}$; and the vertical magenta dash-dotted line, - · -, is the for $\zeta_{R,opt} = \frac{\zeta_m \zeta_{R_0}}{\zeta_m + \zeta_{R_0}}$	69
Figure 17	(a) Maximum normalized energy dissipated by the optimum load resistance damping ratio; and (b) The corresponding optimum load resistance damping ratio as a function of the internal coil resistance and the mechanical damping ratios for $n = 56$ cycles.	71

Figure 18	(a) Maximum normalized energy dissipated by the optimum load resistance damping ratio as a function of the internal resistance damping ratio. (b) The corresponding optimum load resistance damping ratio as a function of the internal resistance damping ratio for $\zeta_m \ll 1$ and $n = 56$ cycles. Red dashed line, $- -$, is the asymptote for $\zeta_{R_o} \ll 1$; and black dotted line, \cdots , is the asymptote for $\zeta_{R_o} \gg 1$. 73
Figure 19	Energy dissipated by each transducer element normalized by the maximum energy available considering $n = 56$ cycles, $\zeta_{R_o} = 0.74$ and: (a) $\zeta_m = 0$; (b) $\zeta_m = \frac{1}{8\pi n}$; (c) $\zeta_m = \frac{1}{\pi n}$; and (d) $\zeta_m = 0.01$. The black dash-dot line, $- \cdot -$, is the total energy available, the blue solid line, $—$, is the energy dissipated by the load resistance; the red dashed line, $- -$, is the energy dissipated by the internal coil resistance; the green dotted line, \cdots , is the energy dissipated by the mechanical damping. 78
Figure 20	Scheme of the proposed compensator filter..... 81
Figure 21	Example of a linear diagram of a single input and a single output signal. 82
Figure 22	Example of the segment averaging method procedure without overlapping. 83
Figure 23	Example of rectangular (blue solid line) and Hanning (red dashed line) window effect in: (a) time; and (b) frequency domains. 85
Figure 24	Spectrum comparison of rectangular (blue line) and hanning (red line) windows for two window periods: T_w (thick solid line); and $2T_w$ (dashed line). 86
Figure 25	Example of the system dynamic identification considering 50% of overlap and $q = 40$ averages (black dashed line, $- -$) and $q = 5$ averages (blue solid line, $—$): a) estimator H ; and b) coherence. 89
Figure 26	Example of the IRF , $h(n)$, for two number of averages: $q = 40$ (black dashed line, $- -$); and $q = 5$ (blue solid line, $—$). 89
Figure 27	Example of the pre-processing of the system impulse response function: a) before pre-processing, $h(n_t)$; and b) after the pre-processing, $\hat{h}(n_t)$. The blue solid line ($—$) is the impulse response function; and the red dashed line ($- -$) is the applied window. 91
Figure 28	Example of the postprocessing procedure: a) <i>hanning</i> window application; and b) the remove of the introduced lag. 93
Figure 29	Schematic of the input signal with the system compensation. 93

Figure 30	The experiment setup.....	94
Figure 31	The estimated system <i>FRF</i> : a) Mobility; b) phase; and c) coherence.	96
Figure 32	The <i>IRF</i> mobility of the experiment setup #1 system: (a) the full time-history; (b) the zoom-in.	97
Figure 33	The compensator filter with 10s delay: (a) full time-history; and (b) a zoom-in.	97
Figure 34	Test of the compensator filter: (a) input compensated signal; and (b) time-history comparison between desired (black solid line, —), and system response (magenta dotted line, - -) time waveforms.....	98
Figure 35	The magnitude ratio between desirable and system response time waveforms. ...	99
Figure 36	Waveforms comparisons of the vertical sleeper velocity and acceleration, due to the passage of 8 passenger carriages of the Inter-city 125 train at a speed of 200 km/h, between desirable (blue solid line, —) and measured on the shaker (black dashed line, - -): (a) time-history; and (b) spectral density.....	101
Figure 37	Spectrum ratio between desirable and measured shaker acceleration due to the passage of 8 passenger carriages of the Inter-city 125 train at a speed of 200 km/h.	102
Figure 38	Waveforms comparisons of the vertical sleeper velocity and acceleration, due to the passage of 8 passenger carriages of the Inter-city 125 train at a speed of 100 km/h, between desirable (blue solid line, —) and measured on the shaker (black dashed line, - -): (a) time-history; and (b) spectrum.	103
Figure 39	Magnitude ratio between desirable and measured acceleration spectrums due to the passage of 8 Inter-city 125 passenger carriages at a speed of 100 km/h.	103
Figure 40	Comparison between desirable, blue solid line, and measured, black dashed line, time waves of the sleeper vertical velocity (.1) and acceleration (.2) due to the passage of 8 Inter-city 125 passenger carriages at speed of 200 km/h without the compensator filter: (a) time-history; and (b) spectrum.....	104
Figure 41	Spectrum ratio between desirable and measured acceleration time waves due to the passage of 8 Inter-city 125 passenger carriages at speed of 100 km/h without the compensator filter: (a) magnitude; and (b) phase.	105

- Figure 42 (a) Time-history and (b) power spectral density (PSD) of the sleeper vertical acceleration induced due to the passage 10 passenger carriages of an Inter-city 125 at a speed of 196 km/h (.1) and 118 km/h (.2)..... 109
- Figure 43 (a) Time-history and (b) Fourier coefficients of the sleeper vertical velocity (.1) and acceleration (.2) due to the passage of 10 passenger carriages of an Inter-city 125 at a speed of 118 km/h. The black dotted line is the complete time-history and the blue solid line correspond to the vibration due to the passage of the 4th carriage. 110
- Figure 44 Results for each natural frequency of two electromagnetic energy harvester devices when subjected to a base vibration induced by the sleeper vertical vibration due to the passage of 10 passenger carriages of an Inter-city 125 travelling at Steventon site with a speed of 118 km/h. Device 1, (.1), comprises of $m=0.011$ kg, $\zeta_m=0$ and $R_o=0$ Ω ; Device 2, (.2), comprises of $m=0.011$ kg, $\zeta_m=0$ and $R_o=369$ Ω . (a) The maximum energy dissipated; (b) the optimum load resistance damping ratio; (c) the corresponding load resistance; and (d) the resulting relative displacement. The blue solid line denotes the numerical results and the black circles denote the analytical results. At the top of each graph is shown a second horizontal axis which corresponds to the trainload frequencies. 115
- Figure 45 Results for each natural frequency of two electromagnetic energy harvester devices when subjected to a base vibration induced by the sleeper vertical vibration due to the passage of 10 passenger carriages of the Inter-city 125 travelling at Steventon site with a speed of 118 km/h. Device 3, (.3), comprises of $m=1$ kg, $\zeta_m=0$ and $R_o=0$ Ω ; Device 4, (.4), comprises of $m=1$ kg, $\zeta_m=0$ and $R_o=369$ Ω . (a) The maximum energy dissipated; (b) the optimum load resistance damping ratio; (c) the corresponding load resistance; and (d) the resulting relative displacement. The blue solid line denotes the numerical results and the black circles denote the analytical results. At the top of each graph is shown a second horizontal axis which corresponds to the trainload frequencies. 118
- Figure 46 Results for each natural frequency of the electromagnetic energy harvester device 5, when subject to a base vibration induced by the sleeper vertical vibration due to the passage of 10 passenger carriages of the Inter-city 125 at a speed of 118 km/h: (a) the maximum energy dissipated; (b) the optimum load resistance damping ratio; (c) the corresponding load resistance; and (d) the resulting relative displacement.

	The blue solid line denotes the numerical results and the black circle denotes the analytical results. At the top of each graph is presented a second horizontal axis which corresponds to the trainload frequencies.....	121
Figure 47	The schematic of the experimental setup.....	122
Figure 48	(a) Example of the Geophone SM-24 and (b) Frequency Response Function (FRF) between the voltage across the geophone terminals and its base velocity. Blue solid line (—) is the FRF obtained experimentally and the black dashed line (- -) is the FRF obtained from the optimum curve fitting.....	123
Figure 49	The sleeper vertical acceleration induced due to the passage of an Inter-city 125 train travelling at Steventon site with the speeds of (a) 117.32 km/h and (b) 273.5 km/h. The black dotted line (.....) is the complete time-history and the blue solid line (—) comprises only the excitation period.	125
Figure 50	The energy harvester results with an attached load resistance of $R_l = 1944 \Omega$ when subjected to sleeper vibration induced by an Inter-city 125 passing train with a speed of 117.2 km/h: (a) the voltage across the load resistance and (b) the relative displacement The black dotted line (.....) is the complete time-history and the blue solid line (—) comprises only the excitation period.	127
Figure 51	The energy harvester results with an attached load resistance of $R_l = 1144 \Omega$ when subjected to sleeper vibration induced by an Inter-city 125 passing train with a speed of 273.5 km/h: (a) the voltage across the load resistance and (b) the relative displacement. The black dotted line (.....) is the complete time-history and the blue solid line (—) comprises only the excitation period.	128
Figure 52	Time waveform replication of the sleeper vertical velocity induce due to an Inter-city 125 passing with the speed of 117.3 km/h. (a) The compensated excitation signal and (b) the desired shaker velocity (blue solid line, —) and the measured shaker velocity (black dashed line, - -).....	129
Figure 53	Time waveform replication of the sleeper vertical velocity induced due to the passage on an Inter-city 125 with a speed of 273.5 km/h. (a) The compensated excitation signal and (b) the desired shaker velocity (blue solid line, —) and the measured shaker velocity (black dashed line, - -).....	130

Figure 54	The schematic of the energy harvester electrical circuit to scavenge the maximum energy for the train with a speed of (a) 117.3 km/h with a $R_{l,eq} = 1903 \Omega$ and (b) 273.5 km/h with a $R_{l,eq} = 1173 \Omega$	131
Figure 55	The voltage across the optimum load resistance, $R_{l,eq} = 1903 \Omega$, when the energy harvester is subjected to the sleeper vertical vibration induced due to an Inter-city 125 train passing with the speed of 117.3 km/h. The black solid line (—) is the voltage predicted by the numerical investigation and the blue dotted line (.....) is the measured.	132
Figure 56	The voltage across the optimum load resistor, $R_{l,eq} = 1173 \Omega$, when the energy harvester is subjected to the sleeper vertical vibration induced due to an Inter-city 125 train passing with the speed of 273.5 km/h. The black solid line (—) is the voltage predicted by the numerical investigation and the blue dotted line (.....) is the measured.	132
Figure A1	Sleeper vertical acceleration (a) time-history; and (b) Power Spectral Density (at the top there is another axis corresponding to frequency normalized by the ratio between train speed and passenger carriage) due to the passage of an Inter-city 125 at different speeds: (i) 162 km/h; (ii) 178 km/h; (iii) 195 km/h; and (iv) 200 km/h.	147

LIST OF TABLES

Table 1	Characteristics of the measurement sites	34
Table 2	Train parameters.	36
Table 3	Calculated support stiffness and train load for five different trains.....	43
Table 4	The element impedance.	50
Table 5	Train parameters.	100
Table 6	Characteristics railway track at Steventon site.	100
Table 7	Characteristics railway track at Steventon site.	108
Table 8	Train parameters.	109
Table 9	The electromagnetic energy harvester parameters.....	112
Table 10	Results for the energy harvester with $m = 0.011\text{kg}$ at the natural frequency corresponding to the 7 th trainload frequency.....	116
Table 11	Results for the electromagnetic energy harvester with $m = 1\text{kg}$ at the natural frequency corresponding to the 7 th trainload frequency.....	119
Table 12	Results for the electromagnetic energy harvester with a heavy mechanical damping at the natural frequencies corresponding to the 3 rd and the 7 th trainload frequencies.	120
Table 13	The Geophone SM-24 specification.	124
Table 14	The numerical results for the Geophone SM-24 as the energy harvesting device when its base is subjected by the vibration induced due to the passage of an Inter-city 125 at Steventon site.	126
Table 15	The harvested energy by the linear electromagnetic transducer subject to the sleeper vibration due to a passing train emulated in a laboratory-based system.....	132

LIST OF SYMBOLS

Roman symbols

B_r	Window bandwidth resolution
c_{c_m}	Critical mechanical damping
c_e	Analogue equivalent electrical damping
c_{eq}	Equivalent damping
c_m	Mechanical damping
C_p	Piezoelectric internal capacitance
d_i, \hat{d}_i	Dimensional and non-dimensional distance between the 1 st and the i -th wheel
\hat{E}_{ava}	Non-dimensional energy available from the source
E_{coil}, \hat{E}_{coil}	Energy and Non-dimensional energy dissipated by the internal coil resistance
E_{elec}, \hat{E}_{elec}	Energy and Non-dimensional harvested by the load resistance
E_{mec}, \hat{E}_{mec}	Energy and Non-dimensional dissipated by the mechanical damping
EI	Flexural stiffness of the rail
F	Driving acting force
\hat{f}_{bogie}	Frequency normalized by the ratio between train speed and bogies distance
\hat{f}_{car}	Trainload frequency
F_s	Frequency sample
\hat{f}_{wheel}	Frequency normalized by the ratio between train speed and wheels distance in a bogie
h	Impulse response function
H	Estimator H – Frequency response function
\hat{h}	Pre-processed impulse response function
\bar{h}	Impulse response function of the compensator filter transfer function
\bar{H}	Compensator filter transfer function
h_c, h_{cd}	Compensator filter without and with time delay adjust
\bar{h}_c	Post-processed compensator filter
h_t	Truncated circle-shifted impulse response function
i	Current
I, I_c	Amplitude of current and closed-circuit current
k	Spring (stiffness)
$k_{support}$	Support stiffness per unit of the sleeper length

k_{trackbed}	Trackbed stiffness per unit of the sleeper length
k_{pad}	Pad stiffness
L_{bogie}	Distance between bogies centre on a carriage
L_{car}	Carriage length
L_o	Electromagnetic internal inductance
L_{sleeper}	Sleeper length
L_{wheel}	Distance between wheelsets in a bogie
m	Mass
n	Number of cycles
N	Number of points
N_d	Number of points delayed
N_r	Number of points of the q -th segmented sequence
n_t	Discrete time
N_t	Number of truncate samples
P_M, \hat{P}_M	Power and non-dimensional power dissipated by the electromagnetic transducer
P_P, \hat{P}_P	Power and non-dimensional power dissipated by the piezoelectric transducer
P_r	Ratio between the powers dissipated by the piezoelectric and electromagnetic transducers
P_t	Power dissipated by the transducer
q	Number of segmented sequences
R	Ratio between spectrums of the measured and the desirable time waveforms
$R_{x_{in}x_{in}, i}$	Autocorrelation
R_t	Load resistance
R_o	Internal coil resistance
S	Train speed
$S_{x_{in}x_{in}}$	Auto periodogram without noise contribution (Power spectral density)
$\hat{S}_{x_{in}x_{in}, i}$	Auto periodogram of the q -th segmented sequence
$\tilde{S}_{x_{in}x_{in}}$	Average auto periodogram (Power spectral density)
$\tilde{S}_{x_{in}x_{out}}$	Cross periodogram (Cross-spectral density)
t, \hat{t}	Time and non-dimensional time
t_d	Time delay

T_r	Time duration of the q -th segmented sequence
T_w	Window time duration
U	Normalized window constant
$v (V)$	Voltage across the transducer terminals (Amplitude)
$v_l (V_l)$	Voltage across the load (Amplitude)
$x_b, \dot{x}_b, \ddot{x}_b$	Base displacement, velocity and acceleration
\dot{X}_b	Amplitude of the base velocity
X_d	Amplitude of the desirable time waveform
\dot{X}_D	Amplitude of the device velocity
x_{ic}	Desirable time waveform
$x_{in} (X_{in})$	Input signal (Amplitude)
$x_m, \dot{x}_m, \ddot{x}_m$	Suspended mass displacement, velocity and acceleration
\dot{X}_m	Amplitude of the suspended mass velocity
X_{mes}	Amplitude of the measured time waveform
$x_{out} (X_{out})$	System output – measured system response (Amplitude)
$x_r, \dot{x}_r, \ddot{x}_r$	Relative displacement, velocity and acceleration
\dot{X}_r	Amplitude of the relative velocity
\dot{X}_S	Amplitude of the source velocity
w	Rail deflection
$w_{\text{sleeper}}, \hat{w}_{\text{sleeper}}$ (\hat{W}_{sleeper})	Dimensional and non-dimensional sleeper deflection (Amplitude)
Y_D	Device mobility
Z_c	Mechanical damping impedance
Z_D	Device impedance
Z_D^I, Z_D^E	Open-circuit and closed-circuit device impedances
Z_e	Internal electric impedance (blocked electrical impedance)
Z_k	Mechanical stiffness impedance
Z_l	Load impedance
Z_m	Mechanical mass impedance
Z_M	Electromagnetic energy harvester impedance
Z_{me}, Z_{em}	Electromechanical transducer impedances
Z_P	Piezoelectric energy harvester impedance
Z_S	Source impedance
Z_t	Transducer impedance

Z_α	Electrical impedance on the transducer
W_{win}	Amplitude of the window

Greek symbols

α	Non-dimensional characteristic length
β	Characteristic length
δ	Dirac delta function
γ_{xy}^2	Coherence function
$\eta, \bar{\eta}$	Phase and non-dimensional phase
$\phi, \bar{\phi}$	Phase and non-dimensional phase
ρ	Lag
τ	Non-dimensional time
τ_o, τ_e	Initial and final non-dimensional excitation time
ω	Angular frequency
ω_d	Damped natural frequency
ω_n	Undamped natural frequency
Ω	Non-dimensional excitation frequency
ζ_e	Analogue equivalent electrical damping ratio
ζ_{eq}	Equivalent damping ratio
ζ_m	Mechanical damping ratio
ζ_R	Load resistance damping ratio (analogous electrical load resistance damping ratio)
ζ_{R_o}	Internal coil resistance damping ratio (analogous electrical internal coil resistance damping ratio)

Other symbols

*	Complex conjugate
j	$\sqrt{-1}$ (complex number)
$\text{Im}\{\dots\}$	Imaginary part
$\text{Re}\{\dots\}$	Real part

CONTENT

1	INTRODUCTION	23
1.1	BACKGROUND.....	23
1.2	LITERATURE REVIEW	24
1.2.1	<i>Energy harvesting from the railway track environmental.....</i>	<i>24</i>
1.2.1.1	Rotational energy harvester	24
1.2.1.2	Piezoelectric energy harvester	25
1.2.1.3	Electromagnetic energy harvester	27
1.2.1.4	Linear energy harvester oscillator	28
1.3	THESIS OBJECTIVES	29
1.4	CONTRIBUTIONS TO KNOWLEDGE	29
1.5	THESIS OUTLINE.....	30
2	SLEEPER VIBRATION DUE TO A PASSING TRAIN.....	32
2.1	INTRODUCTION	32
2.2	MODEL OF SLEEPER VIBRATIONS DUE TO A PASSING TRAIN	33
2.3	COMPARISON OF THE MODEL WITH EXPERIMENTAL DATA	38
2.3.1	<i>Description of the experimental data</i>	<i>38</i>
2.4	SIMULATIONS USING THE MODEL	40
2.5	DISCUSSION	44
2.6	CONCLUSIONS	48
3	ENERGY HARVESTING: TIME-LIMITED PERIODIC EXCITATION	49
3.1	INTRODUCTION	49
3.2	THE MECHANICAL IMPEDANCE OF A SINGLE-DEGREE-OF-FREEDOM MASS-SPRING-DAMPER BASE EXCITATION SYSTEM	50
3.3	THE TWO-PORT NETWORK: A MODEL FOR A PIEZOELECTRIC AND AN ELECTROMAGNETIC TRANSDUCER.....	53
3.3.1	<i>Equivalent Electrical System.....</i>	<i>55</i>
3.3.2	<i>Equivalent Mechanical System.....</i>	<i>56</i>
3.3.2.1	Piezoelectric transducer	57
3.3.2.2	Electromagnetic transducer	58

3.3.3	<i>The electrical power dissipated by the transducer</i>	59
3.3.3.1	Electrical power dissipated by the piezoelectric energy harvester	60
3.3.3.2	Electrical power dissipated by the electromagnetic energy harvester	60
3.3.3.3	Comparison between the power dissipated by piezoelectric and electromagnetic energy harvesting devices.....	61
3.4	ELECTROMAGNETIC DEVICE: BASE EXCITED MASS-SPRING-DAMPER LINEAR OSCILLATOR	62
3.4.1	<i>Existing model</i>	63
3.4.2	<i>Energy dissipated by the load resistance</i>	67
3.4.2.1	Time-limited periodic excitation: steady-state condition	68
3.4.2.2	Time-limited periodic excitation: transient plus steady-state response.....	71
3.4.3	<i>The energy dissipated by the internal coil resistance</i>	76
3.4.4	<i>The dissipated mechanical energy</i>	76
3.4.5	<i>The total energy available</i>	77
3.5	CONCLUSIONS	78
4	THE RAILWAY TRACK VIBRATION EMULATED IN A LABORATORY BASED SYSTEM	80
4.1	INTRODUCTION	80
4.2	TIME WAVEFORM REPLICATION: COMPENSATOR FILTER	81
4.2.1	<i>The identification of the system dynamics</i>	82
4.2.1.1	Direct method: Welch's periodogram estimator	83
4.2.1.2	Direct method: The modified Welch's periodogram (overlapped averaging) estimator..	85
4.2.1.3	The estimator H : the system identification for non-deterministic input and output signal.....	87
4.2.1.4	Coherence: the degree of correlation between signals	88
4.2.1.5	The identification of the system dynamics: example	88
4.2.2	<i>Design of the compensator filter</i>	89
4.2.2.1	Preprocessing.....	90
4.2.2.2	The compensator filter transfer function design.....	91
4.2.2.3	Post-processing.....	92
4.2.3	<i>Design of the compensated input signal</i>	93

4.3	THE LABORATORY-BASED SYSTEM FOR THE SLEEPER TIME WAVEFORM REPLICATION ...	94
4.3.1	<i>The laboratory-based system setup</i>	94
4.3.2	<i>The signal generator</i>	95
4.3.3	<i>The compensator filter</i>	95
4.3.3.1	The identification of the system dynamics	95
4.3.3.2	The design of the compensator filter	97
4.3.3.3	The time waveform replication: simulation.....	97
4.3.4	<i>The sleeper vertical vibration waveform replication</i>	99
4.3.4.1	The model of the sleeper vertical vibration	99
4.3.4.2	The train and railway track parameters: the Inter-city 125 high-speed train passing-by Steventon site, United Kingdom (UK)	100
4.3.4.3	The experiment: Inter-city 125 train passing at speed of 200 km/h with the compensator filter	100
4.3.4.4	Inter-city 125 train passing at speed of 100 km/h	102
4.3.4.5	Inter-city 125 train passing at speed of 200 km/h without the compensator filter	104
4.4	CONCLUSIONS	105
5	HARVESTING ENERGY FROM THE VIBRATION INDUCED DUE TO A PASS-BY TRAIN.....	107
5.1	INTRODUCTION	107
5.2	THE SLEEPER VERTICAL VIBRATION AS THE SOURCE OF THE ENERGY HARVESTING DEVICE BASE EXCITATION.....	108
5.3	THE LINEAR SINGLE-DEGREE-OF-FREEDOM ELECTROMAGNETIC ENERGY HARVESTER.....	111
5.3.1	<i>Optimization of a linear electromagnetic energy harvester</i>	111
5.3.2	<i>Analytical investigation</i>	112
5.3.2.1	Device with no mechanical damping and no internal coil resistance.....	112
5.3.2.2	Device with no mechanical damping and with an internal coil resistance.....	113
5.3.2.3	Device with heavy mechanical damping and with an internal coil resistance	114
5.3.3	<i>Passing train results</i>	114
5.3.3.1	Results for Group 1: transducers with a suspended mass $m = 0.011$ kg and no mechanical damping	114
5.3.3.2	Results for Group 2: transducers with a suspended mass $m = 1$ kg and no mechanical damping	117

5.3.3.3	Results for Group 3: electromagnetic energy harvester with a heavy mechanical damping	119
5.4	HARVESTING ENERGY FROM THE RAILWAY TRACK VIBRATION.....	122
5.4.1	<i>The experimental setup</i>	122
5.4.2	<i>The geophone</i>	123
5.4.3	<i>Harvesting energy from the sleeper vibration induced due to a pass-by train: numerical</i>	125
5.4.3.1	The vibrating source	125
5.4.3.2	Numerical optimization and energy harvested	126
5.4.4	<i>Harvesting energy from the sleeper vibration induced due to a passing train: experiment</i>	128
5.4.4.1	The sleeper vibration time waveform replicated on the electromagnetic shaker	129
5.4.4.2	The electrical circuit	130
5.4.4.3	The harvested energy from the sleeper vibration emulated on an electromagnetic shaker.....	131
5.5	CONCLUSIONS	133
6	FINAL REMARKS	135
6.1	RECOMMENDATION FOR FUTURE WORK	136
	REFERENCES	138
	APPENDIX A	146

1 INTRODUCTION

1.1 BACKGROUND

Energy harvesters are devices which convert a given type of energy into electrical energy. Studies in this subject have been carried out for many years. In the beginning, the aim was to bring comfort in human life, supplying houses with electrical energy. Today, the technology has fixed its roots deep in society. Electric and electromechanical devices have become part of the human being daily life, from the simple to the most difficult tasks. This has increased the global demand for electrical energy, and it is expected to increase by 57% by 2050 (BLOOMBERGNEF, 2018). The seek to overcome the global energy demand, together with attempts to address issue related to climate change, have made energy harvesting a highlight topic.

There are 4 types of energy sources which can provide a small or large amount of electrical energies: thermal; photovoltaic; radio waves; and kinetic energy. Thermal sources provide energy from the temperature difference between two materials (JIA; LIU, 2009). Photovoltaic sources provide energy from solar radiation and indoor illumination (HIROKANE *et al.*, 2010). Radio waves provide energy from the microwaves presented in the ambient (MARIAN *et al.*, 2012). Using an antenna, these micro electromagnetic waves are captured and rectified into an alternating voltage (HEMOUR *et al.*, 2014). Kinetic energy is a great potential energy source due to its presence in almost every type of environment. Hydro-electric power plants (POBERING; SCHWESINGER, 2004) and wind power plants (MORAIS *et al.*, 2008) are examples of such kinetic sources, which can provide a large amount of energy. Ocean waves and tides (KHALIGH; ONAR, 2010) are other examples, however they can provide less energy than the previous ones. Energy from ambient vibration is another example of kinetic source (STEPHEN, 2006a). Although the scale of generated energy is small, due to several applications, this particular source has increased the attention of researchers.

Harvested energy from ambient vibration has become an alternative way to power microelectromechanical systems (MEMS), which require a low power to operate, like wireless sensors (AVCI *et al.*, 2018; KULAH; NAJAFI, 2008; LI; JANG; TANG, 2014a; LU *et al.*, 2015; SARI; BALKAN; KULAH, 2007), which can be implemented in remote places or in places with difficult access (IANNACCI, 2017), e.g., to supply energy for medical implants

(DAGDEVIREN *et al.*, 2014; MIAO *et al.*, 2006), especially for pacemakers (AMIN KARAMI; INMAN, 2012).

Another example of the applicability of energy harvested from ambient vibrations is to supply energy to devices for monitoring the integrity of structures to reduce maintenance costs, mainly in remote areas. Such devices have been extensively applied in bridges (HARMS; SEDIGH; BASTIANINI, 2010; HU; WANG; JI, 2013), buildings (YUN *et al.*, 2020), vehicles (LYNCH, 2006) and others. Recently, due to railway track expansion, together with the increase in the railway line speeds, the undesirable vibrations in railways are now seen as a potential source to supply power to devices that monitor rail integrity (MIAN, 2013) to increase safety and passenger comfort.

1.2 LITERATURE REVIEW

1.2.1 Energy harvesting from the railway track environmental

Harvesting energy from the railway environment to supply power to micro electromechanical devices to monitor the structural integrity, warning signal lights, etc., has increased the amount of research in this topic. Investigations into energy harvesting from sunlight, using photovoltaic panels installed at the centre of a sleeper (GREENRAIL, 2020), harvesting energy from the wind induced due to the passage of a train (WANG *et al.*, 2017), or from suspension of the train (DE PASQUALE; SOMÀ; ZAMPIERI, 2012) are examples of applications which have been carried out. However, it is the energy from the railway track vibration which has gained more attention, mainly, because it still has a small number of published papers on this topic. From the track vibrations, two transducer mechanisms are highlighted: rotational energy harvester; and the resonator energy harvester. More details about the devices for harvesting energy from vibration in railway has been reviewed in (ULIANOV *et al.*, 2020).

1.2.1.1 Rotational energy harvester

Rotational energy harvesters are devices that scavenge energy from the track displacement. Generally, using gears and rack-pinions, the vertical displacement of the track is

converted into rotational motion using a mechanical motion rectifier (MMR) (PAN *et al.*, 2019), which uses a rotating permanent magnet DC generator (PMDC) to generate electrical energy.

One of the first research groups to introduce this mechanism was Nelson *et al.* (2009), who proposed a mechanical energy harvester using rack-pinion mechanism to harvest energy from the sleeper vertical deflection during downward motion. During upward motion, the shaft freewheels. Experimental tests carried out by Hansen *et al.* (2010) showed that a load resistance of 37.3Ω was capable to harvest an average power of 0.22 W from 12.7 mm of sleeper deflection due to the passage of a loaded train with a speed of 18.4 km/h. From 3.2 mm of the sleeper deflection due to the passage of an unloaded train with a speed of 21.6 km/h, an average power of 10 mW was harvested.

Pourghodrat *et al.* (2011) improved the mechanism proposed in (NELSON *et al.*, 2009) by harvesting energy from, both, downward and upward sleeper deflection and by replacing the planetary gearbox by one with a ratio of 1:100 to increase the speed at which the shaft rotates. Simulations showed that the improved mechanism was able to harvest a maximum power output of 215 W for a loaded train passing with the speed of 88 km/h. Later, Pourghodrat *et al.* (2014) introduced a hydraulic and a cam-based mechanisms to harvested energy from the small sleeper deflections induced due to the passage of an unloaded train.

Wang *et al.* (2013) investigated the use of an energy harvester consisting of a single shaft rack-pinion to convert the bi-directional sleeper deflection to a unidirectional rotational motion and a flywheel to regulate the shaft speed. The disadvantage of this device is that it must be anchored into the ballast material. To overcome this, Lin *et al.* (2018) proposed the use of an adjustable threaded rod with pre-compressed springs to support the energy harvesting device and maintain the base plate stationary. Field tests have shown that this device was capable to harvest an average power of 6.9 W using a load resistance of 50Ω in Delta connection from a sleeper deflection of 5.7 mm induced due to a freight train passing with the speed of 64 km/h.

1.2.1.2 Piezoelectric energy harvester

Piezoelectric transducers are devices that when stimulated electrically, their structure responds with a physical deformation (indirect piezoelectric effect). Also, when they undergo mechanical deformation, they generate an electrical charge. Common piezoelectric materials are made from ceramics or polymers (ANTON; SODANO, 2007). Polymer based transducers

have a low cost and are highly flexible. However, it is the ceramic materials, like lead-zirconate-titanate (PZT), that have higher piezoelectric coefficients.

A cantilever beam is the most commonly used structure for an energy harvesting application using a piezoelectric transducer. A small layer of piezoelectric material is applied to one of the beam surfaces. This model is known as a unimorph piezoelectric harvester (YI; SHIH; SHIH, 2002). If the same material is applied to two surfaces, this is known as a bimorph piezoelectric harvester (ANTON; SODANO, 2007; ERTURK; INMAN, 2009; ROUNDY; WRIGHT; RABAEY, 2003).

Nelson *et al.* (2008) investigated the use of a piezoelectric transducer attached to the bottom of the rail to harvest energy from the vertical vibration induced by loaded and unloaded freight trains. Experimental tests showed good agreement with simulations. A load resistance of 387 k Ω was capable to harvest an average power of 0.053 mW when subject to vibration induced due to a train passing with the speed of 24 km/h.

Gao *et al.* (2016) investigated two cantilever beam piezoelectric transducers connected in parallel. They were installed at the bottom of the rail to harvest energy from excitation frequencies of 5 to 7 Hz induced due to a passenger train carriage with the speed of 250 km/h. Experimental tests using the piezoelectric energy harvester with a natural frequency of 23 Hz, showed that the device was capable of achieving a peak-to-peak power of 4 mW and a peak-to-peak of 22.1 V with a load resistance of 100 k Ω .

With the aim to harvest energy from a range of frequencies, Wischke *et al.* (2011) investigated the use of a piezoelectric array to broaden the frequency band of actuation and with a load capacitor attached to the transducer to store the energy. The device, installed at the top of a railway tunnel sleeper, consists of 4 piezoelectric cantilever beams connected in parallel, each of them with different tip mass, whose natural frequency is of 437 Hz, 461 Hz, 480 Hz and 498 Hz. Field tests showed that when subject to vibration induced by the passage of 497 trains with different speeds, the energy harvester was capable of harvesting an average of 395 μ J of energy per train. Li *et al.* (2014b) investigated the use a piezoelectric array which consists of 6 piezoelectric cantilever beam connected in series to broaden the frequency range to 55 to 75 Hz.

Tianchen *et al.* (2014) investigated the use of an array of 16 drums piezoelectric transducer connected in parallel. The device was installed under the sleeper to harvest the vibration induced due to the passage of a metro train with a speed of 60 km/h. Simulation and

experimental tests in laboratory, considering a test rig of scale 1:10 to the real track, showed that a load resistance of 3.9 k Ω was able to harvest a power of 0.1 W.

Wang *et al.* (2015) investigated the performance of two piezoelectric transducers, both installed at the bottom of the rail, to harvest vibration induced due to passing trains. One consisted of a piezoelectric patch-type installed to harvest energy from the longitudinal rail strain and the other was a piezoelectric stack-type to harvest the transversal track displacement. Simulations showed that the faster and heavier the train, the more energy is harvested by both devices. When subject to vibration induced by a train passing with the speed of 108 km/h, the patch-type and the stack-type piezoelectric devices were capable to harvest 0.214 mJ and 0.05 mJ of energy respectively with a corresponding load resistances of 211 k Ω and 180 k Ω .

1.2.1.3 Electromagnetic energy harvester

Electromagnetic transducers are mechanical devices that follow the principle of Faraday's law (STEPHEN, 2006a), where the relative motion between a coil and a magnet generates a voltage. The structure of an electromagnetic energy harvester essentially consists of a coil, a magnet and a spring. One of the first studies of energy harvesting using this technology was by Williams and Yates (1996). Amirtharajah *et al.* (1998) later enhanced the efficiency of an electromagnetic transducer.

Nelson *et al.* investigated the use of a voice coil attached to the bottom of the rail to harvest energy from the vertical vibration induced due to the passage of loaded and unloaded freight trains. Laboratory tests using an electrodynamic shaker to excite the voice coil showed that for a load resistance of 7.5 Ω and under 10 Hz sinusoidal excitation, a maximum average power of 0.146 mW was observed. In field tests, an average power of 4mW was harvested from an unloaded train travelling with a speed of 18 km/h and an average of 12 mW was harvested from a loaded train travelling with a speed of 21 km/h.

Gao *et al.* (2017) investigated the use of a linear electromagnetic energy harvester with copper-beads. The proposed device offered an approach to evaluate different natural frequencies under low-frequency excitation. A dc-dc boost converter is also proposed, and the experimental test has shown that the device operating in its resonance frequency of 6 Hz was able to harvest a maximum power output of 120 mW with a load resistance of 45 Ω .

Hadas *et al.* (2018) investigated an electromagnetic energy harvester operating with a natural frequency of 17 Hz. Experimental tests were performed in the laboratory by mounting

the device on an electrodynamic shaker and attaching different load resistance. The real measurements of the sleeper vibration induced due to the passage of several trains were used to excite the electrodynamic shaker. Results showed that an average output power of 2 mW per train was harvested by the device.

Wang *et al.* (2019) investigated the use of an elastic lever beam to magnify the sleeper vibration induced to the linear electromagnetic transducer. Simulations showed an increase in output power by a factor of 430. Although it was found that this mechanism slightly increases the wheel-rail contact force, a significant negative effect on rail vibration was not observed.

1.2.1.4 Linear energy harvester oscillator

With the aim to investigate the fundamentals of an oscillator when subject to vibrations induced by passing trains and to draw a strategy to maximize the performance of an energy harvesting device, some authors have investigated the potential energy harvested from the vibrating source using a linear single-degree-of-freedom mass-spring-damper oscillator.

Gatti *et al.* (2016) derived an approximate analytical expression considering a time-limited excitation source to investigate the potential mechanical energy available when subject to the vibration induced by a passing train. The analysis showed that the device should have a small damping ratio and the natural frequency should be targeted to the frequency with the largest acceleration amplitude. For the case studied, when the sleeper vibration was induced by an Inter-city 125 train composed of 2 power carriages and 8 passenger carriages passing with the speed of 195 km/h, the device natural frequency should be target to 17 Hz and would be capable to harvest a total of 0.25 J/kg with a damping ratio of 0.0045.

Cleante *et al.* (2016) extended the analyse carried out in (GATTI *et al.*, 2016) and evaluated the performance of a single oscillator when subject to vibrations induced by trains passing with different speeds. Using an approximate expression to determine the acceleration amplitude of the sleeper deflection due to trains passing with a range of speeds from 190 km/h to 200 km/h, the device target frequency and the potential energy harvested have been determined. The investigation showed that the device natural frequency should be 16.57 Hz, at which correspond to a train with the speed of 196 km/h, to harvest a total of 1.1 J/kg of energy.

Brennan and Gatti (2017a) extended the analyse carried out in (GATTI *et al.*, 2016) and investigated the contribution of the free vibration to the total harvested energy when a linear mass-spring-damper oscillator is subjected to a vibrating source with a time-limited excitation.

It was found that when the device is optimally designed, more energy is harvested in the forced phase of vibration than from the free phase of vibration. Depending on the number of the excitation cycles and the harvester damping ratio, more energy is harvested from the free phase of vibration, however, it will result in a large relative displacement.

1.3 THESIS OBJECTIVES

The objectives of this Thesis are to:

- Derive an analytical model involving the train and the track system to predict the resulting sleeper vertical vibration of the railway track in the time and frequency domains;
- Investigate why the sleeper vibration is larger at some frequencies than others;
- Determine the best transduction mechanism to harvest energy from the low frequency sleeper vibrations induced by a passing train;
- Derive, in the time domain, an analytical model of a linear single-degree-of-freedom electromagnetic energy harvester;
- Investigate the effects of the transducer parameters of an electromagnetic energy harvester on its performance;
- Design a laboratory-based system that can emulate the railway track vibrations;
- Determine the optimal linear electromagnetic energy harvester parameters to scavenge the maximum energy from the sleeper vibration induced due to a passing train;
- Use the laboratory-based system to investigate how much energy can be harvested from the sleeper vibrations due to a passing train;

1.4 CONTRIBUTIONS TO KNOWLEDGE

The contributions of this thesis are as follows:

- The factors that govern the maximum vertical acceleration of the sleeper vibration have been determined. This contribution was published in (Cleante *et al.*, 2019);
- Improvement of the equations formulated in (Gatti *et al.* 2016) have been made, by including the transducer electrical effects into the energy harvester analytical model;

- The detrimental effects of damping in the harvester performance for train vibration have been identified;
- A laboratory-based system to emulate on an electromagnetic shaker the sleeper vertical vibration has been designed and tested experimentally;
- It has been shown that the excitation frequency with the largest acceleration amplitude is the target frequency for the electromagnetic harvester to have optimal performance;
- The amount of harvested energy from the sleeper vertical vibration induced due to a passing train has been determined theoretically and validated experimentally.

1.5 THESIS OUTLINE

This thesis outline is as follows:

- Chapter 1 presents an introduction, a literature review, objectives and contributions to the knowledge;
- Chapter 2 presents a brief introduction to the structure of a railway track. An analytical model of the sleeper vibration due to a passing train is derived in the time and frequency domains and the factors that govern the maximum acceleration amplitude are determined;
- Chapter 3 presents a brief overview of the piezoelectric and the electromagnetic transducers to determine by a simple comparison which is the best transducer for energy harvesting from low excitation frequencies. The analytical model derived in (Gatti *et al.* 2016) is improved by introducing the mechanical and electrical losses of the electromagnetic transducer and simplified formulations are presented to determine the optimum parameters;
- Chapter 4 presents a methodology to design a compensator filter based on the estimated system dynamics, and a laboratory-based system to emulate the sleeper vertical vibrations due to passing trains is designed and tested experimentally;
- Chapter 5 investigates, analytically and numerically, the linear electromagnetic energy harvester to determine the optimum transducer parameters, from sleeper vibration due to a passing train. An experiment is performed to validate the linear electromagnetic energy harvester model;
- Chapter 6 presents the overall conclusions and some suggestions for future work;

- Appendix A presents a set of sleeper vertical acceleration measurements and their corresponding power spectral densities due to the passage of an Inter-city 125 train;

2 SLEEPER VIBRATION DUE TO A PASSING TRAIN

2.1 INTRODUCTION

The need to transport a large number of people has made the railway one of the most used transport systems worldwide. The increase in its demand and, principally, in train speeds, bring some undesirable problems, such as noise and vibration (THOMPSON, 2008). Much effort has been spent to increase the performance of high-speed trains. Equally, much effort has been spent in reducing vibration to improve passenger comfort inside the train and to avoid discomfort of those who live near to railways lines. Nowadays, this undesirable vibration is seen as a potential source of electrical energy to power structural monitoring devices (GAO *et al.*, 2017; LI; JANG; TANG, 2012; MIAN, 2013; TAN *et al.*, 2009; ULIANOV *et al.*, 2020). However, there is a limited amount of work on which frequency of track vibration to target for energy harvesting and the physical reasons for this. The aim of this Chapter is to fill this gap in knowledge.

Vibrations of a railway track induced by passing trains occur due to the wheel/rail interaction and they can be subcategorized as quasi-static excitation, due to the trainload excitation, and the dynamic excitation, due to roughness, flat wheel and others excitations (LOMBAERT; DEGRANDE, 2009; SHENG; JONES; THOMPSON, 2004; THOMPSON, 2008). Auersch (2005) and Thompson (2008) compared the quasi-static excitation with the dynamic excitation and showed that quasi-static excitation is at low frequencies range (< 30 Hz). Moreover, it was found that close to the track, the dominant source of low frequency vibration of a railway track is the quasi-static loading as seen in (AUERSCH, 2005; SHENG; JONES; PETYT, 1999; TRIEPAISCHAJONSAK *et al.*, 2011) and this excitation mechanism is characterized by the passage of the axle sequence of a train (AUERSCH, 2006), resulting in large levels of vibration at the so-called trainload frequencies (JU; LIN; HUANG, 2009).

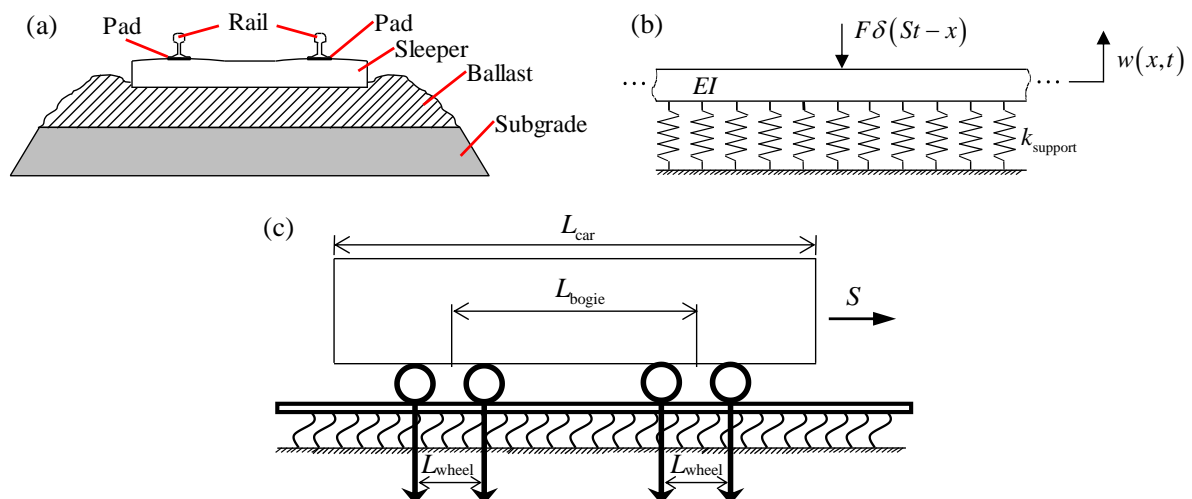
Recently, Gatti *et al.* (2016), Cleante *et al.* (2016) and Brennan and Gatti (2017b) carried out a fundamental investigation into the harvesting energy from track vibrations. They found that the optimum target frequency was the 7th trainload frequency for the case that they studied. This was the frequency at which the vertical track acceleration was the largest. The question that remains unanswered, however, is whether the 7th trainload frequency is the frequency with the largest vertical acceleration for all trains and why this particular trainload frequency has the largest amplitude.

In this chapter, a simple analytical model to predict the sleeper deflection due to the quasi-static excitation in time and frequency domains is derived. A numerical optimization is carried out to estimate the track and train parameters. The model is then validated with 5 different measurement datasets. Finally, using the model, the factors that govern the maximum vertical acceleration of the track vibration and the frequency at which this occurs are investigated. The results investigated in this chapter was published in Cleante *et al.* (2019).

2.2 MODEL OF SLEEPER VIBRATIONS DUE TO A PASSING TRAIN

A drawing showing the cross-section of a typical rail track is shown in Fig. 1(a). The system consists of two steel rails connected to concrete sleepers by clips and rail pads. The sleepers rest on ballast and subgrade which form the distributed track-bed stiffness per unit length of track k_{trackbed} . The low frequency (< 30 Hz) vertical vibration of the track is of interest and in this frequency range, the track vibration is predominantly that due to the quasi-static moving axle load. This is independent of the vehicle and track dynamics, whereas the track vibration due to dynamic excitation caused by the track and wheel irregularities is only significant at higher frequencies (SHENG; JONES; THOMPSON, 2003). The model, therefore, neglects dynamic effects and uses a quasi-static model of the track. Each wheel of the train can be assumed to act as a steady point force on the beam moving at the train speed S .

Figure 1. (a) example of the railway track structure; (b) a simplified model of the track structure consisting of an Euler-Bernoulli infinite beam on a Winkler foundation subject to a concentrated load; and (c) example of the load applied by each wheel of a carriage.



Source: (CLEANTE *et al.*, 2019).

The first resonance of the track, corresponding to the mass of the rail and sleeper, interacting with the ballast stiffness, occurs around 37 Hz for the Steventon site rail track¹, which is one of the tracks considered in this chapter. Below this frequency, the track behaves simply as a stiffness. The rail is modelled as a beam on an elastic foundation. It is sufficient to use Euler-Bernoulli beam theory for the rail as higher order effects such as shear deformation are only significant above about 500 Hz (KNOTHE; GRASSIE, 1993). As the distance between the sleepers L_{sleeper} , which is typically 0.65 m and is given in Tab. 1, is much smaller than the flexural wavelength in the rail at these low frequencies, the rail can be considered to be resting on an equivalent Winkler foundation with distributed support stiffness $k_{\text{support}} = \left(\frac{L_{\text{sleeper}}}{k_{\text{pad}}} + \frac{1}{k_{\text{trackbed}}} \right)^{-1}$, in which k_{pad} is the stiffness of a rail pad, and the mass of the sleepers is ignored. Note that the pad is described as a point stiffness and the trackbed as a distributed stiffness and that they combine in series to give the support stiffness.

Table 1 – Characteristics of the measurement sites.

Site	Rail type [Nm ²]	Rail pad [N/m]	Sleeper spacing [m]
1*	CEN 60E1 ($EI = 6.24 \times 10^6$)		
2**	CEN 60E1 ($EI = 6.24 \times 10^6$)	Pandrol 6650 ($k_p = 60 \times 10^6$)	0.65
3**	CEN 56 E ($EI = 4.86 \times 10^6$)		
4**	CEN 56 E ($EI = 4.86 \times 10^6$)		

Source: *(TRIEPAISCHAJONSAK, 2012); **(LE PEN *et al.*, 2016).

An example of a single wheel load on the model of a single rail system is shown in Fig. 1(b), where EI is the flexural stiffness of the rail, $w(x,t)$ is the vertical rail deflection F is the moving load due to the wheel, δ is the delta function, and x is the horizontal position of the wheel, with reference to an arbitrary reference point. Figure 1(c) shows a typical single carriage of a train, in which L_{car} is the length of the carriage, L_{wheel} is the distance between two wheels on a bogie and L_{bogie} is the distance between the central points of the two bogies. The equation of motion for the rail with a single carriage acting on it is given by (FRÝBA, 1999)

$$EI \frac{\partial^4 w(x,t)}{\partial x^4} + k_{\text{support}} w(x,t) = - \sum_{i=1}^4 F_i \delta(St - x - d_i) \quad (1)$$

¹ The first resonance of the track, corresponding to the mass of the rail and sleeper interacting with the support stiffness, is given by (GRASSIE *et al.*, 1982) $\omega_1 = \sqrt{k_{\text{trackbed}} / (m_{\text{rail}} + m_{\text{sleeper}})}$, where m_{rail} and m_{sleeper} are the rail and sleeper masses per unit length, respectively. For the Steventon site $m_{\text{rail}} = 60$ kg/m; $m_{\text{sleeper}} = 245$ kg/m; and $k_{\text{trackbed}} = 16.5$ MN/m² (TRIEPAISCHAJONSAK, 2012).

where t is time, F_i is the force due to the i -th wheel and $d_1 = 0$, $d_2 = L_{\text{wheel}}$, $d_3 = L_{\text{bogie}}$ and $d_4 = L_{\text{wheel}} + L_{\text{bogie}}$. Noting that the relationship between the vertical displacements of the sleeper, w_{sleeper} , and the rail is given by $\frac{w_{\text{sleeper}}}{w} = \frac{k_{\text{support}}}{k_{\text{trackbed}}}$, the solution to Eq. (1) can be written

$$w_{\text{sleeper}}(x, t) = \frac{-\beta}{2k_{\text{trackbed}}} \sum_{i=1}^4 F_i e^{-\beta|St - x_i - d_i|} \left[\cos(\beta(St - x_i - d_i)) + \sin(\beta|St - x_i - d_i|) \right] \quad (2)$$

where $\beta = \left(\frac{k_{\text{support}}}{4EI} \right)^{1/4}$ has units of m^{-1} . Equation (2) can be written in non-dimensional form as

$$\hat{w}_{\text{sleeper}}(\hat{x}, \hat{t}) = \frac{w_s(x, t)}{\sum_{i=1}^4 \frac{F_i}{2k_{\text{support}} L_{\text{car}}}} = -\alpha \sum_{i=1}^4 e^{-\alpha|\hat{t} - \hat{x} - d_i|} \left[\cos(\alpha(\hat{t} - \hat{x} - d_i)) + \sin(\alpha|\hat{t} - \hat{x} - d_i|) \right] \quad (3)$$

where $\alpha = \beta L_{\text{car}}$, which is the non-dimensional characteristic length, $\hat{x} = \frac{x}{L_{\text{car}}}$, $\hat{d}_i = \frac{d_i}{L_{\text{car}}}$ and $\hat{t} = \frac{t}{t_0}$, where $t_0 = \frac{L_{\text{car}}}{S}$ is the time it takes one carriage to pass an observation point passing at speed S . For the value of $EI = 6.24 \text{ MNm}^2$ given in Tab. 1, and for a carriage length of $L_{\text{car}} = 23 \text{ m}$ given in Tab. 2, then for a range of support stiffness of 10 to 60 MN/m^2 , α has a range of 18 to 28 (LE PEN *et al.*, 2016). The normalized velocity and acceleration of the sleeper are found by differentiating Eq. (3) once and twice respectively with respect to \hat{t} , to give

$$\dot{\hat{w}}_{\text{sleeper}}(\hat{x}, \hat{t}) = -2\alpha^2 \sum_{i=1}^4 e^{-\alpha|\hat{t} - \hat{x} - d_i|} \left[\sin(\alpha(\hat{t} - \hat{x} - d_i)) \right] \quad (4)$$

and

$$\ddot{\hat{w}}_{\text{sleeper}}(\hat{x}, \hat{t}) = 2\alpha^3 \sum_{i=1}^4 e^{-\alpha|\hat{t} - \hat{x} - d_i|} \left[\cos(\alpha(\hat{t} - \hat{x} - d_i)) - \sin(\alpha|\hat{t} - \hat{x} - d_i|) \right] \quad (5)$$

where the overdots denote differentiation with respect to \hat{t} . Using Eqs. (3)-(5), the non-dimensional displacement, velocity and acceleration for an Inter-city 125 are calculated for a value of $\alpha = 20$ and the observation point set at $\hat{x} = 1$. The plots for a single wheel, a bogie and a carriage are shown in Figs. 2(a.i)-2(a.iii). The displacement of the rail as each of the four wheels passes the observation point is clear in Fig. 2(a.i). It is also apparent that the rail does not return to its original position during the passage of a single bogie, but it does so between the passage of the two bogies. It can be seen that the curves for displacement and velocity are relatively smooth, but the acceleration curve is non-smooth, which means that the jerk

(derivative of acceleration) is discontinuous. This occurs at the point where there is a maximum deflection of the rail and is because of the assumption of zero mass in the system, which of course is not physical. Despite this minor deficiency in the model it is acceptable for the purposes of this chapter (which is demonstrated later) and allows a simple model to be used, which facilitates physical insight.

Table 2 – Train parameters.

Site	Train class	Name	Car length [m] – L_{car}	Bogie length [m] – L_{wheel}	Distance between bogie centre [m] – L_{bogie}
1*	Mk3	Inter-city 125	23.0	2.6	16.0
2**	390	Pendolino	23.9	2.7	17.0
2**	221	Supervoyager	22.9	2.6	15.9
3**	171	Turbostar	23.6	2.6	15.8
4**	377	Electrostar	20.0	2.6	14.2

Source: *(TRIEPAISCHAJONSAK, 2012); ***(LE PEN *et al.*, 2016).

Of particular interest is the spectrum of the vibration at an arbitrary observation (measurement) point. Thus \hat{x} is set to zero in Eq. (3) and the Fourier transform used to calculate the non-dimensional spectrum to give

$$\hat{W}_{\text{sleeper}}(\hat{f}_{\text{car}}) = \frac{-8\alpha^4}{4\alpha^4 + (2\pi\hat{f}_{\text{car}})^4} \sum_{i=1}^4 e^{-j2\pi\hat{f}_{\text{car}}\hat{d}_i} \quad (6)$$

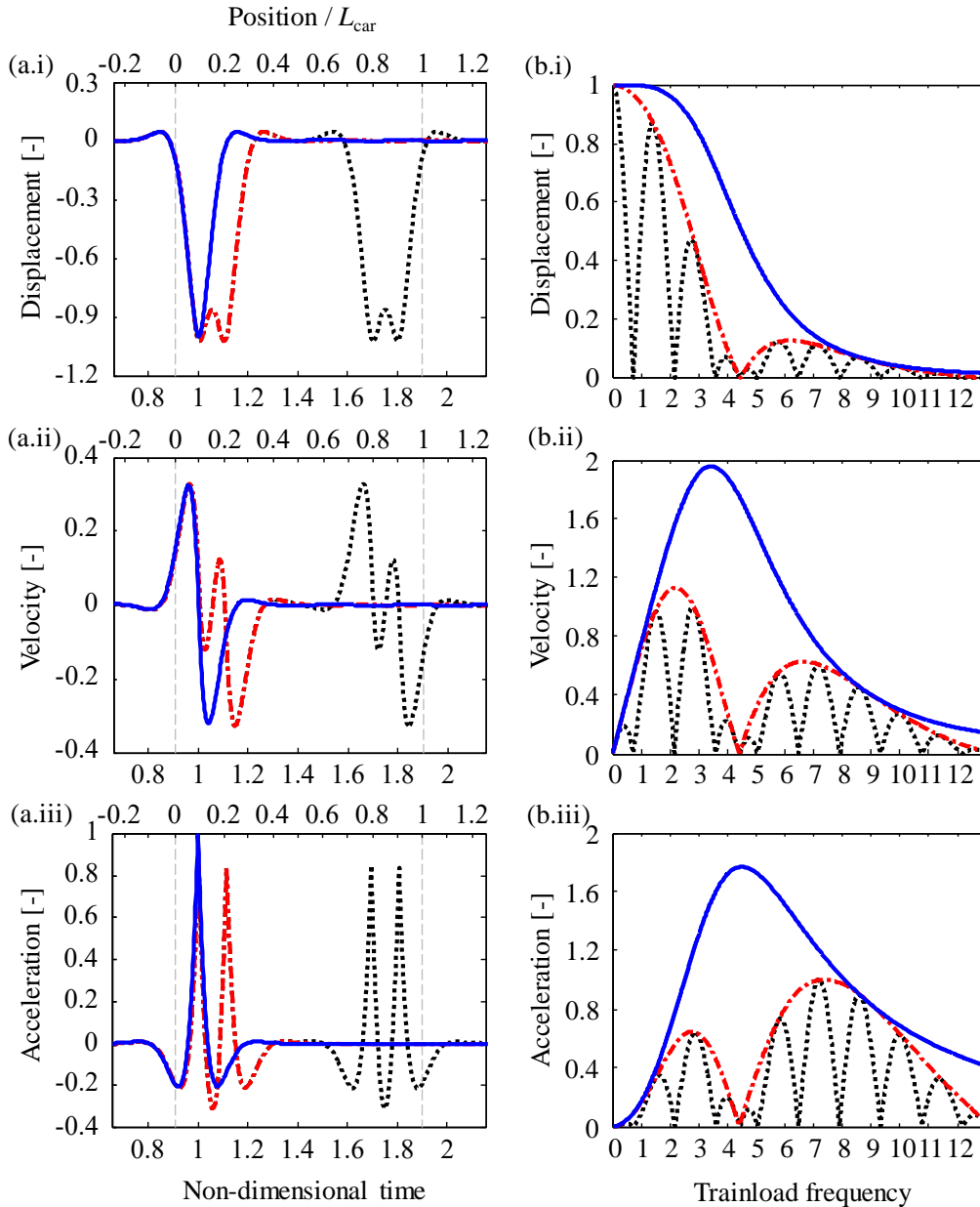
where $\hat{f}_{\text{car}} = f \times \frac{L_{\text{car}}}{S}$ is the non-dimensional so-called “trainload frequency” (JU; LIN; HUANG, 2009), and $j = \sqrt{-1}$. A trainload frequency of 1 corresponds to the passage of a single carriage. The non-dimensional velocity and acceleration spectra can be calculated by simply multiplying Eq. (6) by $j2\pi\hat{f}_{\text{car}}$ and $-(2\pi\hat{f}_{\text{car}})^2$ respectively to give

$$\dot{\hat{W}}_{\text{sleeper}}(\hat{f}_{\text{car}}) = \frac{-j16\pi\alpha^4\hat{f}_{\text{car}}}{4\alpha^4 + (2\pi\hat{f}_{\text{car}})^4} \sum_{i=1}^4 e^{-j2\pi\hat{f}_{\text{car}}\hat{d}_i} \quad (7)$$

and

$$\ddot{\hat{W}}_{\text{sleeper}}(\hat{f}_{\text{car}}) = \frac{32\pi^2\alpha^4\hat{f}_{\text{car}}^2}{4\alpha^4 + (2\pi\hat{f}_{\text{car}})^4} \sum_{i=1}^4 e^{-j2\pi\hat{f}_{\text{car}}\hat{d}_i} \quad (8)$$

Figure 2. Sleeper vibration due to the passage of one wheel (blue solid line, —) one bogie (red dash dot line, - · -); and one carriage (black dotted line, · · ·). The column (a) is the time history (at the top there is another axis corresponding to the non-dimensional position); and (b) normalized spectrum for: (i) displacement; (ii) velocity; and (iii) acceleration.



Source: (CLEANTE *et al.*, 2019).

The modulus of the non-dimensional spectra corresponding to the non-dimensional displacement, velocity and acceleration are plotted in Figs. 2(b.i)-2(b.iii), for one wheel, one bogie and one carriage, with each spectrum being normalised by the number of wheels. This is done so that the shapes of the spectra can be easily compared. The displacement spectrum in Fig. 2(b.i) for the passage of a single wheel is similar to the spectrum of an impulse, exhibiting

behaviour similar to a low-pass filter, with the largest displacements occurring at low frequencies.

The shape of this spectrum is entirely due to the track properties, and in (LE PEN *et al.*, 2016), it is called the shape function. If the passage due to a bogie is considered, then for all frequencies the spectrum remains within the spectrum due to a single wheel. The specific shape of this spectrum is discussed later. For the spectrum of the carriage (four wheels), then for all frequencies, the spectrum remains within the spectrum due to a bogie. Again, the specific shape of this spectrum is discussed later.

Concerning the shapes of the velocity and acceleration spectra, it can be seen that the effect of differentiation with respect to time is to cause the spectra to peak at higher frequencies. For example, when the whole carriage is considered it can be seen that the velocity peaks at around the 3rd trainload frequency, and the acceleration peaks at about the 7th trainload frequency. The reasons for this phenomenon are discussed in detail later in the chapter, once the model has been validated with experimental data.

2.3 COMPARISON OF THE MODEL WITH EXPERIMENTAL DATA

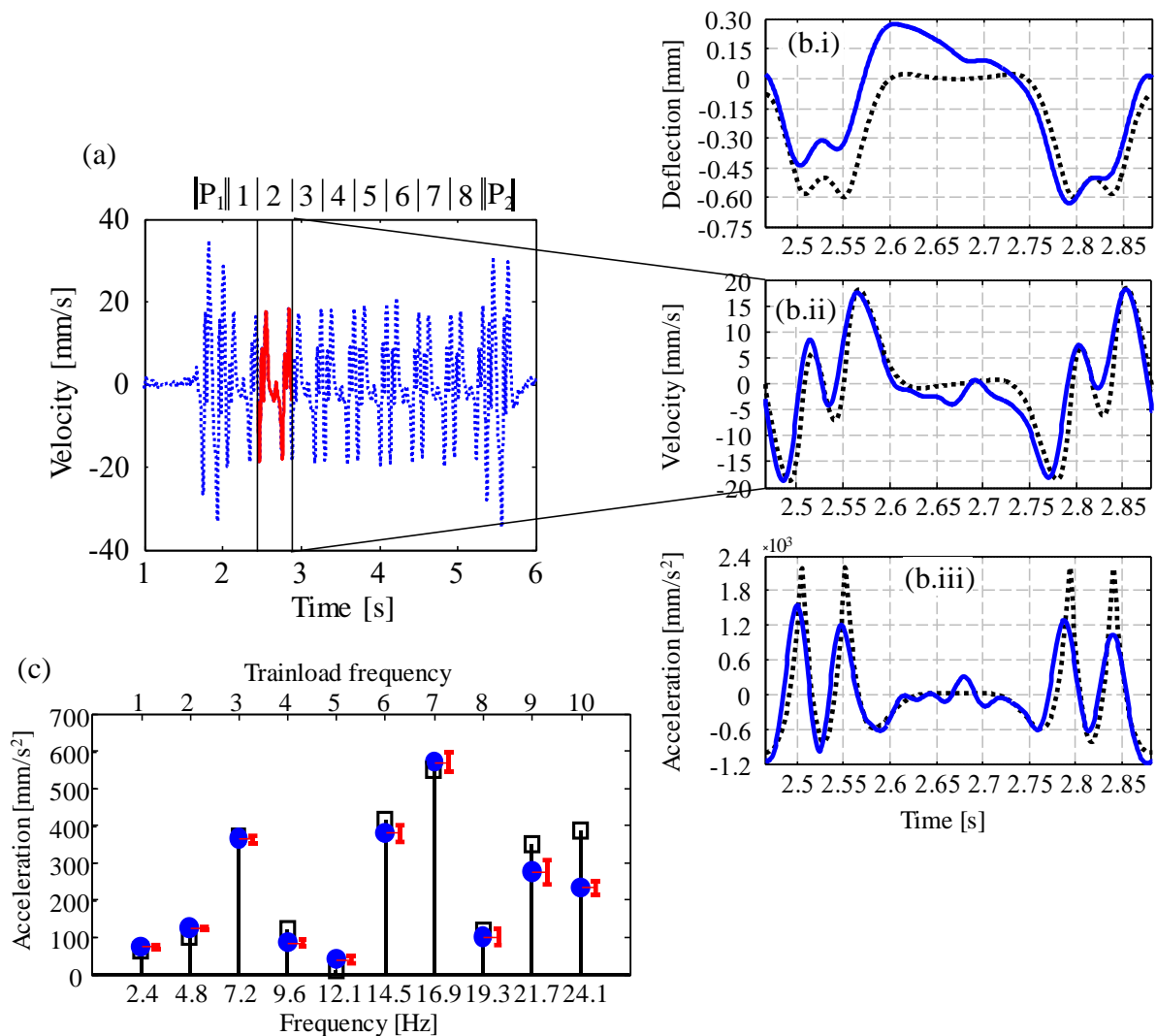
2.3.1 Description of the experimental data

To verify that the model can adequately predict the spectrum of the vertical vibration of a sleeper due to a passing train, it is compared with data from five trains at four different sites. One is an Inter-city 125 consisting of two power cars and eight passenger carriages passing at a speed of 200 km/h (TRIEPAISCHAJONSAK, 2012). The sleeper vibration was measured for the passing of a complete train using an accelerometer with a sampling frequency of 1 kHz. The data for the other four trains are taken from (LE PEN *et al.*, 2016) and are extracted to give the time series for a single carriage for each train. The trains are a Pendolino travelling at a speed of 195 km/h, a Supervoyager travelling at a speed of 202 km/h, a Turbostar travelling at speed of 103 km/h and an Electrostar travelling at speed of 109 km/h. In each case, the measurements were made using a geophone with a sampling frequency of 500 Hz, positioned at the outer side of a sleeper. The track and train parameters are given in Tables 1 and 2, respectively.

The measured vertical sleeper velocity of the Inter-city 125 train is shown in Fig. 3(a). This was obtained by integrating acceleration data and is shown because some pertinent features are more visible in velocity data rather than acceleration data. The train consists of two power

cars, one at the front and the other at the rear of the train, and eight carriages. These are marked at the top of Fig. 3(a). The repetitive velocity pattern can be seen, as each carriage passes the measurement point, and the slightly larger velocities due to the heavier power cars can also be seen.

Figure 3. Sleeper vertical vibration induced by an Inter-city 125 at speed of 200 km/h: (a) velocity, $\bullet\bullet\bullet$ (blue dotted line) is the full time-history, $-$ (red solid line) is a period corresponding to the passage of a single carriage (at the top of the graph there is an axis indicating the carriages: P_1 and P_2 are the power cars and 1-8 are the passenger carriages); (bi-iii) zoom-in of the comparison of displacement, velocity and acceleration, respectively, between measurement (blue solid line, $-$) and model (black dashed line, $\bullet\bullet\bullet$); and (c) comparison between Fourier coefficients of sleeper vertical acceleration of measurement (blue circle, \bullet); standard deviation range from the eight passenger carriages (red line, $-$); and model (black square, \square).



Source: (CLEANTE *et al.*, 2019).

As each carriage appears to generate a similar vibration pattern, the vibration of carriage 2 is extracted from the time series. A zoom of this can be seen in Fig. 3(b.ii), with corresponding zooms of the displacement and acceleration shown in Figs. 3(b.i) and 3(b.iii) respectively. An overlay of the model predictions is also shown in Fig. 3, and these are discussed later.

To extract frequency domain data from the measurement, it is assumed this section of data repeats indefinitely, i.e., the train is infinitely long and consists only of carriages. The Fourier series coefficients can then be calculated. The amplitudes of the first ten coefficients for acceleration data are plotted in Fig. 3(c) as solid blue circles. As mentioned in the introduction, from the perspective of energy harvesting, acceleration rather than velocity is the important quantity. At the top of Fig. 3(c) there is another axis which represents the trainload frequencies. It can be seen that the amplitude of acceleration is greatest at the 7th trainload frequency, which corresponds to 16.9 Hz. The amplitudes are also high at some other trainload frequencies, such as the 3rd and the 6th, but are very low at others, such as the 4th, the 5th and the 8th.

Also shown in Fig. 3, is the range of amplitude coefficients if carriages other than the second are taken to be the representative carriage for the train. It can be seen that, although there are some differences between each carriage, the general trend is the same. Thus, it is sufficient to consider a single carriage for the purposes of this chapter. This assertion is further supported by presentation of the spectra for a complete Inter-city 125 train travelling at different speeds, which is shown in Appendix A. Considering vibration at the trainload frequencies, similar behaviour is observed in each case, and is qualitatively similar to that for a single carriage.

2.4 SIMULATIONS USING THE MODEL

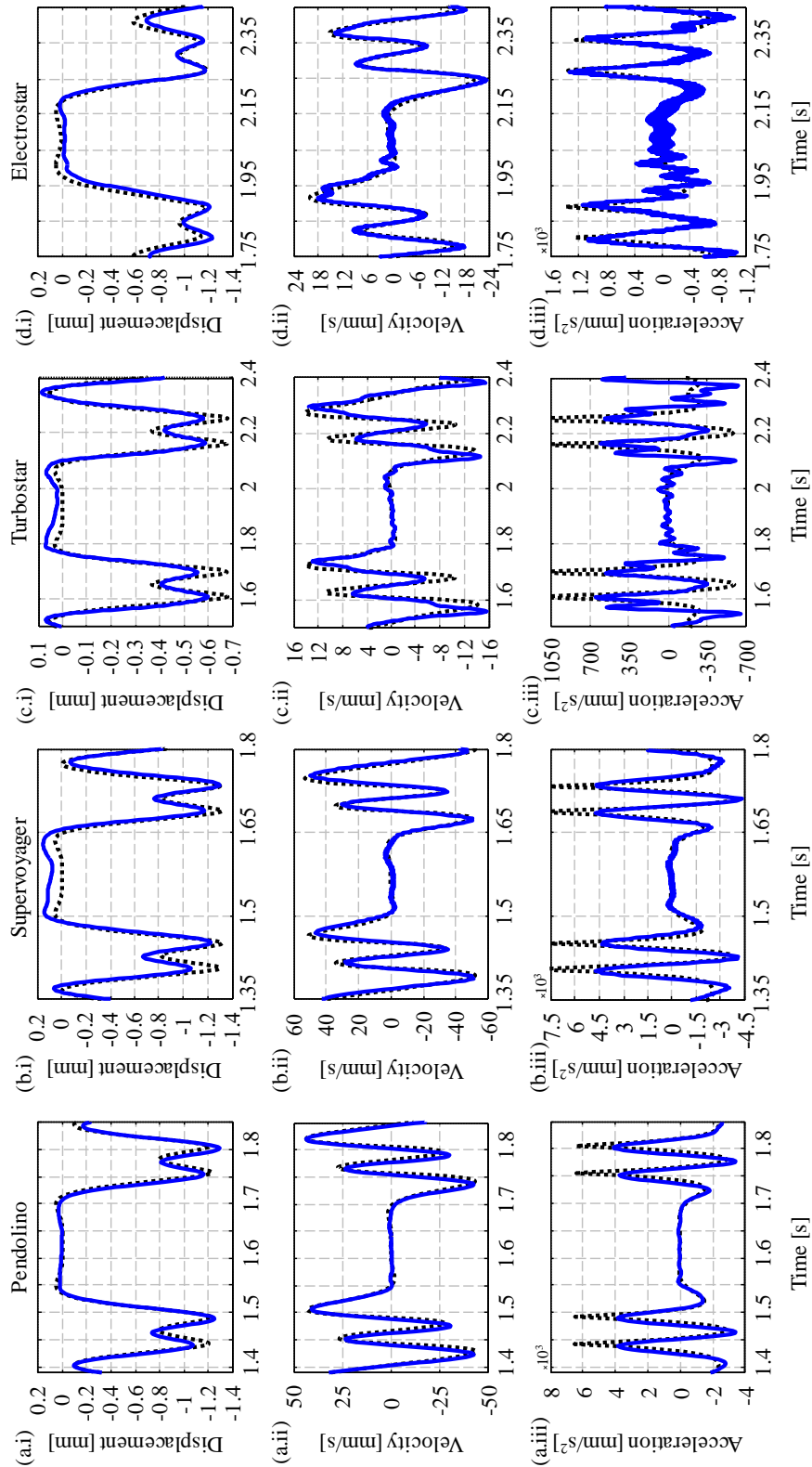
The deflection of the railway track is influenced by the support stiffness k_{support} , which is a series combination of the rail pad and track-bed stiffness. Reliable pad parameters are relatively easily found in a manufacturer's datasheet, but the track-bed stiffness is highly variable and changes over time due to degradation, ballast migration and other factors. It is thus not a simple matter to determine this parameter. Moreover, the track-bed stiffness may vary along a railway line and may be different from one sleeper to another (J. A. PRIEST; W. POWRIE, 2009). To determine the track-bed stiffness, an optimization procedure is used together with the model and measured data. A two-step optimization procedure is carried out to determine the track-bed stiffness and trainload from the measured vertical vibration of a

sleeper. For a single carriage, the sum of the squares of the differences between the Fourier coefficients of the model and the measured acceleration data (from 0 to 30 Hz), is minimised using the *Matlab* function *optimset*. First, an optimum value of β using Fourier coefficients normalized by the value of the maximum coefficient, then an optimum value of the trainload is calculated using a similar procedure.

The estimated Fourier coefficients are shown in Fig. 3(c) as squares. It can be seen that there is good agreement between the model predictions and the experimental data for the first eight trainload frequencies. The agreement is not so good for the 9th and 10th trainload frequencies. The reason for this can be seen if the time histories are reconstructed from the estimated Fourier coefficients. These are shown in Figs. 3(b.i)-(b.iii) for displacement, velocity and acceleration respectively. It can be seen that displacement and velocity are predicted well, with the displacement showing some very low frequency drift, but the acceleration predicted by the model is non-smooth as discussed in Section 1.3. This feature requires high frequency vibration, which is limited in the experimental measurements due to the mass of the track system. This is believed to be the principal cause of the discrepancy between the predicted and measured Fourier coefficients at higher frequencies.

To further verify the model, four data sets consisting of sleeper displacement, are also used. These data were taken from (LE PEN *et al.*, 2016) and consist of only displacement data for a single carriage in each case. A similar procedure to that described above is used to determine the support stiffness. The predicted results and measured data are shown in Figs. 4 and 5, for the time histories and Fourier coefficients respectively. The number of coefficients used to calculate each measurement data was in the frequency range up to 30 Hz. It can be seen that there is good agreement between the model predictions and the measurements with the largest amplitude being at the 7th trainload frequency in three out of the four cases. In the other case, the largest amplitude is at the 6th trainload frequency, but the amplitude at the 7th trainload frequency is only marginally smaller. In all cases, the displacement, velocity and acceleration time histories are in remarkable agreement with the measurements, except at higher frequencies in some cases.

Figure 4. Comparison of sleeper vertical vibration between measurement (blue solid line, —) and model (black dotted line, •••) due to the passage of: a) Pendolino at speed of 200 km/h; b) Supervoyager at speed of 202 km/h; c) Turbostar at speed of 103 km/h; and d) Electrostar at speed of 109 km/h. (i) denotes displacement; (ii) velocity; and (iii) acceleration.



Source: (CLEANTE *et al.*, 2019).

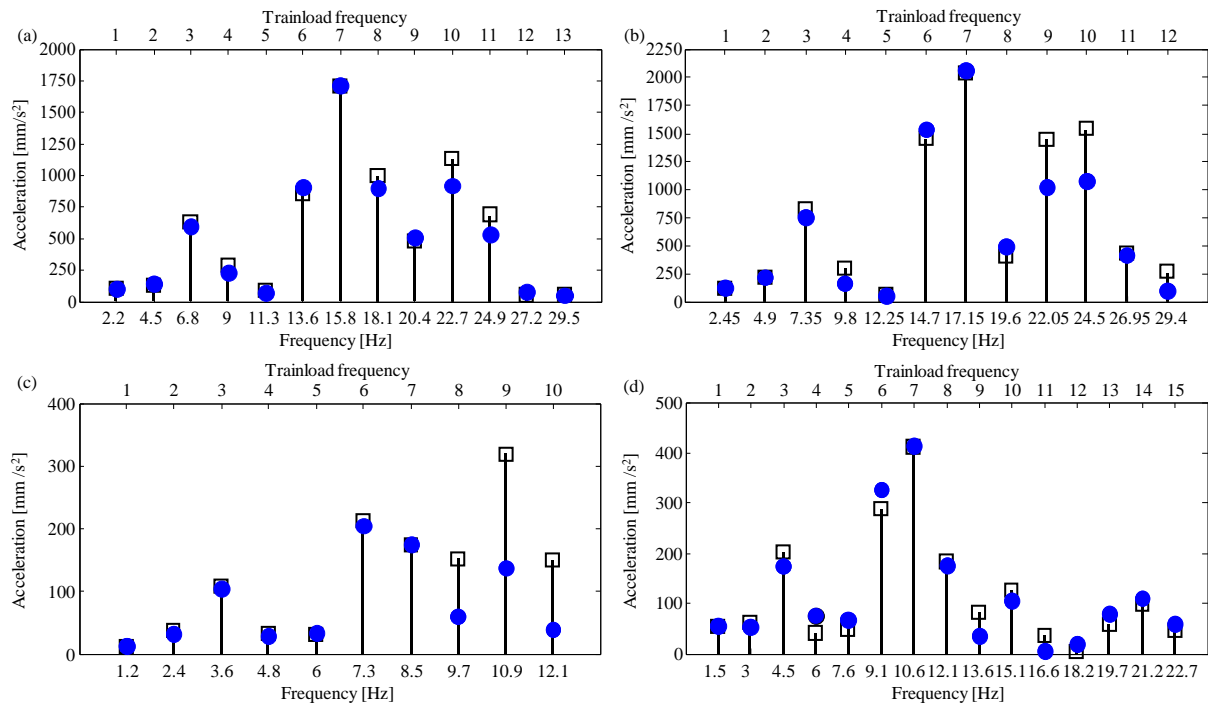
The calculated support stiffness and trainloads are given for all cases in Tab. 3. It can be seen that there is a fairly narrow range for α ranging from slightly more than 17 to slightly more than 26. It can also be noted that the calculated support stiffness for the site No. 2 has two different values for two different trains. It is stiffer for the heavier train, which suggests that the stiffness has a hardening characteristic.

Table 3 – Calculated support stiffness and train load for five different trains.

Site	Train class	Fixed parameter		Estimated parameter		
		Pad stiffness [MN/m]	Speed [km/h]	Load F [kN]	Support stiffness [MN/m ²]	α
1	Mk3		200	21.9	14	19.9
2	390		195	81.8	24.4	23.8
2	221	60	202	120.2	30.1	24.1
3	171		103	56.7	30.2	26.4
4	377		109	34.6	11.4	17.5

Source: (CLEANTE *et al.*, 2019).

Figure 5. Comparison between Fourier coefficients of sleeper vertical acceleration of measurement (blue circle, ●); and model (black square, □) for: (a) Pendolino at 195 km/h; (b) Supervoyager at 202 km/h; (c) Turbostar at 103 km/h; and (d) Electrostar at 109 km/h.



Source: (CLEANTE *et al.*, 2019).

2.5 DISCUSSION

In the previous sections, it was shown that the spectrum of the sleeper acceleration has a particular shape, which is reasonably consistent for different train types and different sites. In all cases, the amplitude of the acceleration at the 7th trainload frequency is either the largest or very close to being the largest. In this section, the reason why this is the case is discussed. To study this, the geometrical parameters of the Inter-city 125 are used, with a value of $\alpha = 20$. The modulus of Eq. (8) is plotted for the passage of a single wheel, a single bogie, a single carriage, and an infinite series of carriages in Fig. 6. Note, that in each case, the amplitude is normalised by the maximum amplitude of one wheel deflection and then divided by the number of wheels, so that the shape of the spectra can be easily compared. For a single wheel, the modulus of the non-dimensional spectrum of the acceleration is given by

$$\ddot{W}_{\text{sleeper}}(\hat{f}_{\text{car}}) \Big|_{\text{wheel}} = \frac{32\pi^2\alpha^4\hat{f}_{\text{car}}^2}{4\alpha^4 + (2\pi\hat{f}_{\text{car}})^4}, \quad (9)$$

which is only dependent on the track. It is plotted as a thick solid red line in Fig. 6. It can be seen that it behaves as a band-pass filter, with a peak when the trainload frequency $\hat{f}_{\text{car}} = f \times \frac{L_{\text{car}}}{S} = \frac{\alpha}{\pi\sqrt{2}}$. For the Inter-city 125 considered here, this is when the trainload frequency is about 4.5. This is the principal reason why the acceleration spectrum is confined to a low frequency range. As mentioned in Section 2.2 the band-pass behaviour is due to the low-pass filtering effect of the track deflection bowl under a wheel load and the high-pass filtering effect due to acceleration being the quantity of interest. The vibration due to the passage of a single bogie (two wheels) is shown in Fig. 6 as a blue dashed line. This is better viewed on the frequency axis $\hat{f}_{\text{wheel}} = f \times \frac{L_{\text{wheel}}}{S}$, which is the wheel passage frequency for a single bogie. It can be seen that it is zero when $\hat{f}_{\text{wheel}} = (n+0.5)$ for $n=0,1,2,\dots$. The frequencies at which the amplitude is zero is only a function of the distance between the wheels on the bogie and the train speed. This phenomenon has also been discussed by Auersch (2006) and Milne *et al.* (2017). However, the peaks in the spectrum that occur between the zeros are dependent on both the train geometry and the track properties. The maxima occur in this particular case when $f \times \frac{L_{\text{wheel}}}{S} \approx 0.31$ and $f \times \frac{L_{\text{wheel}}}{S} \approx 0.83$. Thus, the bogie has created two bandpass frequencies, one centred at $f \times \frac{L_{\text{car}}}{S} \approx 2.74$ and the other at $f \times \frac{L_{\text{car}}}{S} \approx 7.34$, with a zero in between these frequencies at $f \times \frac{L_{\text{car}}}{S} \approx 4.4$. Note that, for this value of α , the higher frequency (7.34) peak is

larger than the lower frequency (2.74) peak. This means that the trainload frequency with the highest amplitude of vibration will occur close to this frequency.

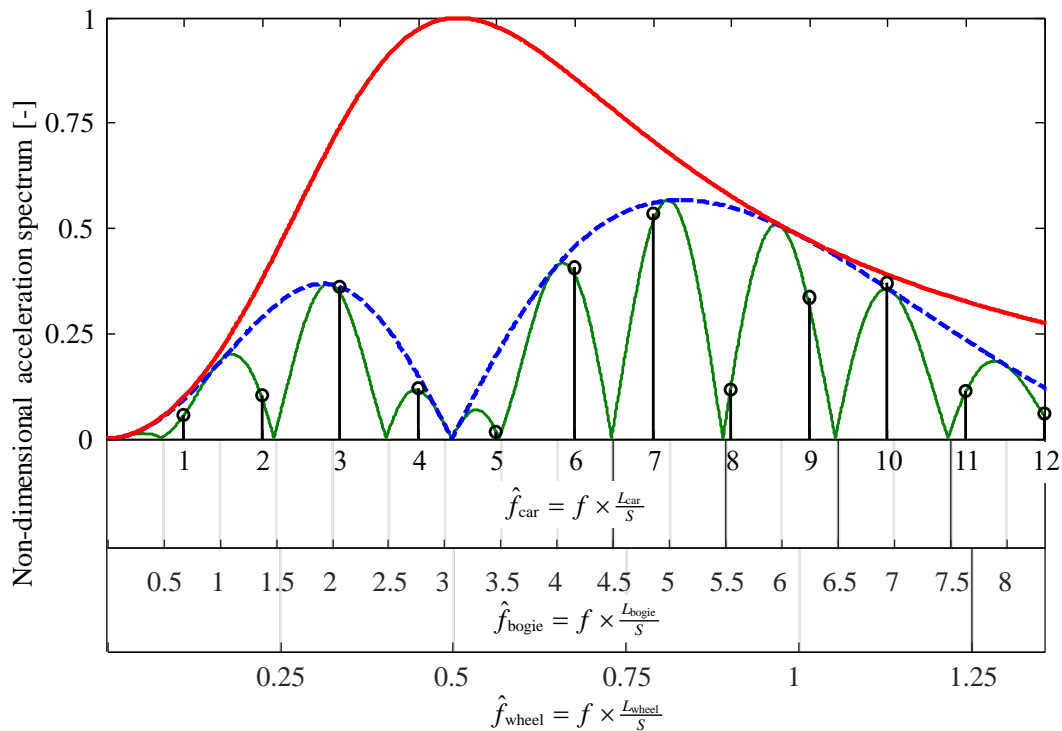
The spectrum for the passage of two bogies (i.e. a carriage) is also plotted in Fig. 6 as a thin solid green line. Note that the amplitude is divided by four. In this case, the spectrum is better viewed on the frequency axis $\hat{f}_{\text{bogie}} = f \times \frac{L_{\text{bogie}}}{S}$, which is the passage frequency for two bogies. It can be seen that there are zeros when $\hat{f}_{\text{bogie}} = (n + 0.5)$ for $n = 0, 1, 2, \dots$, which is only a function of the distance between the bogies and the train speed. It can be further seen that there are also zeros at the same frequencies as for a single bogie (when $f \times \frac{L_{\text{wheel}}}{S} = 0.5$), which is dependent, of course, on the wheel spacing for a single bogie. Between the zeros, there are peaks which are dependent on both train geometry and track properties. It can be seen that the zeros have the effect of significantly reducing the acceleration responses at 5th and 8th trainload frequencies. In general, if the support stiffness is kept constant and train geometry is changed, the zeros created by the passage of one and two bogies shift to different frequencies, which means that the maxima will also shift to different frequencies. This effect is not large, however, given the similarity in train geometries found in practice. If the track properties change, then the effect will be to shift the frequency at which the maximum of the thick solid red line occurs, $\hat{f}_{\text{car}} = \frac{\alpha}{\pi\sqrt{2}}$, in Fig. 6. If the support stiffness is softer, then it could cause the maximum to occur at a frequency lower than that at which the amplitude for a single bogie has its lowest peak (lower than $f \times \frac{L_{\text{wheel}}}{S} = 0.5$). However, this would require an extremely low support stiffness that is unlikely to be seen in practice ($k_{\text{support}} \ll 10 \text{ MN/m}^2$). This can be easily seen by noting that for the peak in the thick solid red curve to occur at a significantly lower frequency (say $f \times \frac{L_{\text{wheel}}}{S} = \frac{3}{8}$) than when the first zero occurs for the single bogie (the first zero in the dashed blue curve), then it is required that

$$\frac{\alpha}{\pi\sqrt{2}} < \frac{3}{8} \frac{L_{\text{car}}}{L_{\text{wheel}}} \quad \text{or that} \quad \alpha < \frac{\pi 3\sqrt{2}}{8} \frac{L_{\text{car}}}{L_{\text{wheel}}}.$$

For the Inter-city train then this means that $\alpha < 14.74$, which corresponds to a support stiffness of $k_{\text{support}} < 4.2 \text{ MN/m}^2$, which is very low. An illustration of this effect is shown in Fig. 7(a). If the support stiffness is larger than that used for the simulation shown in Fig. 6, there will be little change to the frequency at which the peak amplitude occurs. This is illustrated in Fig. 7(b), for the case of $\alpha = 28$, which corresponds to a track stiffness of 60 MN/m^2 . Thus, it may be assumed that in the majority of the cases found in practice, it is likely that the 7th

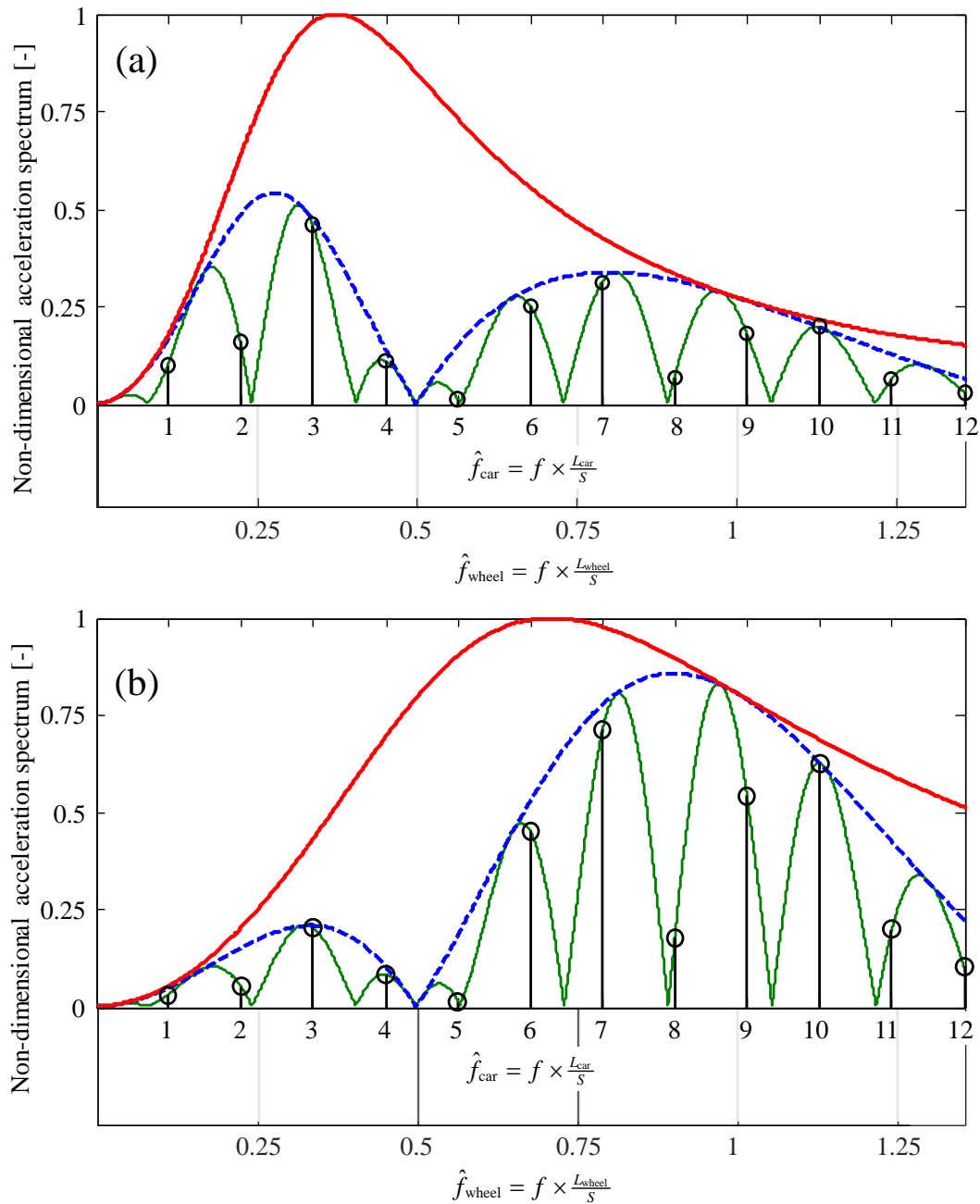
trainload frequency will generally be the frequency at which the amplitude of acceleration is the largest, and hence is the frequency to target for energy harvesting.

Figure 6. Sleeper non-dimensional vertical acceleration spectrum, for $\alpha = 20$ normalized by the maximum amplitude of one wheel induced deflection due to the passage of: one wheel, red solid line —; one bogie (divided by two), blue dashed line - -; one carriage (divided by four), green thin line —; and infinite train of carriages, black circle \circ . The curves were scaled to fit the same envelope.



Source: (CLEANTE *et al.*, 2019).

Figure 7. Sleeper non-dimensional vertical acceleration spectrum normalized by the maximum amplitude of one wheel induced deflection due to the passage of: one wheel, red solid line —; one bogie (divided by two), blue dashed line - -; one carriage (divided by four), green thin line —; and infinite train of carriages, black circle ○. The curves were scaled to fit the same envelope. (a) softer support stiffness, $\alpha = 14.7$; and (b) stiffer support stiffness, $\alpha = 28$.



Source: (CLEANTE *et al.*, 2019).

2.6 CONCLUSIONS

This chapter has described an investigation into why the highest amplitude of track acceleration due to the passage of a train is generally the 7th trainload frequency. A simple quasi-static model of a train moving along a track has been developed and used to conduct the investigation. Some of the model parameters were determined by comparing the model predictions with experimental data. Measurements involving five trains from four different sites have been used to verify that the model can adequately capture the pertinent physical behaviour. The analysis showed that the spectrum due to the passage of one wheel is only dependent on the track features, and acts as a bandpass filter. This effectively restricts the quasi-static component of sleeper vibration due to a passing train to low frequencies. However, the geometry of the train passing at the measurement site has a profound effect on which specific trainload frequency has the largest response amplitude. Of particular importance is the wheel spacing in a bogie, as this partitions the band-pass filter effect into two frequency ranges, and in general, it is the highest of these ranges which is important from the energy harvesting point of view.

For the trains studied, it was observed that the 3rd, 6th, 7th, 8th and 10th trainload frequencies had the highest amplitude of the vibration, with the 7th trainload frequency having the highest amplitude in four out of the five cases. In the case of an extremely soft track support stiffness then it is possible, in principle at least, for the largest amplitude to occur below the 4th trainload frequency, typically at the 3rd.

For the energy harvesting application, these trainload frequencies are the frequencies with the potential to be the device target frequency. This is investigated further in Chapter 5, in which an electromechanical transducer is incorporated into the railway environment to harvest energy from the vibration due to passing trains.

3 ENERGY HARVESTING: TIME-LIMITED PERIODIC EXCITATION

3.1 INTRODUCTION

The development of new electrical components which require less power has motivated researchers to improve the technology of small energy harvesters and to maximize the power scavenged. In addition, due to climate change, the desire to develop alternative ways to provide clean energies has increased research efforts to improve the performance of existing energy harvester technologies. It has also motivated the design of new mechanisms to scavenge mechanical energy from ambient vibration and to convert it into electrical energy.

A large number of papers have been published, in which the analysis takes into account the effects of the host structure and the transducer. In the majority of the work it is assumed that the excitation source has a long time duration and so only the steady-state response is considered. However, some ambient vibrations may have limited time excitation making the transient effects important in the design of an energy harvesting device.

In publications by Gatti *et al.* (2016) and Brennan and Gatti (2017a), it was shown that disregarding the transient effects from time-limited excitation sources can lead to an incorrect prediction of the potential mechanical energy that could be harvested. In this chapter, similar analysis is undertaken, but the electrical effects of electromechanical transducers are taken into consideration, with the aim of determining the potential electrical energy from a time-limited excitation source.

In this chapter, the concepts of mechanical impedance are first introduced. Using a two-port network transducer model, the electric effects of an electromechanical transducer are evaluated, and a simple comparison is made between a piezoelectric and electromagnetic transducer. Later, a single-degree-of-freedom electromagnetic energy harvester is investigated. An analytical expression for the energy dissipated by a load resistance attached to an electromagnetic transducer when subject to a time-limited base excitation, which may include the transient and steady-state responses, is presented, and the optimum load resistance is determined.

3.2 THE MECHANICAL IMPEDANCE OF A SINGLE-DEGREE-OF-FREEDOM MASS-SPRING-DAMPER BASE EXCITATION SYSTEM

This section presents a brief discussion on the mechanical impedance of a linear single-degree-of-freedom (SDOF) mass-spring-damper system, which is a typical mechanical system of an energy harvesting device. The aim is to determine which would be the better operational condition to maximize the oscillation of the suspended mass and potentially increase the harvester efficiency. It is assumed that the impedance of the vibration source, Z_S , is much larger than the impedance of the device, Z_D , so that the velocity of the device approximate to the velocity of the source, $\dot{X}_D \approx \dot{X}_S$ and the device is then a typical base excited system.

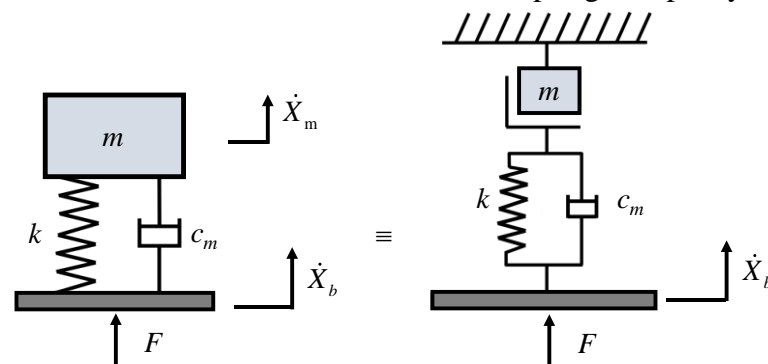
The mechanical impedance of an element is defined as the frequency-dependent relationship between the driven force acting on that element and its resulting velocity for the time-dependent harmonic excitation. The impedance of a mass (m), a spring (k) and a mechanical damper (c_m) are given in Tab. 4, where ω is the angular frequency and $j=\sqrt{-1}$.

Table 4 – The element impedance.

Element	Impedance
Mass	$Z_m = j\omega m$
Spring	$Z_k = \frac{-jk}{\omega}$
Damper	$Z_c = c_m$

Source: (HARRIS; PIERSOL, 2002).

Figure 8. The combination of a base-excited SDOF mass-spring-damper system.



Source: author.

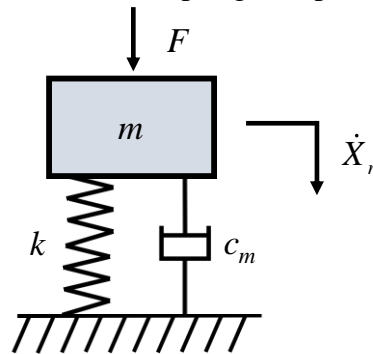
The combination of the mechanical elements forms the SDOF mass-spring-damper, shown in Fig. 8, where F is the amplitude of the driving acting force, \dot{X}_b is the amplitude of the base

velocity and \dot{X}_m is the complex amplitude of the velocity of the suspended mass. The impedance of this mechanical system is the parallel impedance of the stiffness and the damper, which together are in series with the mass impedance. The total impedance of the device is given by

$$Z_D = \frac{1}{\frac{1}{Z_m} + \left(\frac{1}{Z_k} + \frac{1}{Z_{c_m}} \right)}. \quad (1)$$

The SDOF base excited system shown in Fig. 8 can be represented, after some mathematical manipulation, as a function of its relative velocity, i.e. $\dot{X}_r = \dot{X}_m - \dot{X}_b$, and the resulting mechanical system will behave as a force excited SDOF system. An example of the mechanical system is shown in Fig. 9, where the amplitude of the driving force, F , is interpreted as $F = -m\ddot{X}_b$, which is the acceleration of the base of the device shown in Fig. 8.

Figure 9. Example of a force excited SDOF mass-spring-damper system.



Source: author.

The total impedance of the mechanical system is given by

$$Z_D = Z_m + Z_{c_m} + Z_k, \quad (2)$$

which are the parallel impedances of the mass, the damping and the spring. Substituting the impedance for each mechanical element given in Tab. 4 into Eq. (2), the total impedance of the device is

$$Z_D = j\omega m - \frac{jk}{\omega} + c_m, \quad (3)$$

or in non-dimensional form as

$$\frac{Z_D}{c_{c_m}} = \frac{2\zeta_m \Omega + j(\Omega^2 - 1)}{2\Omega} \quad (4)$$

where $\Omega = \omega/\omega_n$ is non-dimensional excitation frequency, ω_n is the undamped natural frequency, $\zeta_m = c_m/c_{c_m}$ is the damping ratio and $c_{c_m} = 2m\omega_n$ is the critical mechanical damping.

The mobility is the ratio between the resulting velocity with the driving forcing acting on the element and it is the inverse of the element impedance. Then, the device mobility is given by

$$Y_D = \frac{1}{j\omega m - \frac{j}{\omega k} + c_m}, \quad (5)$$

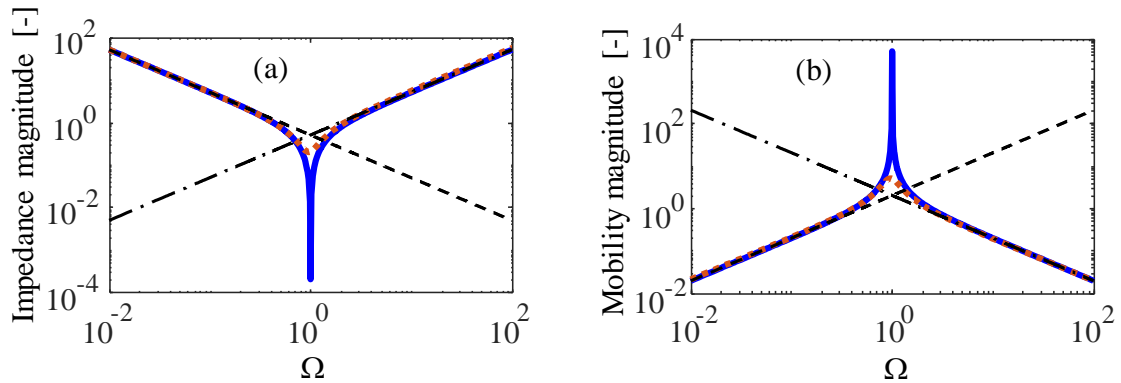
or in non-dimensional form

$$Y_D c_{c_m} = \frac{2\Omega}{2\zeta_m \Omega + j(\Omega^2 - 1)}. \quad (6)$$

Examples of the non-dimensional impedance of the device given by Eq. (4), and the non-dimensional mobility, Eq. (6), for two different damping ratios are shown in Fig. 10. The non-dimensional mass lines impedance (mobility), $\frac{Z_m}{c_{c_m}} = \frac{j\Omega}{2}$ ($Y_m c_{c_m} = \frac{-2j}{\Omega}$) and stiffness line impedance (mobility), $\frac{Z_k}{c_{c_m}} = \frac{-2j}{\Omega}$ ($Y_k c_{c_m} = j2\Omega$), are also shown in Fig. 10.

Figure 10 (a) and (b) show, respectively, the non-dimensional impedance and mobility of the SDOF mass-spring-damper mechanical system for two different damping ratios. It can be seen from the impedance (mobility) of the device is large (small) at, both, low and high frequencies. Moreover, at low frequency, the impedance (mobility) is controlled by the device stiffness, while at high frequency the impedance (mobility) is controlled by the device mass. The impedance (mobility) is small (large) when the device is operating at its resonance, i.e. $\Omega = 1$. At this frequency, the impedance (mobility) is controlled by the device damping and it becomes larger (smaller) as the damping ratio is increased.

Figure 10. Example of the non-dimensional device impedance (a) and mobility (b) for two different mechanical damping ratio: $\zeta_m = 0.001$ (blue solid line, —); and $\zeta_m = 0.1$ (red dotted line, ···). The black dash-dot line, - · -, is the mass line and the black dashed line, - - -, is the stiffness line.



Source: author.

In Fig. 10 it is seen that at the resonance frequency the magnitude of the non-dimensional impedance (mobility), in which $\frac{Z_D}{c_m} = \zeta_m$ ($Y_D c_m = \frac{1}{\zeta_m}$), is less (greater) than 1. This means that apart from this being the frequency at which the maximum transmissibility of the base vibration to the suspended mass occurs, the transmitted vibration is also amplified. From the point of view of an energy harvesting device, which harvests energy from the oscillation of the suspended mass, a small damping ratio ($\zeta_m \rightarrow 0$) is desirable, so that the mobility tends to infinity ($Y_D c_m \rightarrow \infty$). However, this leads to a large relative velocity ($\dot{X}_r \gg 1$) and, consequently, to a large relative displacement ($X_r \gg 1$) which will make the device constrained to its housing size. Then, the optimum damping ratio would be $\zeta_{m,opt} = X_b / 2X_{r,max}$, which is the ratio between the base displacement and the maximum relative displacement.

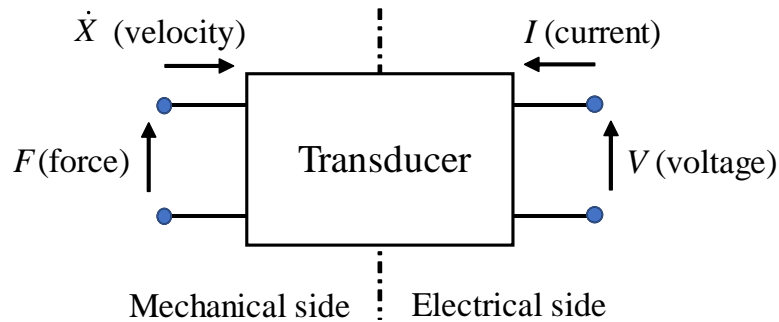
3.3 THE TWO-PORT NETWORK: A MODEL FOR A PIEZOELECTRIC AND AN ELECTROMAGNETIC TRANSDUCER

In the last section, the mechanical impedance of a SDOF mass-spring-damper system was discussed and it was shown that each mechanical element has a contribution to the impedance (mobility) of the device. An energy harvesting device is an electromechanical system, i.e., it has mechanical and electric elements and each of these elements, including the electrical ones, will have a contribution to the total impedance of the electromechanical transducer.

The concept of electromechanical functionality is simple. The transducer oscillation due to a driving harmonic force generates an internal voltage. The transducer internal electric components, when subject to this voltage, generates a feedback force changing the behaviour of the oscillator. The same behaviour is observed in the opposite process. When a driving voltage is applied to the electromechanical system, the electric components generate a feedback force which will cause a force which in turn, generates a voltage in the opposite direction. A simple way to describe mathematically the electromechanical behaviour is using a two-port network model. This model, which connect two external circuits, describes by a 2-2 matrix of impedances the behaviour of any type of mechanical, electrical or electromechanical system, i.e., the behaviour of an energy harvester.

A two-port model of a transducer is shown in Fig. 11. At one side of the two-port electromechanical transducer is the mechanical port, which connects the SDOF base excited system given in Fig. 9. This mechanical port is defined by the driven force F and the resulting velocity \dot{X} and is responsible to generate the transducer motion. The other side is the electrical port which connects the internal transducer elements. This electrical port is defined by the generated voltage V and the resulting current I .

Figure 11. Schematic of a two-port model of a transducer



Source: author.

The two-port electromagnetic transducer is used to investigate the effects of the electromechanical interactions and the potential power that can be delivered to the attached electrical load. Moreover, in this section, a comparative study between piezoelectric and electromagnetic energy harvesters is presented. The source of vibration (the driving force) and the resulting velocity in Fig. 9 are $F = -m\ddot{X}_b$ and $\dot{X} = \dot{X}_r$. As seen in the previous section, the oscillation of the suspended mass is maximized and, consequently, more energy is delivered to

the electrical side when the impedance (mobility) is minimum (maximum), which occurs at the resonance frequency.

The frequency domain matrix equation for a two-port electromechanical transducer shown in Fig. 11 is given by (WOOLLETT, 1966)

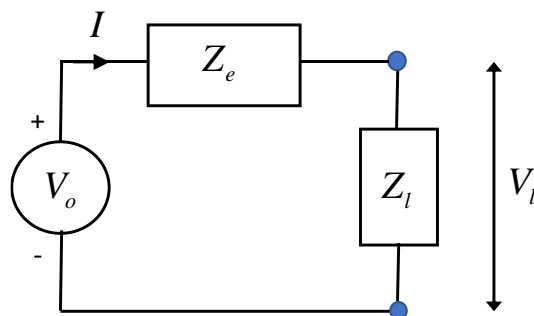
$$\begin{Bmatrix} F \\ V \end{Bmatrix} = \begin{bmatrix} Z_D^I & Z_{me} \\ Z_{em} & Z_e \end{bmatrix} \begin{Bmatrix} \dot{X} \\ I \end{Bmatrix}, \quad (7)$$

where V is the voltage generated and I is the resulting current. The impedances, given in the matrix elements of Eq. (7), are specific for each transducer mechanism (here they are piezoelectric and electromagnetic). However, their physical meaning and effects are not different. Z_D^I is the open-circuit mechanical impedance ($I = 0$), Z_e is the blocked electrical impedance ($\dot{X} = 0$), i.e., the internal electric transducer impedance and Z_{me} and Z_{em} are the electromechanical transducer impedance, i.e. the impedance of the element that transfers energy from the mechanical to the electrical side and vice-versa.

3.3.1 Equivalent Electrical System

The energy generated by the vibrating source only can be scavenged when an electrical load is connected to the transducer terminals on the electrical side in Fig. 11. The equivalent electrical circuit is shown in Fig. 12 for a voltage source in series with the internal impedance and the load impedance.

Figure 12. The equivalent electrical circuit of the transducer connected to an electrical load.



Source: author.

Where V_o is the voltage generated due to the device motion, Z_e is the internal impedance of the transducer and Z_l and V_l are the impedance and the voltage across the electrical load,

respectively. When the electrical load impedance is large ($Z_l \rightarrow \infty$), the circuit behaves like its terminals are open and no current flows in the circuit, $I_o = 0$. The open-circuit voltage, from Eq. (7) is given by

$$V_o = Z_{em} \dot{X} . \quad (8)$$

When the load impedance is small, so that $Z_l \rightarrow 0$, the circuit behaves like the terminals are connected without any load. Then, the closed-circuit current is given by

$$I_c = -\frac{Z_{em} \dot{X}}{Z_e} . \quad (9)$$

Note that the coupling condition between the transducer and the load is $V_l = -V$. Substituting the voltage across the electrical impedance load, $V_l = Z_l I$, into Eq. (7), the resulting current is given by

$$I = -\frac{Z_{em}}{Z_l + Z_e} \dot{X} \quad (10)$$

and the transducer total mechanical impedance is

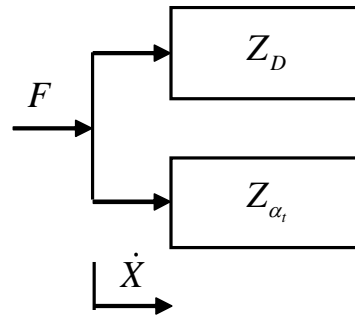
$$Z_t = \frac{F}{\dot{X}} = Z_D^I - \frac{Z_{me} Z_{em}}{Z_l + Z_e} . \quad (11)$$

It can be noted in Eq. (10) that the resulting current amplitude is a function of the chosen load and the resulting velocity. From Eq. (11) it can also be noted that the feedback force, due to electrical effect interactions, changes the total mechanical impedance of the transducer.

3.3.2 Equivalent Mechanical System

The equivalent electrical system shows that when an electrical load is connected to the transducer, the electrical side has an important contribution to the total transducer impedance. The transducer model has an equivalent mechanical system as shown in Fig. 13.

Figure 13. Equivalent mechanical model for the transducer connected to an electrical load.



Source: author.

From Eq. (11), the impedance of the transducer coupled to an electrical load, shown in Fig. 13 is given by

$$Z_t = \frac{F}{\dot{X}} = Z_D + Z_{\alpha_t}, \quad (12)$$

where $Z_D = Z_D^l$ and

$$Z_{\alpha_t} = -\frac{Z_{me}Z_{em}}{Z_l + Z_e}. \quad (13)$$

3.3.2.1 Piezoelectric transducer

A piezoelectric transducer is a reciprocal transducer (NAKANO; ELLIOTT; RUSTIGHI, 2007; WOOLLETT, 1966) and its electro-mechanical impedance is given by

$$Z_{me} = Z_{em} = TZ_e \quad (14)$$

whose open-circuit mechanical impedance is given by

$$Z_D^l = Z_D^E + \frac{Z_{em}Z_{me}}{Z_e} = Z_D^E + T^2Z_e, \quad (15)$$

where Z_D^E is the closed-circuit mechanical impedance, which is the transducer impedance without the electric effects into the mechanical side, Eq. (2). For the piezoelectric transducer Z_D^E is

$$Z_D^E = Z_m + Z_{c_m} + Z_k. \quad (16)$$

Substituting Eqs. (13), (15) and (16) into Eq. (12) and with some manipulation, the piezoelectric total impedance is given by

$$Z_p = \text{Re}\{Z_D\} + T^2 \text{Re}\left\{\frac{Z_e Z_l}{Z_l + Z_e}\right\} + j \left(\text{Im}\{Z_D\} + T^2 \text{Im}\left\{\frac{Z_e Z_l}{Z_l + Z_e}\right\} \right), \quad (17)$$

where $\text{Re}\{\dots\}$ and $\text{Im}\{\dots\}$ denotes the real and the imaginary parts, respectively. In the particular case $Z_e = -j/\omega C_p$ and $Z_l = R_l$, which are respectively the internal piezoelectric capacitive impedance and the resistive load impedance, resulting in

$$Z_p = c_m + \frac{R_l T^2}{1 + \omega^2 R_l^2 C_p^2} + j \left(\omega m - \frac{k}{\omega} - \frac{\omega R_l^2 T^2 C_p}{1 + \omega^2 R_l^2 C_p^2} \right). \quad (18)$$

It can be noted in Eq. (18) that when the load resistance is connected to the piezoelectric transducer, the electrical feedback effect introduces a real and an imaginary term to the transducer total impedance. The real term is positive and acts like an analogous electrical damping. The imaginary term is negative and acts like an equivalent electrical stiffness.

3.3.2.2 Electromagnetic transducer

An electromagnetic transducer is an anti-reciprocal transducer (DAL BO; GARDONIO, 2018; WOOLLETT, 1966) and its electro-mechanical impedance is

$$Z_{me} = -Z_{em} = T \quad (19)$$

And the open-circuit mechanical impedance is given by

$$Z_D^I = Z_D^E - \frac{T^2}{Z_e}, \quad (20)$$

where Z_D^E is the closed-circuit mechanical impedance. Different from the piezoelectric transducer, the device mechanical impedance, i.e. the total impedance without the influence of the electrical effects, occurs in the open-circuit condition which gives

$$Z_D^I = Z_D = Z_m + Z_{c_m} + Z_k. \quad (21)$$

Substituting Eqs. (13), (19) and (21) into Eq. (12) and with some manipulation, the total impedance of the electromagnetic transducer is

$$Z_M = \operatorname{Re}\{Z_D\} + \frac{T^2 \operatorname{Re}\{Z_l + Z_e\}}{|Z_l + Z_e|^2} + j \left(\operatorname{Im}\{Z_D\} - \frac{T^2 \operatorname{Im}\{Z_l + Z_e\}}{|Z_l + Z_e|^2} \right). \quad (22)$$

In the particular case $Z_e = j\omega L_o$ and $Z_l = R_l$, which are respectively the internal inductance and the resistive load impedances, which results in

$$Z_M = c_m + \frac{R_l T^2}{R_l^2 + \omega^2 L_o^2} + j \left(\omega m - \frac{k}{\omega} + \frac{\omega L_o T^2}{R_l^2 + \omega^2 L_o^2} \right). \quad (23)$$

It can be seen in Eq. (23) that, similar to the piezoelectric transducer, when the load resistance is connected to the electromagnetic transducer, the electrical feedback effect introduces a real and an imaginary terms to the total transducer impedance. The real term is positive and acts like an analogous electrical damping and the imaginary term is positive and in-phase with the mass, which means it acts like an equivalent electrical mass.

3.3.3 The electrical power dissipated by the transducer

As mentioned earlier, in accordance with Eq. (4), the maximum vibration transmitted from the device base to the suspended mass occurs when the transducer resonance frequency coincides with the source excitation frequency. Moreover, the transducer mechanical damping should be small, $\zeta_m \rightarrow 0$ so that $Z_D \rightarrow 0$ ($Y_D \rightarrow \infty$). In this section, the impedance of the

transducer is assumed to be operating at the device resonance frequency, i.e. $\text{Im}\{Z_t\}=0$, and with no mechanical damping, $\text{Re}\{Z_D\}=0$, which is the ideal case for energy harvesting purposes. The power dissipated by the transducer is given by (HARRIS; PIERSOL, 2002)

$$P_t = \frac{1}{2} \text{Re}\{F \dot{X}^*\}, \quad (24)$$

where $\{*\}$ represents the complex conjugate. The power can also be written as

$$P_t = \frac{1}{2} |F|^2 \text{Re}\{Y_t\} \quad (25)$$

in which, Eq. (25) is the square of the input power multiplied by the transducer mobility.

3.3.3.1 Electrical power dissipated by the piezoelectric energy harvester

Considering the electromechanical coefficient $T = \theta$ and the assumptions, $\text{Im}\{Z_p\} = 0$ and $\text{Re}\{Z_D\} = 0$, and substituting Eq. (17) into Eq. (25), the electrical power dissipated by the piezoelectric transducer electrical damping normalized by the square of the base vibration is given by

$$\hat{P}_p = \frac{P_p}{\frac{1}{2} |m\ddot{X}_b|^2} = \frac{\omega^2 R_t^2 C_p^2 + 1}{\theta^2 R_t}. \quad (26)$$

It can be seen from Eq. (26), that the power dissipated by the piezoelectric transducer is large when $\omega \gg 1$, i.e. for high excitation frequencies.

3.3.3.2 Electrical power dissipated by the electromagnetic energy harvester

Considering the electromechanical coefficient is $T = Bl$, which B is the magnetic flux density and l is the coil length, and the assumptions, $\text{Im}\{Z_M\} = 0$ and $\text{Re}\{Z_D\} = 0$, and substituting Eq. (22) into Eq. (25), the electrical power dissipated by the electrical damping of the electromagnetic transducer normalized by the square of the base vibration is given by

$$\hat{P}_M = \frac{P_M}{\frac{1}{2} |m\ddot{X}_b|^2} = \frac{R_l^2 + \omega^2 L_o^2}{(Bl)^2 R_l}. \quad (27)$$

3.3.3.3 Comparison between the power dissipated by piezoelectric and electromagnetic energy harvesting devices

The ratio between the power dissipated by electromagnetic and piezoelectric energy harvester device is

$$P_r = \frac{\hat{P}_M}{\hat{P}_p}. \quad (28)$$

Substituting Eqs. (26) and (27) into Eq. (28), the ratio between the electromagnetic and piezoelectric energy harvesting devices result in

$$\hat{P}_r = P_r \frac{(Bl)^2}{\theta^2} = \frac{R_l^2 + \omega^2 L_o^2}{1 + \omega^2 R_l^2 C_p^2}. \quad (29)$$

There are two electrical circuits conditions at which electromechanical transducers can operate: at short and open circuits. Then, when in short-circuit ($R_l \rightarrow 0$), the ratio between the power dissipated, Eq. (29), is

$$\hat{P}_{r,SC} \approx L_o^2 \omega^2. \quad (30)$$

When in open-circuit ($R_l \rightarrow \infty$), the ratio between power dissipated, Eq. (29), is

$$\hat{P}_{r,OC} \approx \frac{1}{C_p^2 \omega^2}. \quad (31)$$

Note from Eq. (30), for a small ω , since $L_o \ll 1$, the ratio between dissipated powers results in $\hat{P}_{r,SC} < 1$. This means that, at short-circuit condition and at low frequency, the piezoelectric transducer dissipates more energy than the electromagnetic transducer. From Eq. (31), for a small ω , since $C_p \ll 1$, the ratio between dissipated powers result in $\hat{P}_{r,OC} > 1$. This

means that, at open-circuit and at low frequency, the electromagnetic transducer dissipates more energy than the piezoelectric transducer.

In order to determine which transducer performs better in low frequency, if it is the piezoelectric transducer in short-circuit or the electromagnetic transducer in open-circuit, the product between the ratio dissipated powers is calculated by

$$\hat{P}_{r,\omega\rightarrow 0} = \hat{P}_{r,SC} \cdot \hat{P}_{r,OC} \quad (32)$$

Where, since at low frequency $\hat{P}_{r,SC} < 1$ and $\hat{P}_{r,OC} > 1$, if $\hat{P}_{r,\omega\rightarrow 0} > 1$, the electromagnetic transducer dissipates more energy. Otherwise, if $\hat{P}_{r,\omega\rightarrow 0} < 1$, the piezoelectric transducer dissipates more energy. Substituting Eq. (30) and (31) into Eq. (32) gives

$$\hat{P}_{r,\omega\rightarrow 0} = \frac{L_o^2}{C_p^2} \quad (33)$$

As the magnitude of the piezoelectric internal capacitance, C_p , is generally known to be lower than the magnitude of the electromagnetic internal inductance, L_o , and both are lower than unity, $C_p \ll L_o \ll 1$, the product between the ratios of the dissipated powers, Eq. (33), is $\hat{P}_{r,\omega\rightarrow 0} > 1$. This suggest that, in low frequency, the electromagnetic transducer performs better than the piezoelectric. This suggest that to harvest the low frequencies of the sleeper vertical vibrations induced due to a pass-by train, investigated in Chapter 2, the electromagnetic transducer will be preferable.

3.4 ELECTROMAGNETIC DEVICE: BASE EXCITED MASS-SPRING-DAMPER LINEAR OSCILLATOR

As discussed in the previous section, a SDOF mass-spring-damper is used to model an oscillator which can convert mechanical energy from vibrating energy into electrical energy. This was first proposed by Williams and Yates (1996). Since then, much research, for example Stephen (2006a), have used this model mostly to study electromagnetic, piezoelectric and electrostatic generators.

Since the early studies on energy harvesting from vibration, most researchers have conducted their analysis based on harmonic base excitation for an unlimited time, i.e., steady-

state vibration, (AMIRTHARAJAH; CHANDRAKASAN, 1998; ROUNDY, 2005; SAHA *et al.*, 2008; WILLIAMS; YATES, 1996). However, depending on the vibrating source, the transient responses could be more dominant than the steady-state response. Gatti *et al.* (2016) presented an approximate equation for an energy harvester considering both the transient and steady-state condition. They showed that the transient response has a detrimental effect on the harvester performance and to disregard its effects leads to a wrong interpretation of the performance of the device.

This section presents a discussion on the operating conditions in which it will be possible to dissipate the maximum amount of electric energy for an initial transient plus steady state response. Different to that investigated by Gatti *et al.* (2016) and Brennan *et al.* (2017a), the transduction mechanism is considered here and the amount of energy dissipated by the electrical load is investigated.

3.4.1 Existing model

An example of a linear electromagnetic energy harvesting transducer is shown in Fig. 14. It is usual to represent the electrical circuit with a coil which has internal resistance, R_o , and inductance, L_o . In this investigation, however, the coil internal inductance is neglected as its impedance is low (7 Ohm) compared to the coil internal resistance (369 Ohm).

The governing equation for the transducer shown in Fig. 14 is given by (STEPHEN, 2006a)

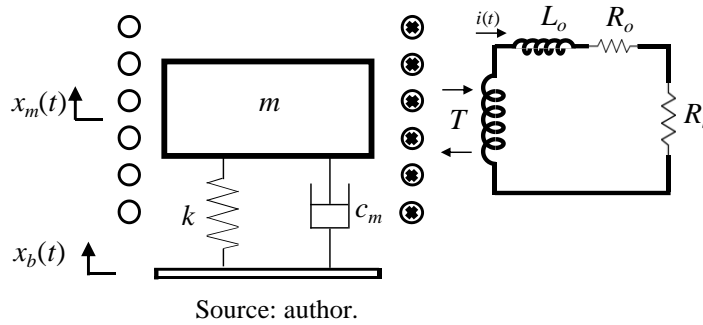
$$m\ddot{x}_r(t) + c_m\dot{x}_r(t) + kx_r(t) + Ti(t) = -m\ddot{x}_b(t) \quad (34a)$$

$$v(t) = -T\dot{x}_r(t) + L_o \frac{di(t)}{dt} + R_o i(t) \quad (34b)$$

where m is the seismic mass, c_m is the mechanical viscous damping, k is the transducer stiffness, $T = Bl$ is the electromechanical constant², in which B is the magnetic flux density and l is the coil effective length; v is the voltage across the transducer terminals, i is the resulting current, $x_r(t) = x_m(t) - x_b(t)$ is the relative displacement of the suspended mass, t is time and the overdots denotes time derivation.

² More detail about the magnetic flux density and the coil characteristic length can be find in (DAL BO; GARDONIO, 2018)

Figure 14. Example of an electromagnetic energy harvesting transducer.



When a load resistance is attached to the transducer terminals, the voltage across the load resistance is given by

$$v_l(t) = -v(t) = R_l i(t). \quad (35)$$

Assuming $L_o = 0$ and substituting Eq. (35) into Eq. (34b) to give

$$i(t) = \frac{T}{R_l + R_o} \dot{x}_r(t) \quad (36)$$

and substituting Eq. (36) into Eq. (34a), with some manipulation, gives the general equation for the electromagnetic transducer motion, which is

$$m\ddot{x}_r(t) + c_{eq}\dot{x}_r(t) + kx_r(t) = -m\ddot{x}_b(t), \quad (37)$$

where $c_{eq} = c_m + c_e$ is the equivalent damping and $c_e = T^2/(R_l + R_o)$ is the analogue equivalent electrical damping. Moreover, normalizing the electrical damping by the critical mechanical damping, $c_{c_m} = 2m\omega_n$, gives

$$\zeta_e = \frac{c_e}{c_{c_m}} = \frac{T^2}{2m\omega_n(R_l + R_o)} \quad (38)$$

and the equivalent electrical damping ratio can be rewritten as

$$\zeta_e = \frac{\zeta_R \zeta_{R_o}}{\zeta_R + \zeta_{R_o}}, \quad (39)$$

which is the analogous damping ratio of the load resistance, which is referred to as the load resistance damping ratio,

$$\zeta_R = \frac{T^2}{2m\omega_n R_l}, \quad (40)$$

in series with the analogous damping ratio of the internal coil resistance, which is referred to as the internal coil resistance damping ratio,

$$\zeta_{R_o} = \frac{T^2}{2m\omega_n R_o}. \quad (41)$$

The equivalent damping ratio in the electromagnetic transducer is then $\zeta_{eq} = \zeta_m + \zeta_e$.

Consider, now, that the vibrating source excites the base of the device with a periodic harmonic excitation $x_b(t) = X_b \sin(\omega t)$ and assuming zero initial conditions, the full solution of the differential equation of motion, Eq. (37), is given by (RAO, 2010)

$$x_r(t) = \left| \frac{X_b \omega^2}{\omega_n^2 - \omega^2 + 2j\zeta_{eq}\omega\omega_n} \right| \left(\sin(\omega t + \phi) - \frac{\omega}{\omega_d} e^{-\zeta_{eq}\omega_n t} \sin(\omega_d t + \eta) \right), \quad (42)$$

where

$$\phi = -\text{atan} \left(\frac{2\zeta_{eq}\omega\omega_n}{\omega_n^2 - \omega^2} \right), \quad \eta = -\text{atan} \left(\frac{2\omega_n^2 \zeta_{eq} \sqrt{1 - \zeta_{eq}^2}}{\omega_n^2 - \omega^2 - 2\omega_n^2 \zeta_{eq}^2} \right), \quad \omega_d = \omega_n \sqrt{1 - \zeta_{eq}^2} \quad \text{and} \quad j = \sqrt{-1}.$$

For the case when the damping is light, $\zeta_{eq} \ll 1$, and the source is exciting the device undamped natural frequency, $\omega = \omega_n$, the relative displacement in Eq. (42) can be written as

$$x_r(t) \approx \frac{X_b}{2\zeta_{eq}} \left(1 - e^{-\zeta_{eq}\omega_n t} \right) \sin(\omega_n t). \quad (43)$$

The solution of the electromagnetic transducer equation of motion, Eq. (37) for a non-dimensional time $\tau = \omega_n t$ is given by

$$x_r(\tau) = \frac{X_b \Omega^2}{\sqrt{(1-\Omega^2)^2 + 4\zeta_{eq}^2 \Omega^2}} \left[\cos(\Omega\tau - \bar{\phi}) - \frac{e^{-\zeta_{eq}\tau}}{\sqrt{1-\zeta_{eq}^2}} \cos(\sqrt{1-\zeta_{eq}^2}\tau - \bar{\eta}) \right], \quad (44)$$

where

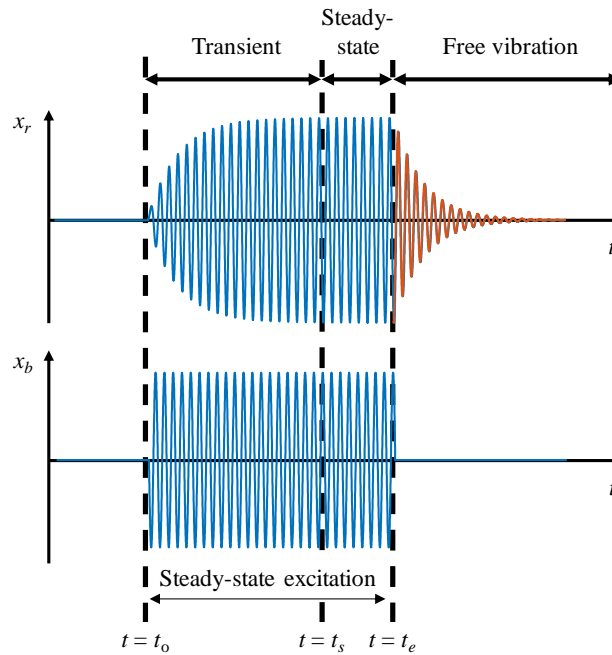
$$\bar{\phi} = -\text{atan}\left(\frac{2\Omega\zeta_{eq}}{1-\Omega^2}\right) \text{ and } \bar{\eta} = -\text{atan}\left(\frac{2\zeta_{eq}\sqrt{1-\zeta_{eq}^2}}{1-\Omega^2-2\zeta_{eq}^2}\right).$$

For light damping, when $\zeta_{eq}^2 \ll 1$ and $\Omega = 1$, Eq. (44) simplifies to

$$x_r(\tau) = \frac{X_b}{2\zeta_{eq}} (1 - e^{-\zeta_{eq}\tau}) \sin(\tau). \quad (45)$$

An example of the electromagnetic transducer when subject to time-limited harmonic excitation is shown in Fig. 15. The behaviour of the electromagnetic transducer can be split into three phases. During the period when the device is excited, the transient phenomenon is observed, which may be followed by the steady-state response and, then, the free vibration when the excitation ceases.

Figure 15. Energy harvester subject to time-limited harmonic excitation.



Source: adapted from GATTI *et al.* (2016).

3.4.2 Energy dissipated by the load resistance

When subject to an excitation source, a mechanical system dissipates energy through mechanical damping. In an electromechanical system operating at its resonance frequency, part of the energy introduced by the excitation source is dissipated by the mechanical damping (c_m) and the other part by the equivalent electrical damping (c_e). However, only the energy dissipated by the electrical load is useful as a source of electric energy. The expression for the electrical energy is given by (STEPHEN, 2006a)

$$E_{elec}(t) = \int_{t_o}^{t_e} v(t)i(t)dt. \quad (46)$$

Considering the electromagnetic energy harvester in Fig. 14 and substituting Eqs. (35) and (36) into Eq. (46), the energy dissipated by the electrical resistance during the excitation period is given by

$$E_{elec}(n) = \frac{\omega_n R_l T^2}{(R_l + R_o)^2} \int_{\tau_o}^{\tau_e} \left(\frac{\partial x_r(\tau)}{\partial \tau} \right)^2 d\tau. \quad (47)$$

Substituting the derived form of Eq. (45), into Eq. (47) and integrating the expression for a non-dimensional time $\tau_o = 0$ to $\tau_e = 2\pi n/\Omega$, where n is the number of cycles at a time t_e , results in the energy dissipated by the electrical resistance normalized by the kinetic energy of the suspended mass

$$\hat{E}_{elec}(n) = \frac{E_{elec}(n)}{\frac{1}{2} m \dot{X}_b^2} = \frac{\zeta_e^2}{\zeta_R} \left\{ \left(\frac{\pi n}{\zeta_{eq}^2} \right) - \left[\frac{3 + e^{-4\pi n \zeta_{eq}} - 4e^{-2\pi n \zeta_{eq}}}{4\zeta_{eq}^3} \right] \right\}. \quad (48)$$

Note that Eq. (48) is function of three damping ratios: the equivalent electrical damping ratio, ζ_e , the load resistance damping ratio, ζ_R , and the equivalent transducer damping ratio ζ_{eq} . To understand the physical significance of Eq. (48), the various terms of the equation are evaluated individually.

3.4.2.1 Time-limited periodic excitation: steady-state condition

Examining the time-history of the suspended mass in Fig. 15, it can be noted that it takes time t_s for the oscillating mass to achieve steady-state. If the transducer stays for n cycles in the steady-state, the normalized energy dissipated by the electrical resistance is

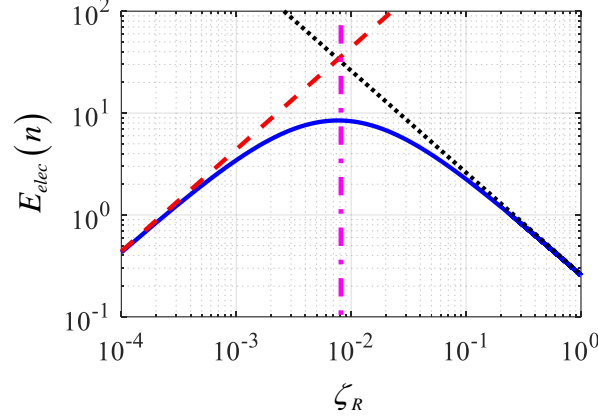
$$\hat{E}_{elec} = \frac{\pi n \zeta_e^2}{\zeta_R \zeta_{eq}^2}, \quad (49)$$

which is the term in the round brackets of Eq. (48). Also, it is noted that if $\pi n \zeta_{eq} \rightarrow \infty$, the term inside the square brackets tends to zero, which means that almost all the energy dissipated is due to the steady-state response. This condition may occur when the steady-state excitation is considered so that n is infinitely large, or the equivalent damping ratio, ζ_{eq} , is large. Moreover, note that Eq. (49) is still a function of the three transducer damping ratios and a closed-form expression cannot be determined. Thus, Eq. (49) is better investigated in its expanded form

$$\hat{E}_{elec} = \frac{\zeta_R \zeta_{R_o}^2}{(\zeta_R + \zeta_{R_o})^2} \left[\frac{\pi n}{\left(\zeta_m + \frac{\zeta_R \zeta_{R_o}}{\zeta_R + \zeta_{R_o}} \right)^2} \right]. \quad (50)$$

Equation (50) is plotted in Fig. 16 as a function of ζ_R . It is easily seen that for a given ζ_m and ζ_{R_o} there is an optimum solution for ζ_R in which the transducer dissipates its maximum electrical energy. Determination of an expression for the optimum solution for Eq. (50) it is not possible. However, from the graph, it can be noted that there are two asymptotes for $\zeta_R \gg 1$ and $\zeta_R \ll 1$, which means that for a given resistance the system is in, respectively, closed and open circuit condition.

Figure 16. Normalized electrical energy dissipated by the load resistance as a function of ζ_R for $\pi n \zeta_{eq} \gg 1$ ($\zeta_m = 0.2$, $\zeta_{R_o} = 0.008$ and $n = 56$). Red dashed line, $- -$, is the asymptote given by $\hat{E}_{elec} \approx \frac{\pi n \zeta_R \zeta_{R_o}}{\zeta_m}$; black dotted line, \cdots , is the asymptote given by $\hat{E}_{elec} \approx \frac{\pi n \zeta_{R_o}^2}{\zeta_R (\zeta_m + \zeta_{R_o})^2}$; and the vertical magenta dash-dotted line, $- \cdot -$, is the for $\zeta_{R,opt} = \frac{\zeta_m \zeta_{R_o}}{\zeta_m + \zeta_{R_o}}$.



Source: author.

When $\zeta_R \gg 1$, Eq. (50) becomes

$$\hat{E}_{elec} = \frac{\pi n \zeta_{R_o}^2}{\zeta_R (\zeta_m + \zeta_{R_o})^2}, \quad (51)$$

and when $\zeta_R \ll 1$, Eq. (50) becomes,

$$\hat{E}_{elec} = \frac{\pi n \zeta_R}{\zeta_m^2}. \quad (52)$$

and an approximate expression for the optimum solution of Eq. (50) can be determined by setting the two asymptotes to be equal, which is when

$$\zeta_{R,opt} = \frac{\zeta_m \zeta_{R_o}}{\zeta_m + \zeta_{R_o}} \quad (53)$$

or, writing in terms of the load resistance, the optimum condition is when

$$R_{l,opt} = \frac{T^2}{c_m} + R_o. \quad (54)$$

This is the *electrical domain analogous matching* in accordance with Stephen (2006a), the impedance matching condition to transfer the maximum energy to the load resistance (STEPHEN, 2006b). Substituting the optimum electrical resistance damping ratio into Eq. (50) gives

$$\hat{E}_{elec,max} = \frac{\pi n \zeta_{R_o}}{4 \zeta_m (\zeta_m + \zeta_{R_o})} \quad (55)$$

Additionally, in the ideal case, if the electromagnetic transducer has no internal coil resistance ($R_o = 0$), $\zeta_{R_o} \rightarrow \infty$ and then, the optimum electrical resistance damping ratio is simply

$$\zeta_{R,opt} = \zeta_m, \quad (56)$$

or, writing in terms of the load resistance, the optimum condition is when

$$R_{l,opt} = \frac{T^2}{c_m}, \quad (57)$$

which is the *domain matching*, where the mechanical damping is equal to the analogous electrical damping ($c_m = c_e$) in accordance with Stephen (2006a). The maximum electrical energy dissipated is then

$$\hat{E}_{elec,max} = \frac{\pi n}{4 \zeta_m} \quad (58)$$

If the mechanical damping is much greater compared to the internal coil resistance damping ratio, $\zeta_{R_o} \ll \zeta_m$, the load resistance damping ratio which is

$$\zeta_{R,opt} = \zeta_{R_o}, \quad (59)$$

is not the largest source of energy dissipation. However, it is the optimum condition possible. The maximum normalized energy dissipated by the load resistance is then

$$\hat{E}_{elec,max} = \frac{\pi n \zeta_{R_o}}{4 \zeta_m^2}. \quad (60)$$

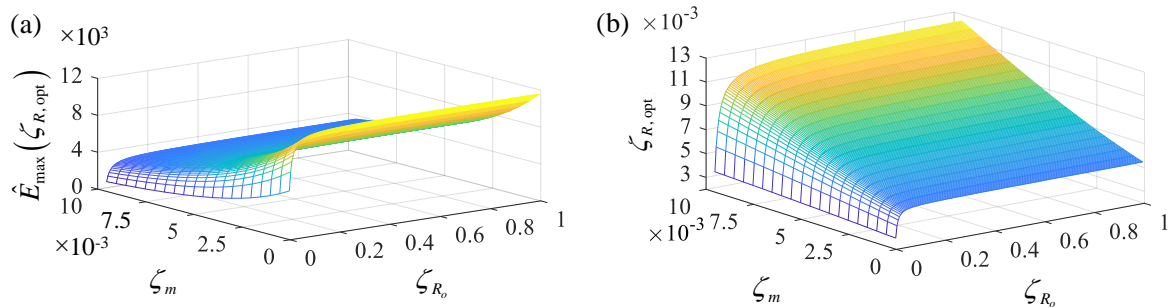
3.4.2.2 Time-limited periodic excitation: transient plus steady-state response

Examining Fig. 15, it can be seen that if both n or ζ_{eq} are not sufficiently large, then the transient response will be relatively long compared to the steady-state response and the transient effects cannot be disregarded. The condition for $\zeta_{eq} \ll 1$ occurs is when ζ_m and ζ_e are much lower than 1. This implies that the terms inside the square brackets of the normalized energy dissipated by the load resistance, which is repeated here for convenience,

$$\hat{E}_{elec}(n, \zeta_R) = \frac{E(n, \zeta_R)}{\frac{1}{2} m \dot{X}_b^2} = \frac{\zeta_e^2}{\zeta_R} \left\{ \left(\frac{\pi n}{\zeta_{eq}^2} \right) - \left[\frac{3 + e^{-4\pi n \zeta_{eq}} - 4e^{-2\pi n \zeta_{eq}}}{4\zeta_{eq}^3} \right] \right\}, \quad (61)$$

has a significant contribution to the energy dissipated. To demonstrate the effects of the damping ratios on the energy dissipated by the load resistance, a numerical investigation is performed. Equation (61) is calculated for $n = 56$ and ranges of the mechanical damping ratio (ζ_m) from 0.0001 to 0.01, of the internal coil resistance damping ratio (ζ_{R_o}) from 0.01 to 1 and of the load resistance damping ratio (ζ_R) from 0.0001 to 0.05. The maximum normalized energy dissipated by the optimum load resistance damping ratio and its respective optimum load resistance damping ratio are plotted in Fig. 17.

Figure 17. (a) Maximum normalized energy dissipated by the optimum load resistance damping ratio; and (b) The corresponding optimum load resistance damping ratio as a function of the internal coil resistance and the mechanical damping ratios for $n = 56$ cycles.



Source: author.

From Fig. 17 it can be seen that both, maximum energy dissipated and the optimum load resistance damping ratio, are influenced by the device damping ratios. Moreover, observe in Fig. 17(a) that the maximum energy occurs when $\zeta_m \ll 1$, i.e., when the device has no mechanical damping. In addition, from the ζ_{R_o} point of view, for a given value of ζ_m , the maximum energy dissipated appears to be constant for some values of ζ_{R_o} , at which may indicate that the device is no longer affected by internal coil resistance. This behaviour is further investigated below.

Note that it is not possible to determine a closed-form expression to the maximum energy dissipated. However, considering some assumptions for ζ_R , an approximate expression to the optimum load resistance damping ratio can be determined and then used to evaluate the energy dissipated. When $\zeta_R \ll 1$, the equivalent electrical damping ratio is $\zeta_e = \zeta_R$ and Eq. (61) becomes

$$\hat{E}_{elec}(n, \zeta_R) = \frac{\pi n \zeta_R}{\zeta_m^2} \left(1 - \frac{3 + e^{-4\pi n \zeta_m} - 4e^{-2\pi n \zeta_m}}{4\pi n \zeta_m} \right). \quad (62)$$

When $\zeta_R \gg 1$, the equivalent electrical damping is $\zeta_e = \zeta_{R_o}$ and Eq. (61) becomes

$$\hat{E}_{elec}(n, \zeta_R) = \frac{\pi n \zeta_{R_o}^2}{\zeta_R (\zeta_m + \zeta_{R_o})^2} \left[1 - \frac{3 + e^{-4\pi n (\zeta_m + \zeta_{R_o})} - 4e^{-2\pi n (\zeta_m + \zeta_{R_o})}}{4\pi n (\zeta_m + \zeta_{R_o})} \right]. \quad (63)$$

Setting Eqs. (62) and (63) to be equal, the matching condition, i.e., the optimum load resistance damping ratio, to maximize the dissipated energy by the electrical load is when

$$\zeta_{R,opt} \approx \frac{\zeta_m \zeta_{R_o}}{\zeta_m + \zeta_{R_o}} \frac{\sqrt{1 - \frac{3 + e^{-4\pi n (\zeta_m + \zeta_{R_o})} - 4e^{-2\pi n (\zeta_m + \zeta_{R_o})}}{4\pi n (\zeta_m + \zeta_{R_o})}}}{\sqrt{1 - \frac{3 + e^{-4\pi n \zeta_m} - 4e^{-2\pi n \zeta_m}}{4\pi n \zeta_m}}}. \quad (64)$$

Although Eq. (64) is not an elegant expression, it is helpful to understand the device behaviour. First, note that if $\pi n \zeta_{eq} \gg 1$, due to $\pi n \zeta_m \gg 1$ and $\pi n \zeta_{R_o} \gg 1$, the square roots in Eq. (64) are unity and then, the optimum load resistance damping ratio is simply given by

$$\zeta_{R,\text{opt}} = \frac{\zeta_m \zeta_{R_o}}{\zeta_m + \zeta_{R_o}}, \quad (65)$$

which is similar to Eq. (53), the solution considering only the steady-state response. Now, when $\zeta_m \rightarrow 0$, in which the transient response is relevant, then Eq. (64) reduces to

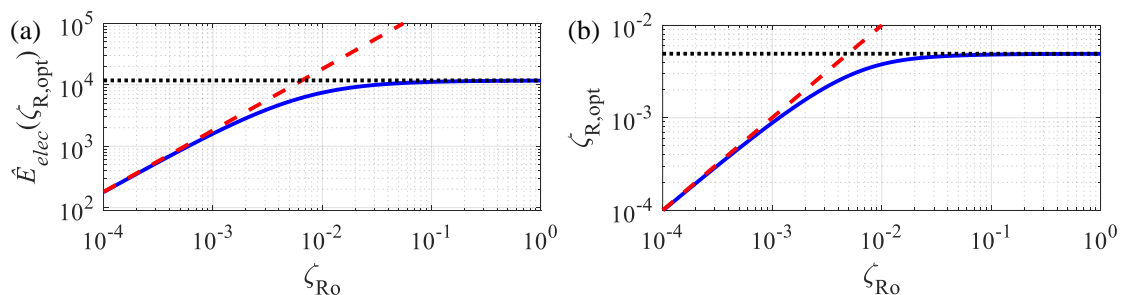
$$\zeta_{R,\text{opt}} \approx \frac{\sqrt{3}}{2\pi n} \sqrt{1 - \frac{3 + e^{-4\pi n \zeta_{R_o}} - 4e^{-2\pi n \zeta_{R_o}}}{4\pi n \zeta_{R_o}}}. \quad (66)$$

Equation (66) indicates that the optimum load resistance damping ratio is no longer dependent on the mechanical damping and the electromagnetic transducer is controlled by the internal coil and load resistances. Combining Eq. (61) with Eq. (66), gives the normalized energy dissipated by the optimum load resistance damping ratio, which is

$$\hat{E}(n, \zeta_{R,\text{opt}}) = \frac{\pi n}{\zeta_{R,\text{opt}}} \left(1 - \frac{3 + e^{-4\pi n \zeta_{e,\text{opt}}} - 4e^{-2\pi n \zeta_{e,\text{opt}}}}{4\pi n \zeta_{e,\text{opt}}} \right) \quad (67)$$

where $\zeta_{e,\text{opt}} = \zeta_{R,\text{opt}} \zeta_{R_o} / (\zeta_{R,\text{opt}} + \zeta_{R_o})$ is the optimum equivalent electrical damping ratio. Equations (66) and (67) are plotted in Fig. 18.

Figure 18. (a) Maximum normalized energy dissipated by the optimum load resistance damping ratio as a function of the internal resistance damping ratio. (b) The corresponding optimum load resistance damping ratio as a function of the internal resistance damping ratio for $\zeta_m \ll 1$ and $n = 56$ cycles. Red dashed line, $- -$, is the asymptote for $\zeta_{R_o} \ll 1$; and black dotted line, $\dots\dots$, is the asymptote for $\zeta_{R_o} \gg 1$.



Source: author.

From Fig. 18, it can be seen that the shape of the maximum normalized energy dissipated has similar behaviour to its corresponding optimum load resistance damping ratio. Both, \hat{E}_{elec} and $\zeta_{R, opt}$ are small for $\zeta_{R_o} \ll 1$ and increases with the increase in ζ_{R_o} up to a constant value. Also, note that there are two asymptotes for $\zeta_{R_o} \ll 1$ and for $\zeta_{R_o} \gg 1$, which, for a given level of internal coil resistance damping ratio, corresponding to a device with a large and small internal impedance. When $\zeta_{R_o} \ll 1$, Eq. (66) gives

$$\zeta_{R, opt} \approx \zeta_{R_o}, \quad (68)$$

and the optimum load resistance is given by

$$R_{l, opt} \approx R_o. \quad (69)$$

Substituting Eqs (68) into (61), gives the maximum normalized energy dissipated by the load resistance for $\zeta_{R_o} \ll 1$ which is

$$\hat{E}_{elec, max}(n, \zeta_{R, opt}) = \frac{(\pi n)^3}{3} \zeta_{R_o}. \quad (70)$$

Equations (70) and (68) are also plotted in Fig. 18(a) and (b), respectively. Note that these equations are the asymptotes for $\zeta_{R_o} \ll 1$. Moreover, Eq. (68) is similar to Eq. (59), when only the steady-state is considered, which means that if $\zeta_{R_o} \ll \zeta_m$, there is a unique optimum load resistance, independently if the transient response is relevant for the total energy dissipated or not. When $\zeta_{R_o} \gg 1$, Eq. (66) becomes

$$\zeta_{R, opt} \approx \frac{\sqrt{3}}{2\pi n} \quad (71)$$

and Eq. (61), with some manipulation, becomes

$$\tilde{E}(\pi n \zeta_R) = \frac{\hat{E}_{elec}(n, \zeta_R)}{(\pi n)^2} = \left(\frac{1}{\pi n \zeta_R} \right) - \left[\frac{3 + e^{-4\pi n \zeta_R} - 4e^{-2\pi n \zeta_R}}{(2\pi n \zeta_R)^2} \right]. \quad (72)$$

Equation (71) is the optimum load resistance damping ratio, the damping match condition to maximize the normalized energy dissipated by the load resistance, Eq. (72). Note that for the ideal electromagnetic energy harvester, i.e., in the absence of mechanical damping and internal coil resistance, the optimum load resistance damping ratio is simply a function of the number of oscillation cycles, n . Moreover, this optimum damping is similar to the one obtained by (GATTI *et al.*, 2016), in which they carried out a fundamental investigation into determining the optimum damping for a device to harvest energy disregarding the device electrical components. Additionally, Gatti *et al.* (2016) observed that a simple rule to determine the optimum damping is then given by

$$\zeta_{R,\text{opt}} \approx \frac{1}{\pi n}. \quad (73)$$

Furthermore, substituting Eq. (73) into (72), the maximum normalized energy dissipated by the load resistance for n oscillation cycles when $\zeta_m \ll 1$ and $\zeta_{R_o} \gg 1$, is found to be

$$\hat{E}_{elec,\text{max}}(n) = (\pi n)^2 \left(\frac{1 - e^{-4} + 4e^{-2}}{4} \right) \approx 0.38(\pi n)^2 \quad (74)$$

Equations (74) and (73) are plotted in Fig. 18(a) and (b), respectively. Observe that they are the asymptotes for $\zeta_{R_o} \gg 1$ and they are constants, which correspond to the maximum energy dissipated and the optimum load resistance damping ratio which the electromagnetic energy harvester can potentially scavenge assuming the ideal conditions, $\zeta_m = 0$ and $R_o = 0$. Moreover, combining Eqs. (68) and (71) gives

$$\zeta_{R_o} = \frac{\sqrt{3}}{2\pi n}. \quad (75)$$

It can be seen in Fig. 18(b) that Eq. (75) is the condition in which both asymptotes lines are the same. This is not an optimum condition for ζ_{R_o} . However, for $\zeta_{R_o} > \frac{\sqrt{3}}{2\pi n}$, the optimum load resistance and the maximum normalized energy dissipated are less sensitive to variations in the level of the internal coil resistance damping ratio. Moreover, when $\zeta_{R_o} > 0.1$, the curve of the energy dissipated approximately achieves its maximum. This is due to $\zeta_{R_o} \gg \zeta_R$, as can be seen in Fig. 18(b) where $\zeta_{R_o}(0.1) \approx 20\zeta_{R,\text{opt}}$, and the equivalent electrical damping ratio, ζ_e , is

controlled by the load resistance. Also, if $\zeta_{R_o} > 0.1$, the electromagnetic energy harvester can be approximate to the condition in which $\zeta_{R_o} \rightarrow \infty$, i.e., the ideal condition in which the internal coil resistance $R_o = 0$. Notwithstanding this assumption is only valid for $\pi n \zeta_{eq} \ll 1$. When $\pi n \zeta_{eq} \gg 1$, based on Eq. (53), the electromagnetic energy harvester can be approximate to an ideal device when $\zeta_{R_o} \gg \zeta_m$.

3.4.3 The energy dissipated by the internal coil resistance

If the electromagnetic energy harvester is not assumed to be ideal, part of the energy delivered to the electrical side is dissipated by the internal coil resistance, which in one oscillation cycle is given by

$$E_{coil}(n) = \frac{\omega_n R_o T^2}{(R_l + R_o)^2} \int_{\tau_o=0}^{\tau_e=\frac{2\pi n}{\Omega}} \left(\frac{\partial x_r(\tau)}{\partial \tau} \right)^2 d\tau. \quad (76)$$

Substituting Eq. (45) into Eq. (76), gives the energy dissipated by the internal coil resistance normalized by the kinetic energy of the base vibration, which is

$$\hat{E}_{coil}(n) = \frac{E_{coil}(n)}{\frac{1}{2} m \dot{X}_b^2} = \frac{\zeta_e^2}{\zeta_{R_o}} \left\{ \left(\frac{\pi n}{\zeta_{eq}^2} \right) - \left[\frac{3 + e^{-4\pi n \zeta_{eq}} - 4e^{-2\pi n \zeta_{eq}}}{4\zeta_{eq}^3} \right] \right\}. \quad (77)$$

3.4.4 The dissipated mechanical energy

As seen previously, if the ideal case is not taken into consideration, i.e. $\zeta_m \neq 0$, part of the energy introduced by the vibrating source is also dissipated by the mechanical damping, which in one oscillation cycle is given by

$$E_{mec}(n) = 2m\omega_n^2 \zeta_m \int_{t_o=0}^{\tau_e=\frac{2\pi n}{\Omega}} \left(\frac{\partial x_r(\tau)}{\partial \tau} \right)^2 d\tau. \quad (78)$$

Substituting Eq. (45) into Eq. (78), gives the expression for the energy dissipated by the mechanical damping normalized by the kinetic energy of the base vibration which is

$$\hat{E}_{mec}(n) = \frac{E_{mec}(n)}{\frac{1}{2}m\dot{X}_b^2} = \zeta_m \left\{ \left(\frac{\pi n}{\zeta_{eq}^2} \right) - \left[\frac{3 + e^{-4\pi n\zeta_{eq}} - 4e^{-2\pi n\zeta_{eq}}}{4\zeta_{eq}^3} \right] \right\}. \quad (79)$$

3.4.5 The total energy available

The total normalized energy available on the electromagnetic energy harvester of Fig. 14, when it is operating at the resonance frequency, comprises the sum of the normalized energies dissipated by the mechanical damping, the load resistance and the internal coil resistance,

$$\hat{E}_{ava} = \hat{E}_{elec} + \hat{E}_{coil} + \hat{E}_{mec}. \quad (80)$$

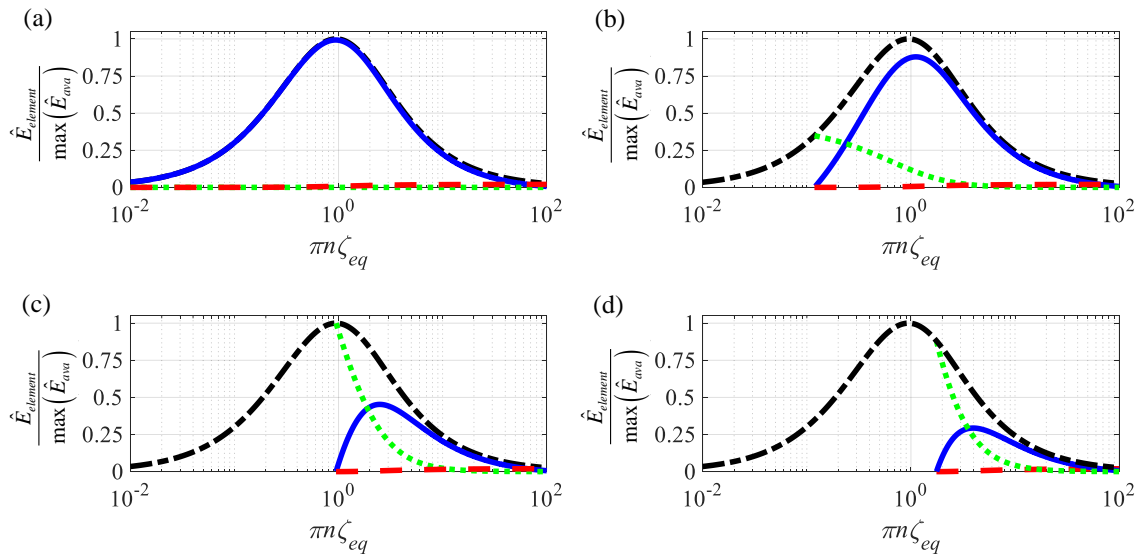
Substituting the normalized energies given in Eqs. (48), (77) and (79) into Eq. (80) to give the normalized total energy available on the electromagnetic energy harvester, at which with some manipulation is given by

$$\hat{E}_{ava}(n) = (\pi n)^2 \left[\frac{1}{\pi n\zeta_{eq}} - \frac{3 + e^{-4\pi n\zeta_{eq}} - 4e^{-2\pi n\zeta_{eq}}}{(2\pi n\zeta_{eq})^2} \right]. \quad (81)$$

Examples of the energy dissipated by the damping elements normalized by the maximum energy available for different electromagnetic transducers operational condition are shown in Fig. 19.

It can be seen in Fig. 19 that the energy dissipated by the load resistance is strongly affected by the damping ratios of the transducer elements. For this particular transducer parameters, by the mechanical damping ratio. Note that the energy available curve is the envelope for the energies dissipated by the transducer elements and as observed by (Gatti *et al.* 2016), the maximum energy available occurs when $\pi n\zeta_{eq} \approx 1$. Moreover, note that due to the detrimental effect of the mechanical damping, the load resistance can harvest the maximum energy available by the vibrating source only when $\zeta_m = 0$. This is shown in Fig. 19(a) where the energy dissipated by the load resistance curve approximately overlays the energy available curve. This occurs because $\zeta_{eq} = \zeta_m + \zeta_e$ and the mechanical damping is the minimum condition for the equivalent damping ratio.

Figure 19. Energy dissipated by each transducer element normalized by the maximum energy available considering $n = 56$ cycles, $\zeta_{R_o} = 0.74$ and: (a) $\zeta_m = 0$; (b) $\zeta_m = \frac{1}{8\pi n}$; (c) $\zeta_m = \frac{1}{\pi n}$; and (d) $\zeta_m = 0.01$. The black dash-dot line, $- \cdot -$, is the total energy available, the blue solid line, $—$, is the energy dissipated by the load resistance; the red dashed line, $- -$, is the energy dissipated by the internal coil resistance; the green dotted line, $\cdot \cdot \cdot$, is the energy dissipated by the mechanical damping.



Source: author.

When $\zeta_m \neq 0$, as shown in Fig. 19(b)-(d), the mechanical damping has a detrimental effect to shift, the maximum energy dissipated by the load resistance, out of the condition at which the maximum energy is available, so that $\pi n \zeta_{eq, opt} > 1$ and less energy is dissipated by the load resistance. In particular, Fig. 19(b) and (c) shows an optimum condition at which both transient and steady-state contributes to the total energy dissipated. Additionally, note in Fig. 19(d) that when $\zeta_m = 0.01$, the transducer performance decreases significantly and the maximum energy dissipated by the load resistance is approximately the same energy dissipated by the mechanical damping. At this condition, due to a relatively high equivalent damping ratio caused by the strong effect of mechanical damping together with the load resistance damping ratio, the transducer response is due to the steady-states response.

3.5 CONCLUSIONS

In this chapter, a two-port network model has been used to characterize the linear SDOF mass-spring-damper electromagnetic and piezoelectric energy harvesters. The investigation has

revealed that when a load resistance is attached to the transducer terminals, the electrical effects introduce an analogous electrical damping which is responsible for harvesting the electrical energy. Moreover, from a simple comparison, it was shown that at low frequency the electromagnetic transducer has a better performance than the piezoelectric transducer.

In practice, in many cases the vibrating source acts for a limited time, implying that both transient and steady state response should be considered. In this study, an approximate analytical model for the energy dissipated by the load resistance attached to an electromagnetic transducer due to time-limited harmonic excitation has been investigated and strategies have been proposed to determine the optimal load resistance damping ratio. It was found that the maximum energy dissipated occurs when $\zeta_{eq} \ll 1$, where the oscillation of the suspended mass does not achieve the steady-state. Also, it has been found that the energy is maximized when the device damping are $\zeta_m \ll 1$ and $\zeta_{R_o} \gg 1$, for a matching condition in which $\zeta_{R,\text{opt}} \approx \frac{1}{\pi n}$. When $\pi n \zeta_{eq} \gg 1$, the oscillation of the suspended mass is due to the steady-state vibration and the matching condition is $\zeta_{R,\text{opt}} = \frac{\zeta_m \zeta_{R_o}}{\zeta_m + \zeta_{R_o}}$, which its optimum load resistance is $R_{l,\text{opt}} = \frac{T^2}{c_m} + R_o$.

Moreover, it was found that if $\zeta_m \ll 1$, the energy dissipated by the load resistance is less sensitive to the variation of the internal coil resistance damping ratio for $\zeta_{R_o} > \frac{\sqrt{3}}{2\pi n}$ and for $\zeta_{R_o} > 0.1$ the internal coil resistance can be neglected and the energy harvester may be approximate to an ideal case. Comparing the energies dissipated by the damping elements, it was found that the load resistance dissipates almost all the energy introduced by the vibrating source when $\zeta_m \ll 1$ and $\zeta_{R_o} \gg 1$.

The study reveals that for the energy harvesting application from a railway track, in which the low frequency vibrations induced due to a passing trains are scavenged, the electromagnetic transducer with a small mechanical damping and a high internal coil resistance damping would be preferable to maximize the device efficiency.

4 THE RAILWAY TRACK VIBRATION EMULATED IN A LABORATORY BASED SYSTEM

4.1 INTRODUCTION

There are several constraints to perform measurements or experiments in a railway environment. The life-risk, the risk to damage the railway line, the difficulty to receive access authorization and the fact that Brazil does not have high-speed trains, are some of the constraints. However, research related to high-speed trains and railways which attempt to improve or develop a device to be incorporated into this environment should be tested on-site or, at least, in an environment which simulate the same desirable conditions.

To overcome those difficulties, researchers have created small-scale railway lines in the laboratory. However, they require a large space to accommodate the equipment. For some applications, which require only part of the railway line physical behaviour (e.g. the railway vibration), this laboratory-based system may exceed the requirements. An alternative way to emulate part of the physical behaviour of the railway environment in the laboratory is to use an electrodynamic shaker to replicate the desirable time waveform.

Time waveform replication has been used previously to emulate desired physical behaviour in the laboratory. The procedure comprises of design a compensator controller, which acts as a filter, to remove, partially (YAO *et al.*, 2019) or totally (SHEN *et al.*, 2016), the effects of the system dynamics so that the system output signal has the desired behaviour.

The use of the compensator filter for time waveform replication has been extensively applied in electrohydraulic shaking tables. Shen *et al.* (2011) proposed an adaptative controller to extend the frequency bandwidth of the electrohydraulic shaking table and improve the accuracy of time waveform replication. Shen *et al.* (2018) proposed an inverse model controller to replicate the acceleration waveform on six-degree-freedom redundant electrohydraulic shaking tables. Yao *et al.* (2019) investigated the suppression of the electrohydraulic shaking table resonance using a compensator based on an adaptative Notch filter. Compensator filters have been used in other applications. Ahmadizadeh *et al.* (2008) and Chen and Ricles (2009) designed a compensator filter based on an equivalent discrete transfer function to remove, in real-time, the delay and the dynamics of the test rig. Cornelis *et al.* (2014) investigated two updates approaches to increase the time waveform accuracy in test rigs. One approach updates the excitation signal, while the second approach updates the compensator filter model.

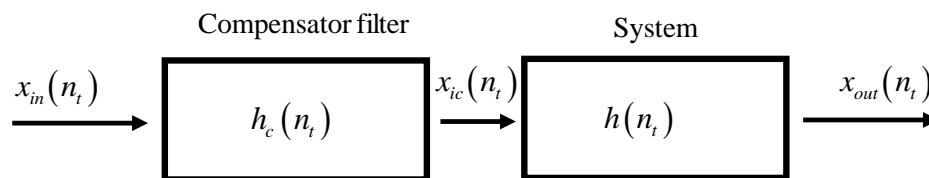
Recently, Iwanaga *et al.* (2019) investigated the leakage noise in water pipeline waveform replication in two electrodynamic shakers at the same time. They proposed a compensator filter design which removes the dynamics of the systems and the latency between the two shakers outputs. Yi *et al.* (2019) proposed a hybrid compensator filter based on a Finite-Impulse-Response model to compensate the ill-conditioned dynamic hysteresis on an electrodynamic shaker operating at a frequency below 5 Hz.

In this chapter, the design of a robust compensator filter to remove the dynamic of the system is described. A laboratory-based system, comprising a sound card, a power amplifier and an electromagnetic shaker, is used to emulate the sleeper vertical vibrations induced due the passage of a high-speed train. An experiment to emulate sleeper vertical vibration is performed for three cases: for a train passing at a speed of 200 km/s and at a speed of 100 km/h, using the compensator filter, and a train passing with a speed of 200 km/h without use the compensator filter. The time waveforms replicated are evaluated in the time and frequency domains.

4.2 TIME WAVEFORM REPLICATION: COMPENSATOR FILTER

To achieve the desirable waveform of the system response, the compensator filter is designed to remove totally or part of the system dynamics. It is desirable that the measured system response is equal to the desired waveform, i.e. $x_{out}(n_t) = x_{in}(n_t)$. An example of the proposed compensator filter scheme is shown in Fig. 20.

Figure 20. Scheme of the proposed compensator filter.



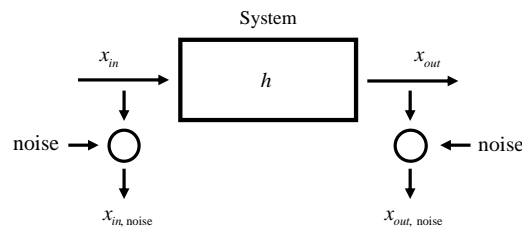
Source: author.

The waveform replication can be achieved by passing the desired waveform signal through the compensator filter and then the compensated input signal excites the system, resulting in the replication of the desired waveform. The process of the waveform replication is divided into three steps: *identification of the system dynamics, design of the compensator filter, design of the replicated waveform.*

4.2.1 The identification of the system dynamics

The dynamic identification of a linear time-invariant system is simply identifying the relationship between the system input and the output. An example of a single input and single output system is shown in Fig. 21.

Figure 21. Example of a linear diagram of a single input and a single output signal.



Source: author.

The system in Fig. 21 is represented as a black box. The system can be a single or a group of devices, i.e., the system is unknown. Note that the system input and output measurement may be noise-contaminated. Moreover, it is important to note that the system which is been identified is not the actual physical system but one that includes the individual frequency responses of sensors and filters, the effects of quantization noise, measurement of external noise and the experiment (SHIN; HAMMOND, 2008).

The system dynamics, if the measurement noise is ignored and both input and output signals are deterministic, in the discrete frequency domain is given by

$$H(g) = \frac{X_{out}(g)}{X_{in}(g)} \quad (82)$$

where

$$X_{in}(g) = \sum_{n_t=1}^N x_{in}(n_t) e^{-j \frac{2\pi n_t g}{N}} \quad (83)$$

and

$$X_{out}(g) = \sum_{n_t=1}^N x_{out}(n_t) e^{-j \frac{2\pi n_t g}{N}} \quad (84)$$

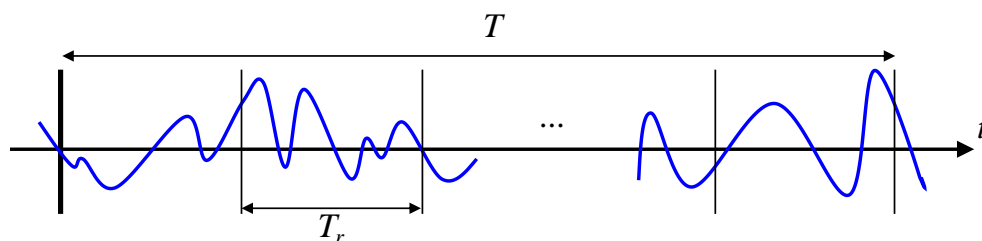
are the discrete Fourier transforms of the input and output signals, respectively.

However, the system input and output signals may be non-deterministic signals and noise-contaminated. In order to identify the system dynamics, the measured signals must be treated statistically. One way of doing this is to use a non-parametric estimator, such as Welch's periodogram estimator.

4.2.1.1 Direct method: Welch's periodogram estimator

There are different statistical estimation methods for random signals based on a single realization to estimate the power spectral density function (*PSD*). The most widely used is the non-parametric Welch's periodogram estimator. To reduce the random error, this method estimates the power spectral density by segmenting the signal in slices and then calculates their average. An example of the procedure is shown in Fig. 22.

Figure 22. Example of the segment averaging method procedure without overlapping.



Source: author.

The data of the time-history shown in Fig. 22, in which the time length is $T = \frac{N}{F_s}$, where the frequency sample is F_s and N is the number of points, is segmented into q separate time slices of N_r points, each of time length $T_r = \frac{N_r}{F_s}$. By definition, the periodogram for each segment is given by (SHIN; HAMMOND, 2008)

$$\hat{S}_{x_{in}, i}(g) = \frac{1}{N_r} \sum_{n_t=1}^{N_r} R_{x_{in}, i}(\rho) e^{-j \frac{2\pi g n_t}{N_r}} \quad \text{for } i = 1, 2, \dots, q \quad (85)$$

computed for a finite number of frequency points where $f_g = \frac{(g-1)F_s}{N_r}$ for $g = 1, 2, \dots, N_r$ and

$$R_{x_{in}x_{in},i}(n_t) = \frac{1}{N_r} \sum_{\tau=1}^{N_r} x_{in,i}(n_t) x_{in,i}(n_t - \rho) \text{ for } n_t = 1, 2, \dots, N_r \quad (86)$$

is the autocorrelation and ρ is the sample lag. Substituting Eq. (86) into Eq. (85) and with some manipulation, the periodogram can be rewritten as

$$\hat{S}_{x_{in}x_{in},i}(g) = \frac{1}{N_r F_s} \left| \sum_{n_t=1}^{N_r} x_{in,i}(n_t) e^{-j \frac{2\pi g n_t}{N_r}} \right|^2 = \frac{1}{N_r F_s} |X_{in,i}(g)|^2 \text{ for } i = 1, 2, \dots, q. \quad (87)$$

Note that the periodogram can be simply estimated by calculating the discrete Fourier transform of each segment of $x(n_t)$, which can be easily computed using the *FFT* algorithm. This is the reason why this non-parametric method widely used to estimate the *PSD*.

By averaging the periodogram, Eq. (87), the variability is reduced, thus the power spectral density is expressed as

$$\tilde{S}_{x_{in}x_{in}}(g) = \frac{1}{q} \sum_{i=1}^q \hat{S}_{x_{in}x_{in},i}(g) = \frac{1}{N_r F_s q} \sum_{i=1}^q |X_{in,i}(g)|^2. \quad (88)$$

and the variance reduction can be estimated by (SHIN; HAMMOND, 2008)

$$\frac{\text{Var}(\tilde{S}_{x_{in}x_{in}}(g))}{S_{x_{in}x_{in}}^2(g)} \approx \frac{1}{q} \quad (89)$$

where $S_{xx}^2(g)$ is the PSD without noise contribution. Equation (89) can be expressed in terms of the data window bandwidth resolution $B_r = \frac{F_s}{N_r} = q \frac{F_s}{N}$ as

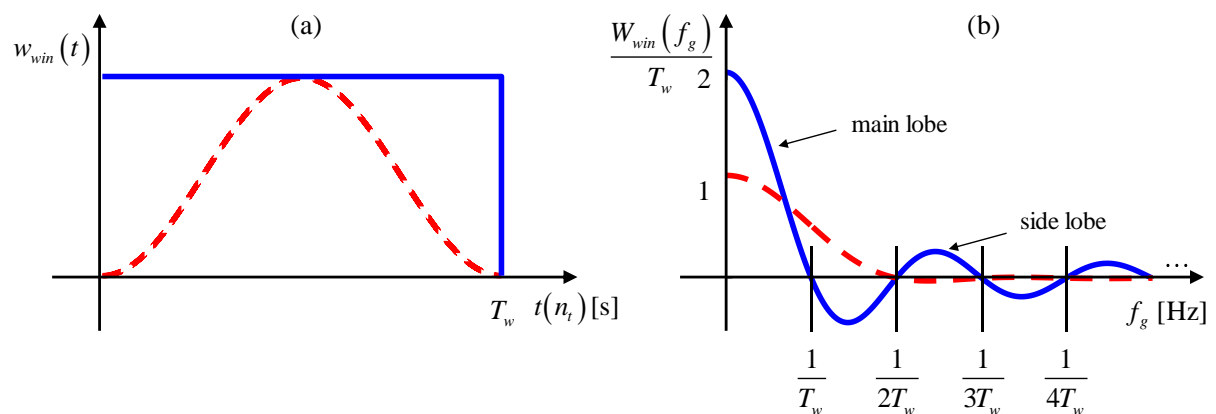
$$\frac{\text{Var}(\tilde{S}_{x_{in}x_{in}}(g))}{S_{x_{in}x_{in}}^2(g)} = \frac{F_s}{B_r N}. \quad (90)$$

Note from Eq. (89) that the variance can be reduced if the data is segmented in a large number of sequences. However, this implies that the resolution bandwidth becomes narrow since $N_r < N$ and the content of some frequencies may not be estimated. Therefore, the number of averages must be chosen carefully.

4.2.1.2 Direct method: The modified Welch's periodogram (overlapped averaging) estimator

In the estimation of the *PSD* using the Welch's periodogram, data segmentation is achieved by multiplying the data of the time-history by a rectangular window with N_r points (window time length of T_r). This windowed waveform introduces leakage which may compromise the estimation of the content in some frequencies. To minimize the bias error due to data truncation, different types of window waveforms have been proposed. Figure 23 shows an example of the rectangular and the Hanning windows in time and frequency domain.

Figure 23. Example of rectangular (blue solid line) and Hanning (red dashed line) window effect in: (a) time; and (b) frequency domains.



Source: author.

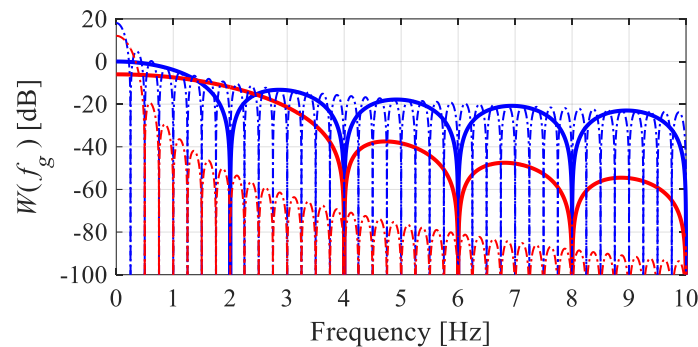
Figure 23(a) shows a comparison between a rectangular and hanning window. It can be seen that different from the rectangular window, the Hanning window smoothly reduces the amplitude of the segment data in its edge and introduces periodicity between segments. However, this reduction in amplitude implies that the energy of the segment is also reduced which need to be compensated when the periodogram is estimated.

Figure 23(b) shows that the windowing effect introduces distortions to the Fourier transform. The main lobe broadens the data frequency while the side lobes “leaks” and distort the adjacent frequencies. Also in Fig. 23(b), note that the Hanning window main lobe is broader than the rectangular window, which the first zero occurs at $1/T_w$ and $1/2T_w$ for rectangular and hanning window, respectively. However, the amplitude of their side lobes is lower than the rectangular window. Thus, if two or more frequencies are closely spaced, they will not be easily

observed mainly due to the main lobe distortion and then, the window time must be increased.

Figure 24 shows an example of the effect of increasing the window time.

Figure 24. Spectrum comparison of rectangular (blue line) and hanning (red line) windows for two window periods: T_w (thick solid line); and $2T_w$ (dashed line).



Source: author.

It is clear from Fig. 24 that the main lobe is narrowed if the window time is increased. Moreover, it is important to note that while the increase in the time window has no effect on the amplitude of the side lobes of the rectangular window, for the Hanning window it has an important effect on the reduction of leakage. Thus, to reduce the bias error, the window spectrum should have a very narrow main lobe, i.e. a long time window, so that $T_w \rightarrow \infty$. However, this implies that the data time-history is sliced into a small number of sequences (a small number of averaging) and results in a large random error. This shows that the number of points and the frequency sample must be carefully chosen to reduce both, bias and random errors.

Then, the modified Welch's overlapped averaging estimator can be expressed as (SHIN; HAMMOND, 2008)

$$\hat{S}_{x_{in}x_{in},i}(g) = \frac{1}{qU_i N_r F_s} \left| \sum_{n_t=1}^{N_r} w_{win,i}(n_t) x_{in,i}(n_t) e^{-j\frac{2\pi g n_t}{N_r}} \right|^2 = \frac{|W_{win,i}(g) X_{in,i}(g)|^2}{qU_i N_r F_s} \text{ for } i=1, 2, \dots, q \quad (91)$$

where $w_{win,i}(n_t)$ and $W_{win,i}(g)$ are the i -th window in discrete time and discrete frequency, respectively, and

$$U_i = \frac{1}{N_r} \sum_{n_t=1}^{N_r} |w_{win,i}(n_t)|^2 \quad (92)$$

is the window normalized constant. The cross-spectral density can be estimated by the same modified periodogram of Welch overlapped averaging and it is expressed as

$$\tilde{S}_{x_{in}x_{out}}(g) = \frac{1}{q} \sum_{i=1}^q \hat{S}_{x_{in}x_{out},i}(g) = \frac{1}{qN_r F_s} \sum_{i=1}^q \frac{W_{win,i}(g) X_{in,i}^*(g) X_{out,i}(g)}{U_i}. \quad (93)$$

4.2.1.3 The estimator H : the system identification for non-deterministic input and output signal

There are three estimators H where each of them is related to where the measured noise is located. Considering the modified Welch's overlapped averaging estimator, described in previous sections, if the measured noise is only in the output signal, the estimator H is defined as

$$H_1(g) = \frac{\tilde{S}_{x_{in}x_{out}}(g)}{\tilde{S}_{x_{in}x_{in}}(g)}, \quad (94)$$

which is the ratio between cross and the input power spectral density. For the case which the measured noise is only in the input signal, the estimator H is defined as

$$H_2(g) = \frac{\tilde{S}_{x_{out}x_{out}}(g)}{\tilde{S}_{x_{out}x_{in}}(g)}, \quad (95)$$

which is the ratio between the output power spectral density and the cross power spectral density. For the case which the noise is measured in both input and output signals, the estimator is defined as

$$H_T(g) = \frac{\tilde{S}_{x_{out}x_{out}}(g) - \tilde{S}_{x_{in}x_{in}}(g) + \sqrt{[\tilde{S}_{x_{in}x_{in}}(g) - \tilde{S}_{x_{out}x_{out}}(g)]^2 + 4|\tilde{S}_{x_{in}x_{out}}(g)|^2}}{2\tilde{S}_{x_{out}x_{in}}(g)}. \quad (96)$$

Thus, calculating the discrete inverse Fourier transform, the impulse response function is expressed as

$$h(n_t) = \frac{1}{N_r} \sum_{g=1}^{N_r} H(g) e^{j \frac{2\pi g n_t}{N_r}} \quad \text{for } n_t = 1, 2, \dots, N_r. \quad (97)$$

4.2.1.4 Coherence: the degree of correlation between signals

In the signal processing procedure to identify the system dynamics, it is important to verify how the output signal is correlated with the input signal. The coherence estimator uses the modified Welch's overlapped averaging estimator and it measures the degree of linearity between the input and output signals at each discrete frequency k . In other words, it measures how good the system was identified. Thus, the coherence function is defined as

$$\gamma_{x_{in}x_{out}}^2(g) = \frac{|\tilde{S}_{x_{in}x_{out}}(g)|^2}{\tilde{S}_{x_{in}x_{in}}(g)\tilde{S}_{x_{out}x_{out}}(g)} \quad (98)$$

where $0 \leq \gamma_{x_{in}x_{out}}^2(g) \leq 1$, which $\gamma_{x_{in}x_{out}}^2(g) = 1$ indicates that the $x_{in}(n_t)$ is totally correlated with $x_{out}(n_t)$.

4.2.1.5 The identification of the system dynamics: example

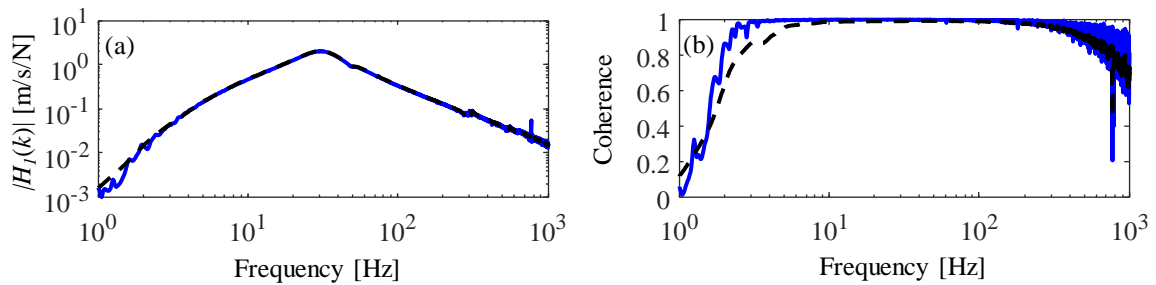
An example of the identification of the system dynamics is presented here using the *Matlab tfestimate function*, which is a function based on the non-parametric modified Welch's periodogram estimator.

The system consists of an analogue power amplifier connected to an electrodynamic shaker. A random signal, generated in a computer, with the duration time of 60 s and frequency sample of 1000 Hz was used to excite the system and the shaker velocity output was measured using a vibrometer and recorded by a LMS Scadas XS. Using a Hanning window, 50% of overlap and two different number of averages – 5 and 40 – the estimated *FRFs* are shown in Fig. 25 and their corresponding *IRF* are shown in Fig. 26.

From Fig. 25 it can be seen that when there are three averages the *FRF* provides good estimation. However, note in Fig. 25(b) that for frequencies below 10 Hz, due to the increase in the bias error, there is a deterioration in the coherence as the number of averages is increased. On the other hand, the random error is reduced, where for frequencies higher than 10 Hz the coherence is closer to 1 and smoother. This variance reduction is almost not visible in the magnitude of the *FRF* in Fig. 25(a). This is better viewed in the *IRF* in Fig. 26, from which it

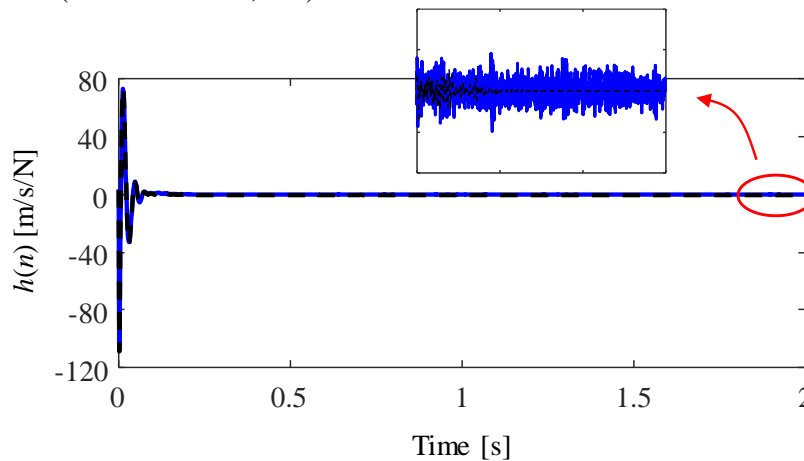
is clear that increasing the number of averaging has a considerable improvement to reduce the variance of the estimator.

Figure 25. Example of the system dynamic identification considering 50% of overlap and $q = 40$ averages (black dashed line, - -) and $q = 5$ averages (blue solid line, —): a) estimator H ; and b) coherence.



Source: author.

Figure 26. Example of the IRF , $h(n)$, for two number of averages: $q = 40$ (black dashed line, - -); and $q = 5$ (blue solid line, —).



Source: author.

4.2.2 Design of the compensator filter

A robust filter, which removes the effects of the system, is one that has exactly the inverse dynamics of the system whose the filter will be applied, so that the product between the compensator filter and the system IRF is $h_c(n_t) * h(n_t) = \delta(n_t)$, where $\delta(n_t)$ is the Dirac delta function. However, $h_c(n_t) \neq h^{-1}(n_t)$ and the compensator filter is better designed in the frequency domain which the filter transfer function is simply the inverse of the system FRF , $\bar{H}(g) = H^{-1}(g)$.

Bias and random errors cannot be avoided in the system *FRF* estimation using the non-parametric estimator; however, they must be minimized to design the filter transfer function. This minimization is obtained by performing a pre-processing to guarantee the system stability when the compensator filter transfer function is designed and a post-processing to maximize the filter performance. The compensator filter design has 3 main steps: *the pre-processing*; *the filter design* (the frequency response function design); and *the post-processing*. Each of these steps are discussed in the following subsections.

4.2.2.1 Preprocessing

Errors may be carried from the non-parametric estimation and pre-processing of the *IRF*, $h(n)$, is performed to minimize them before the compensator filter transfer function is designed. For applications where low frequency is important (e.g. 1 Hz), bias and random errors become more sensitive. To minimize both errors, a data measurement with long duration time and large sample size are required. On the other hand, this implies a high computational cost.

To remove some non-causality introduced by the inverse Fourier transform, $h(n_t)$ is truncated at the first N_t samples, where $N_t = \frac{N_r}{2}$ and is integer. Despite this being an arbitrary number, the sample size of the truncated *IRF* has a profound influence on the filter efficacy, even more so for low frequency compensation (< 10 Hz), which requires a large sample size. This is further discussed later. Moreover, the truncated *IRF* is circle-shifted in $\frac{N_t}{2}$ samples, this is the same as introducing a time delay of $t_d = \frac{N_t}{2F_s}$ and, then applying a Hanning window to minimize the variance, forcing the data extremities to zero. Thus, the pre-processed *IRF* is

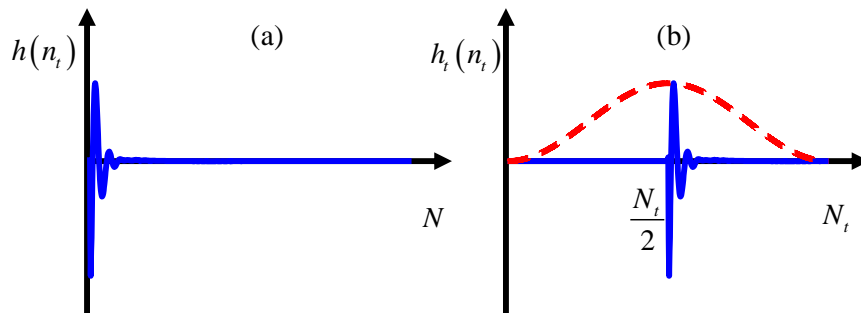
$$\hat{h}(n_t) = w_{win,t}(n_t)h_t(n_t), \text{ for } n_t = 1, 2, \dots, N_t \quad (99)$$

where $w_t(n_t)$ is the Hanning window and

$$\begin{cases} h_t(n_t) = h\left(n_t + \frac{N_t}{2}\right), \text{ for } n_t = 1, 2, \dots, \frac{N_t}{2} \\ h_t(n_t) = h\left(n_t - \frac{N_t}{2}\right), \text{ for } n_t = \frac{N_t}{2} + 1, \frac{N_t}{2} + 2, \dots, N_t \end{cases} \quad (100)$$

is the truncated circle-shifted *IRF*. An example of this pre-processing is shown in Fig. 27, where it can be noted that the IRF is circle-shifted to guarantee that the window will not truncate the section which contains the system dynamics.

Figure 27. Example of the pre-processing of the system impulse response function: a) before pre-processing, $h(n_t)$; and b) after the pre-processing, $\hat{h}(n_t)$. The blue solid line (—) is the impulse response function; and the red dashed line (---) is the applied window.



Source: author.

4.2.2.2 The compensator filter transfer function design

The compensator filter should compensate for the system dynamics and it is better to design it in the frequency domain. So, first, the pre-processed *IRF*, given by Eq. (99), is transformed into the frequency domain. Using the Discrete Fourier Transform, the pre-processed *FRF* is given by

$$\hat{H}(g) = \sum_{n_t=1}^{N_t} \hat{h}(n_t) e^{-j \frac{2\pi g n_t}{N_t}} \quad \text{for } g = 1, 2, \dots, N_t. \quad (101)$$

Then, the compensator filter transfer function is simply given by

$$\bar{H}(g) = \frac{1}{\hat{H}(g)} \quad (102)$$

and by calculating its inverse Fourier transform, the compensator filter in discrete time domain is

$$\bar{h}(n_t) = \sum_{g=1}^{N_t} \bar{H}(g) e^{j \frac{2\pi g n_t}{N_t}} \quad \text{for } n_t = 1, 2, \dots, N_t. \quad (103)$$

4.2.2.3 Post-processing

The post-processing step, which is the third step in the compensator filter design, is performed to remove minor errors introduced due to previous steps. This step is divided into two procedures: (1) remove the non-causalities due to the inverse Fourier transform; and (2) remove the lag due to the data circle-shift. For applications in which the number of the samples of the truncated data, N_t , and the signal frequency sample, F_s , are small, the introduced time delay, $t_d = N_t/2F_s$, is small and the post-processing step may be disregarded, then the compensator filter is simply given by

$$h_c(n_t) = \bar{h}(n_t). \quad (104)$$

However, if a long time delay is introduced, the compensator filter may not perform well, compromising the waveform replication which may occur at a time later than the predefined duration time of the signal.

The domain transform, from frequency to time, using the inverse Fourier transform algorithm (*iFFT*) in the compensator filter transfer function design, may introduce non-causality. This is removed by applying a Hanning window to smoothly force the data sample extremities to zero. Thus, the adjusted compensator filter is given by.

$$\bar{h}_c(n_t) = w_{win}(n_t) \bar{h}(n_t) \quad \text{for } n_t = 1, 2, \dots, N_t, \quad (105)$$

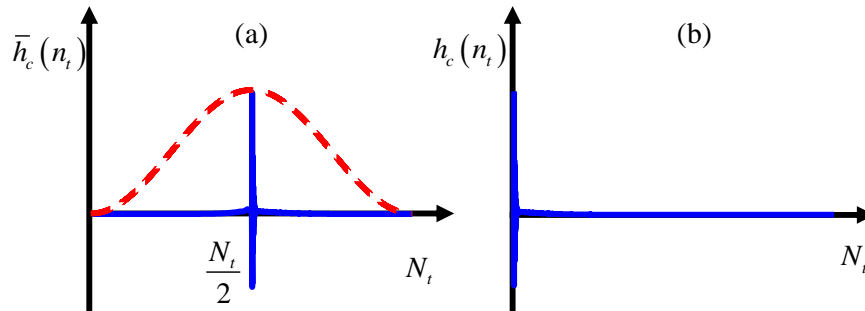
where $w_h(n_t)$ is the Hanning window. An example of this procedure is shown in Fig. 28a.

The lag due to the circle-shifted data applied in the pre-processing step is removed by circle-shifting by $N_t/2$ samples the adjusted compensator filter, $\bar{h}_c(n_t)$, which gives

$$\begin{cases} h_c(n_t) = \bar{h}_c\left(n_t + \frac{N_t}{2}\right), & \text{for } n_t = 1, 2, \dots, \frac{N_t}{2} \\ h_c(n_t) = \bar{h}_c\left(n_t - \frac{N_t}{2}\right), & \text{for } n_t = \frac{N_t}{2} + 1, \frac{N_t}{2} + 2, \dots, N_t \end{cases} \quad (106)$$

and an example of this procedure is shown in Fig. 28b.

Figure 28. Example of the postprocessing procedure: a) *hanning* window application; and b) the remove of the introduced lag.



Source: author.

Moreover, it may be desirable that a time delay is added to the time wave replication. This implies that the system will respond after a pre-set time delay, t_d . This is introduced to the compensator filter by circle-shifting its sample by $N_d = t_d F_s$, so that the delayed compensator filter is given by

$$\begin{cases} h_{cd}(n_t) = h_c(n_t + N_t - N_d), & \text{for } n_t = 1, 2, \dots, N_d \\ h_{cd}(n_t) = h_c(n_t - N_d), & \text{for } n_t = N_d + 1, N_d + 2, \dots, N_t. \end{cases} \quad (107)$$

4.2.3 Design of the compensated input signal

The compensated input signal is simply a signal passed through the compensator filter. The schematic of the input signal design is shown in Fig. 29.

Figure 29. Schematic of the input signal with the system compensation.



Source: author.

The procedure consists of a signal, $x_m(n_t)$, with a desired time waveform, convolved with the respective system compensator filter, so the compensated input signal is

$$x_{ic}(n_t) = h_c(n_t) * x_m(n_t) \quad (108)$$

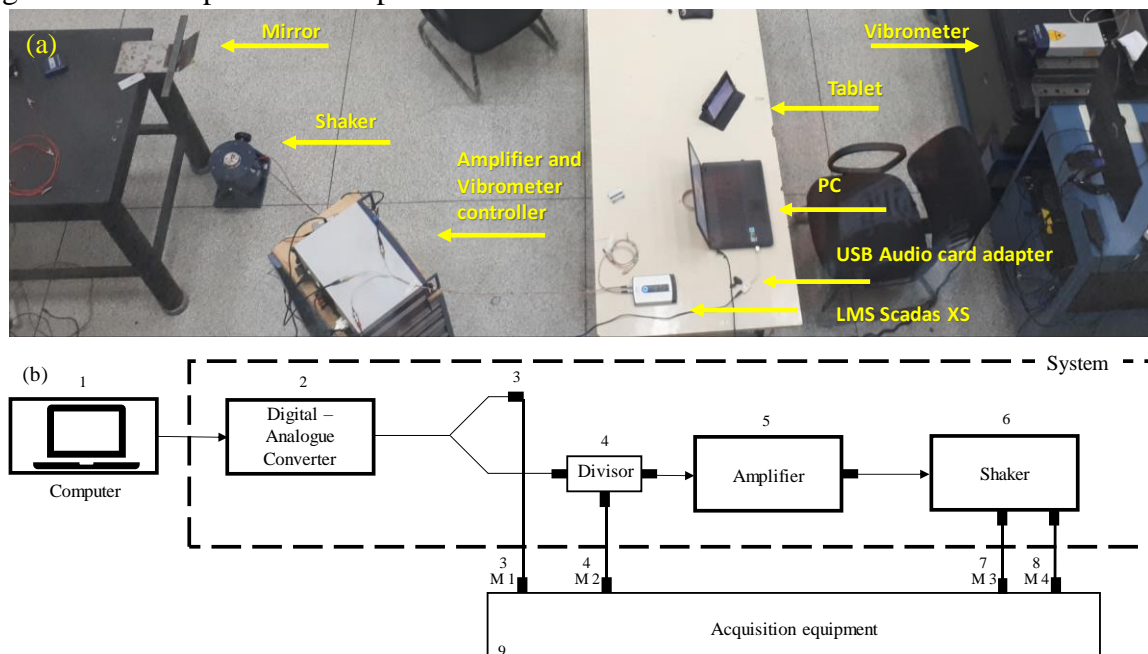
The advantage of performing this procedure by convolution is that the compensated input signal will not be restricted by the number of samples of the compensator filter. Its limitation is related to the sample frequency, F_s , which must be the same for both compensator filter and the desired input signal.

4.3 THE LABORATORY-BASED SYSTEM FOR THE SLEEPER TIME WAVEFORM REPLICATION

4.3.1 The laboratory-based system setup

The experiment setup is shown in Fig. 30(a) and the schematic of the experiment setup is shown in Fig. 30(b). It consisted of a computer (1) and a USB sound card adaptor (2) as the signal generator, a Crown Xli 2500 (5), an analogue power amplifier and an electrodynamic shaker (6). A vibrometer (7) and a Brüel & Kjaer triaxial accelerometer (8) were used to measure the vertical shaker velocity and acceleration, respectively, and the LMS Scadas XS (9) with 12 input channels, was used to data acquisition. A mirror with an angle of 45° was used to reflect the laser point direction from horizontal to the vertical direction.

Figure 30. The experiment setup.



Source: author.

4.3.2 The signal generator

The signal generator is a device which generates a signal in the time domain with a choice of several waveforms and then converts it from digital to analogue so that the signal can be applied. In this experimental setup, the signal is generated on the computer as sound data using the *Matlab* and using a generic USB sound card adapter, the sound data is converted from digital to analogue with 24 bits per sample and applied to the system. A limitation to using the computer sound as a signal generator is the peak-to-peak signal amplitude output must be smaller than or equal to 2V.

4.3.3 The compensator filter

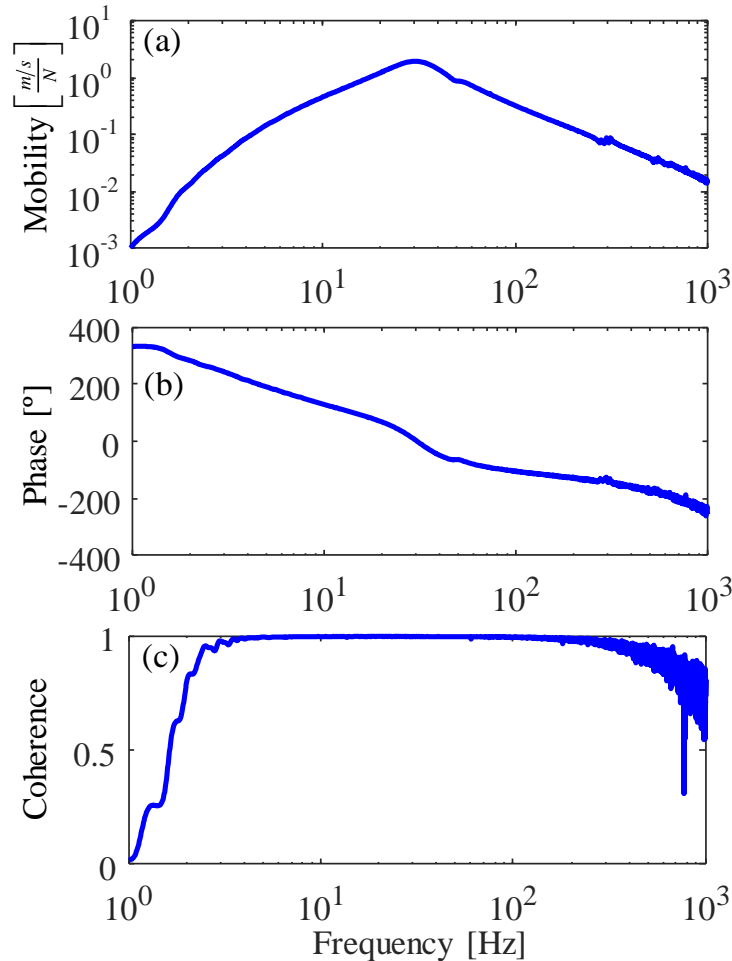
In this section, the compensator filter based on the experiment setup described in Fig. 30 is designed. The procedure consists of estimate the system *FRF*, design the compensator filter and numerically test the compensator filter.

4.3.3.1 The identification of the system dynamics

Identification of the system dynamics is carried out to determine the relationship between the system input and output. The experiment to identify the dynamics of the system consist of applying an input signal which excites a large range of frequencies.

The system shown in Fig. 30 was excited with a random signal with a time duration of $T = 60$ s and a sample frequency of $F_s = 5120$ Hz. The shaker velocity was measured using the laser vibrometer and acquired by the LMS Scadas XS. Considering the input data (the data generated on the computer) and the measured shaker velocity, the estimation of the system dynamics was performed in *Matlab* using the *tffestimate* with 20 averages and 50% overlap. The system mobility, phase and coherence are shown in Fig. 31

Figure 31. The estimated system *FRF*: a) Mobility; b) phase; and c) coherence.

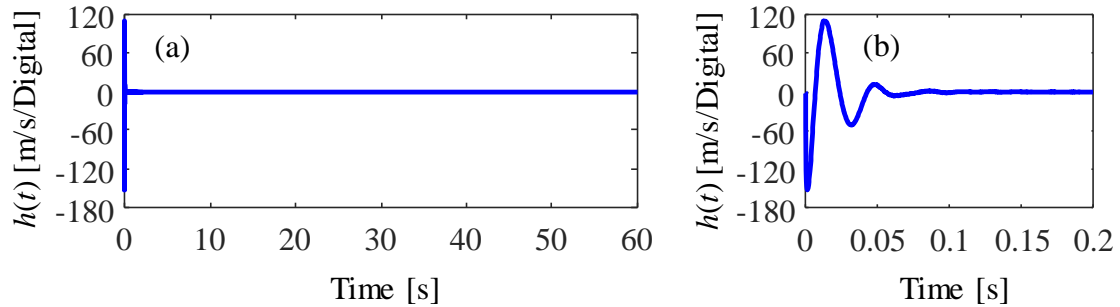


Source: author.

From Fig. 31(a) and (b) we can note that it is possible to use the computer with a sound card as a signal generator and the non-parametric Welch's estimator was able to identify the system dynamics. Moreover, in Fig. 31(c) it can be seen that the coherence function is $\gamma^2 > 0.9$ for frequencies higher than 3 Hz.

The inverse Fourier transform was calculated from the estimated *FRF* and plotted in Fig. 32. From Fig. 32(b) it can be seen its free decay oscillation goes to zero around 0.1s. Despite the system is heavy damped and the important system dynamic comprises of only this 0.1s, to increase the compensator filter performance a large number of samples is necessary.

Figure 32. The *IRF* mobility of the experiment setup #1 system: (a) the full time-history; (b) the zoom-in.

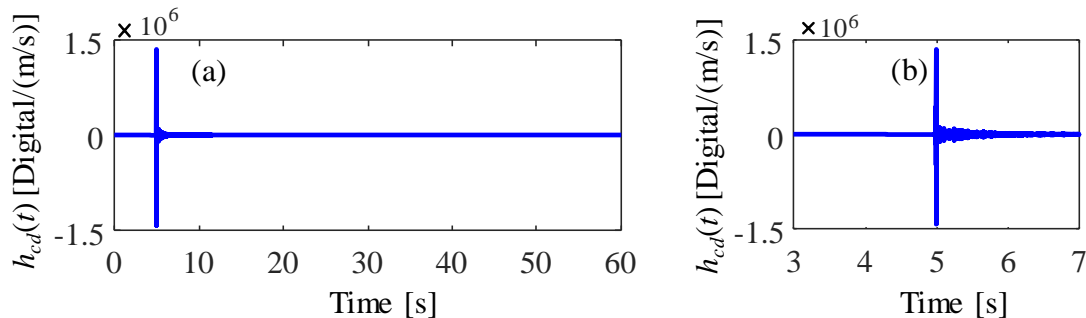


Source: author.

4.3.3.2 The design of the compensator filter

The compensator filter is designed for the system described in Fig. 30 and is shown in Fig. 33. Following the compensator filter design, described in Section 4.2.2, the data sample of the *IRF* obtained from the system mobility was truncated at 153600 samples (corresponding to 60s) and a delay of 5s was added during the postprocessing.

Figure 33. The compensator filter with 10s delay: (a) full time-history; and (b) a zoom-in.



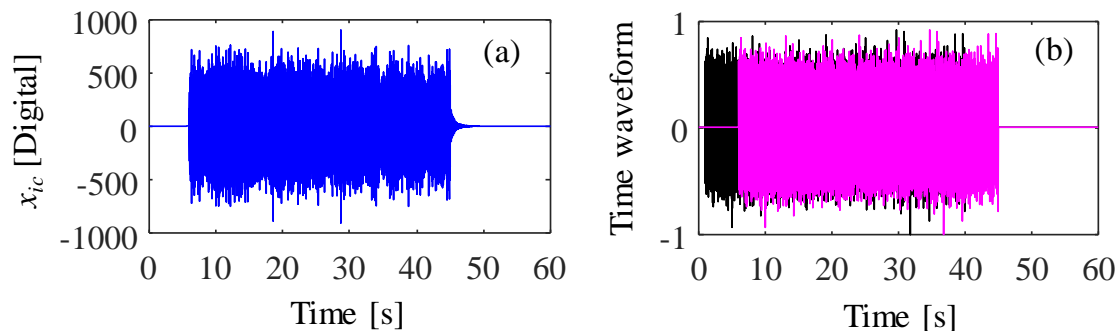
Source: author.

4.3.3.3 The time waveform replication: simulation

This simulation was performed to test numerically the compensator filter; evaluating the time waveform of the system response and to determine its frequency range of actuation. A signal comprising of the first 40 s of random vibration in a duration time of $T = 60$ s and a

sample frequency of $F_s = 5120\text{Hz}$ was convolved with the compensator filter to generate the input compensated signal x_{ic} , shown in Fig. 34(a). The system response was obtained by convolving the x_{ic} with the estimated IRF , $h(t)$. The system response is shown in Fig. 34(b) by comparing with the desirable waveform.

Figure 34. Test of the compensator filter: (a) input compensated signal; and (b) time-history comparison between desired (black solid line, —), and system response (magenta dotted line, - - -) time waveforms.



Source: author.

Figure 34(b) apparently shows that the compensator filter was able to remove the system dynamics and replicate the desired time waveform. Also, note that the system response is shifted in time due to the delay introduced in the compensator filter design. For this random signal waveform replication, a better analysis is performed by evaluating the magnitude ratio between the desirable and the system response spectrums.

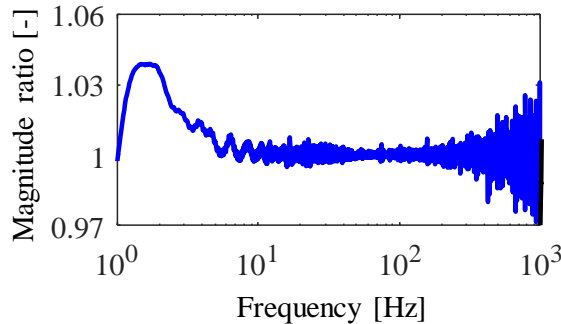
To evaluate how good the spectrum of the system response compared with the spectrum of the desirable waveform replication, the magnitude ratio between spectrums is calculated by

$$R = \frac{X_m(g)}{X_d(g)} \quad (109)$$

where $X_m(g)$ is the system measurement and $X_d(g)$ is the desired system time waveform in the discrete frequency domain.

For this particular case, the magnitude ratio is shown in Fig. 35 where the magnitude ratio is approximately 1 for frequencies higher than 3 Hz up to 100 Hz, which is the frequency range for this compensator filter.

Figure 35. The magnitude ratio between desirable and system response time waveforms.



Source: author.

4.3.4 The sleeper vertical vibration waveform replication

In this section, the sleeper vertical vibration is replicated in the laboratory-based system described in Fig. 30. First, the model to design the desirable waveform is presented and the train and the railway track parameters are introduced. Later, the experiment is performed to replicate the sleeper vertical vibration waveform.

4.3.4.1 The model of the sleeper vertical vibration

The model of the sleeper vibration consists of an infinite Euler-Bernoulli beam resting on a Winkler foundation. This model was described in Chapter 2 and it is presented here, again, for convenience. The sleeper vertical displacement is given by (CLEANTE *et al.*, 2019)

$$w_{\text{sleeper}}(x, t) = \frac{-\beta}{2k_{\text{trackbed}}} \sum_{i=1}^4 F_i e^{-\beta|St-x_i-d_i|} \left[\cos(\beta(St-x_i-d_i)) + \sin(\beta|St-x_i-d_i|) \right] \quad (110)$$

where $\beta = \sqrt[4]{\frac{k_{\text{support}}}{4EI}}$ has units of m^{-1} , $k_{\text{support}} = \left(\frac{L_{\text{sleeper}}}{k_{\text{pad}}} + \frac{1}{k_{\text{trackbed}}} \right)^{-1}$ is the support stiffness, which is the trackbed stiffness (the stiffness of the ballast in series with the ground) in series with the rail pad stiffness per unit of the sleeper length, t is time, F_i is the force due to the i -th wheel and d_i is distance between the 1st and the i -th wheel and x_i is the observation point.

4.3.4.2 The train and railway track parameters: the Inter-city 125 high-speed train passing-by Steventon site, United Kingdom (UK)

The time waveform of the sleeper vertical vibration is due to the passage of an Inter-city 125 high-speed train. This train consists of 2 power cars, one at the front and the other at the back of the train, and 8 passenger carriages between them. The railway track parameters are related to the Steventon site, a railway site from the train line which links Swindon to Didcot, in the UK. For the cases investigated in this section, only the vibration due to the passage of the passenger carriages is taken into consideration. The train and track parameters are given in Tab. 2 and Tab. 1.

Table 5 – Train parameters.

Train class	Name	Car length [m] – L_{car}	Bogie length [m] – L_{wheel}	Distance between bogie centre [m] – L_{bogie}	Wheel load [kN]*
Mk3	Inter-city 125	23.0	2.6	16.0	21.9

Source: (TRIEPAISCHAJONSAK, 2012); *(CLEANTE *et al.*, 2019).

Table 6 – Characteristics railway track at Steventon site.

Rail type [Nm ²]	Trackbed [N/m ²]*	Rail pad [N/m]	Sleeper spacing [m]
CEN 60E1 ($EI = 6.24 \times 10^6$)	$k_{\text{trackbed}} = 1.39 \times 10^7$	Pandrol 6650 ($k_p = 60 \times 10^6$)	0.65

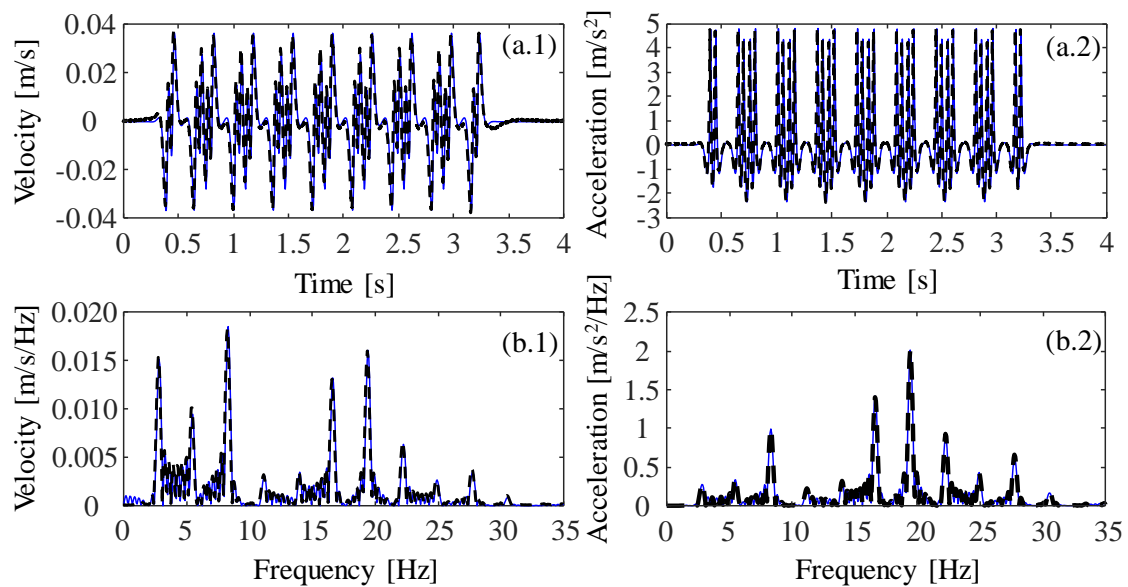
Source: (TRIEPAISCHAJONSAK, 2012); *(CLEANTE *et al.*, 2019).

4.3.4.3 The experiment: Inter-city 125 train passing at speed of 200 km/h with the compensator filter

The sleeper vertical vibration is emulated in the laboratory-based system for the Intercity 125 at a speed of 200 km/h passing at Steventon site. Using the train and the railway track parameters given in Tabs. 2 and 1, in Eq. (110), the waveform of the sleeper vertical displacement is generated for a duration time of 16 s and with a frequency sample of 5120 Hz. The sleeper vertical displacement is derived once and twice with respect to time to obtain the sleeper vertical velocity and acceleration, respectively. The sleeper vertical velocity generated on the computer is then convolved with the compensator filter to produce the compensated input signal and used to excite the system. The shaker velocity and acceleration are measured and are shown in Fig. 36, compared with their respective desired sleeper vertical vibration waveforms.

Also, the spectrum ratio between the measured shaker acceleration and the desirable sleeper vertical acceleration is calculated and shown in Fig. 37.

Figure 36. Waveforms comparisons of the vertical sleeper velocity and acceleration, due to the passage of 8 passenger carriages of the Inter-city 125 train at a speed of 200 km/h, between desirable (blue solid line, —) and measured on the shaker (black dashed line, - -): (a) time-history; and (b) spectral density.



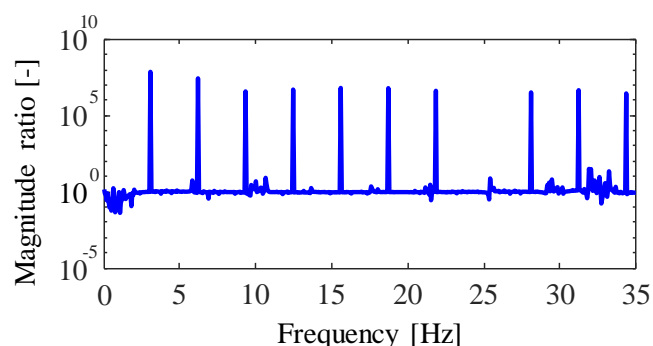
Source: author.

Note in Fig. 36(a.1) and (a.2) that the measured shaker velocity and acceleration were, manually, shifted in time so that their waveforms overlay with the desired waveforms. Hence, it can be seen that in both time and frequency domains, the measured shaker vibration has good agreement with the desired waveform. Using the compensator filter, the system was able to replicate the waveforms with the same amplitude and shape. However, note in Fig. 36(a.1) that there is a small difference at the beginning and at the end of the measured shaker velocity section corresponding to the passage of the train. This is, probably, due to the fact that the compensator filter cannot compensate the vibrations below 3 Hz. If compared with the acceleration, Fig. 36(a.2), this phenomenon is not observed. As the acceleration is simply the velocity multiplied by $j\omega$, vibrations at higher frequencies are amplified compared to the lower frequencies, making this compensator limitation not visible.

From the magnitude ratio, in Fig. 37, it is clear that the system is able to replicate the desirable waveform if the compensator filter is applied. The magnitude ratio is around 1 for the

frequencies higher than 3 Hz, which is the frequency range of the designed compensator filter. Moreover, if compared this with the shaker acceleration spectrum Fig. 36(b.2), we can observe that the spikes occur at frequencies which the desired spectrum is zero (or close to it), and a reasonable explanation for this, is that the shaker cannot vibrate with that amplitude, resulting in a large error.

Figure 37. Spectrum ratio between desirable and measured shaker acceleration due to the passage of 8 passenger carriages of the Inter-city 125 train at a speed of 200 km/h.



Source: author.

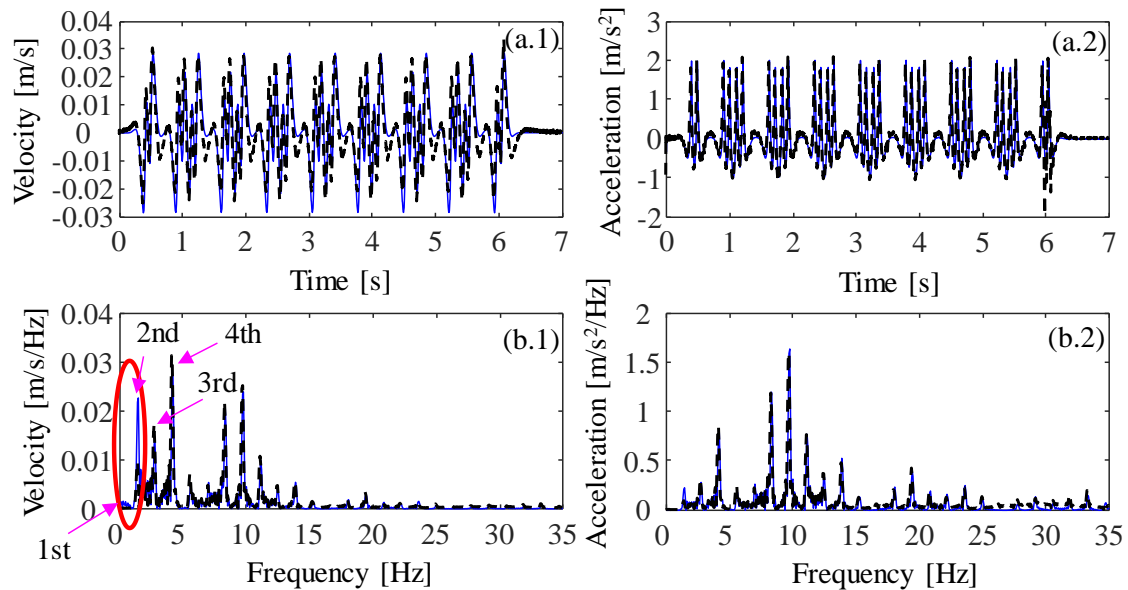
4.3.4.4 Inter-city 125 train passing at speed of 100 km/h

For this case, the compensator filter is evaluated for a passing train at a speed of 100 km/h. Despite this not being a typical speed for this train configuration, nor for the Steventon site, the frequency of the 7th trainload frequency, which occurs at 10 Hz, coincides with the natural frequency of the electromagnetic energy harvester which is investigated in Chapter 5. The measured shaker velocity and acceleration are shown in Fig. 38 compared with the respective desired time waveforms. Also, the spectrum ratio between the measured shaker acceleration and the desirable sleeper vertical acceleration is calculated and shown in Fig. 39.

Note from Fig. 38 that, despite the measured shaker response appears to be periodic and similar to the desired time waveforms, the amplitude and shape do not have good agreement. This can be seen in Fig. 38(a.1) and is particularly evident in Fig. 38(b.1) where the velocity spectra are compared. Note that there is a large difference, in the 1st and 2nd dominant peaks, between the measured and desired spectra. This is because the fundamental frequency of the vibration induced by this passing train speed is 1.2 Hz, which is lower than the compensator filter lower frequency of actuation (3 Hz). However, it can be observed from the acceleration measurements shown in Fig. 38(a.2) and (b.2), that the agreement between the measured and

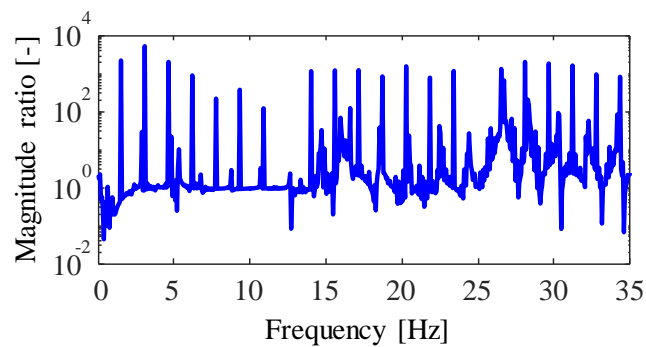
desired signals are relatively good. The two dominant peaks, that could not be compensated for, are less sensitive for acceleration than velocity.

Figure 38. Waveforms comparisons of the vertical sleeper velocity and acceleration, due to the passage of 8 passenger carriages of the Inter-city 125 train at a speed of 100 km/h, between desirable (blue solid line, —) and measured on the shaker (black dashed line, - -): (a) time-history; and (b) spectrum.



Source: author.

Figure 39. Magnitude ratio between desirable and measured acceleration spectrums due to the passage of 8 Inter-city 125 passenger carriages at a speed of 100 km/h.



Source: author.

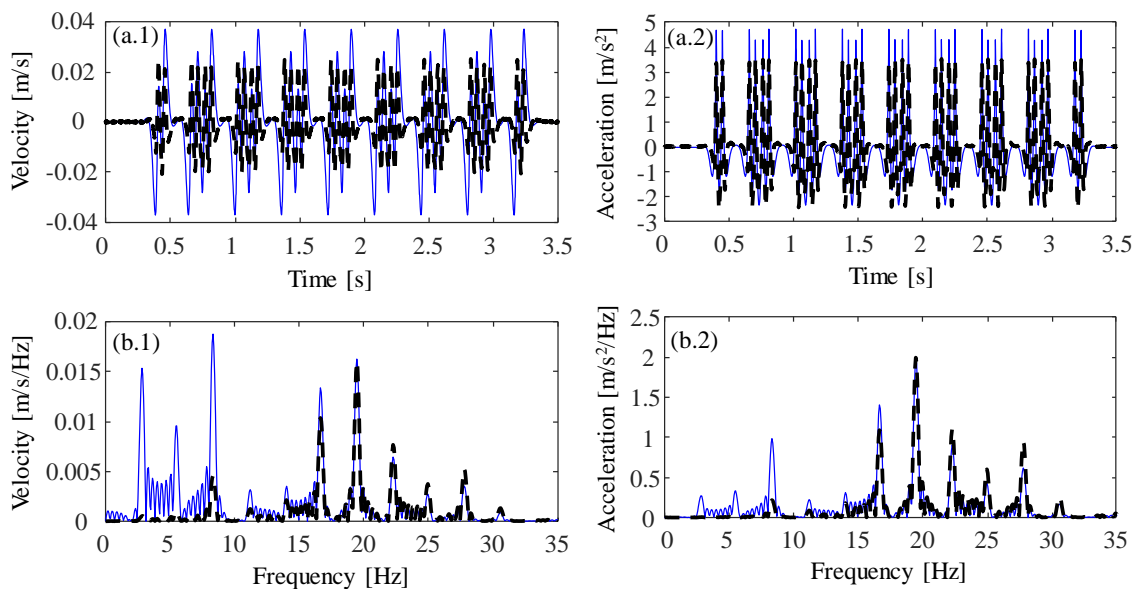
When the magnitude ratio is examined, it can be seen that the time waveform replicated is relatively good for this train speed case. Note that from 3 to 15 Hz, which accommodates the largest dominant peaks, the magnitude ratio is around 1. For frequencies greater than 15 Hz,

which the acceleration spectrum amplitude is close to zero, the magnitude ratio is compromised showing that the shaker cannot emulate these vibration levels.

4.3.4.5 Inter-city 125 train passing at speed of 200 km/h without the compensator filter

To emphasise the detrimental effect that the system dynamics has on the time waveform of a signal, first an experiment without a signal compensation is performed. The system is excited with a time waveform of the sleeper vertical velocity due to the passage of an Inter-city 125 at a speed of 200 km/h without signal compensation. The measured shaker velocity and acceleration are shown in Fig. 40 compared with its respective desirable time waveforms. Also, the spectrum ratio between the measured shaker acceleration and the desired sleeper vertical acceleration is calculated and shown in Fig. 41.

Figure 40. Comparison between desirable, blue solid line, and measured, black dashed line, time waves of the sleeper vertical velocity (.1) and acceleration (.2) due to the passage of 8 Inter-city 125 passenger carriages at speed of 200 km/h without the compensator filter: (a) time-history; and (b) spectrum.

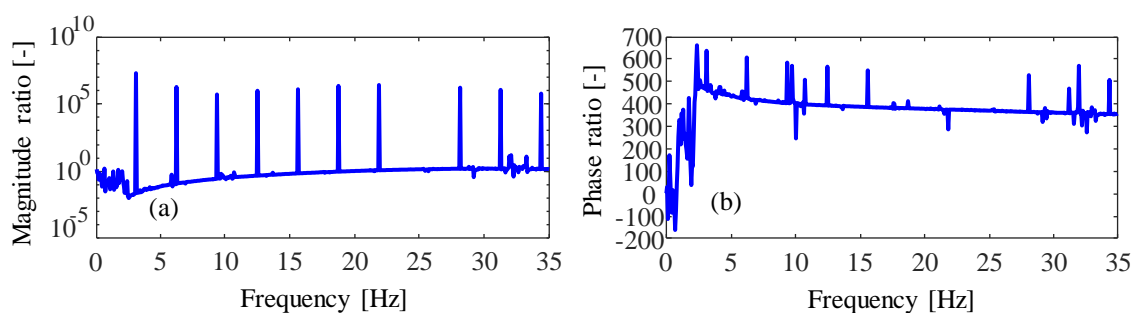


Source: author.

Figure 40(a.1) and (a.2) shows that the measured shaker velocity and acceleration are different in amplitude and shape when compared with their respective desired time waveforms. These differences are also seen in the frequency domain, as shown in Fig. 40(b.1) and (b.2).

Moreover, strong degradation of the measured spectra at frequencies below 15 Hz is evident. This may occur as both the USB sound card adapter and power amplifier are first-order systems which act similar to a high-pass filter. For this particular case, the magnitude ratio and the phase ratio between the measured acceleration and the desirable time wave without the compensator filter are shown in Fig. 41.

Figure 41. Spectrum ratio between desirable and measured acceleration time waves due to the passage of 8 Inter-city 125 passenger carriages at speed of 100 km/h without the compensator filter: (a) magnitude; and (b) phase.



Source: author.

It can be seen in Fig. 41(a) that the magnitude ratio between signals is not flat with a value of 1, i.e., the measured shaker does not represent the desirable time waveform at almost all frequencies. Also, the strong degradation at frequencies below 15 Hz is clear. This shows that to replicate a time waveform in a laboratory-based system it is necessary to use a compensator filter to remove the dynamics of the system. Moreover, if this is compared with the shaker acceleration spectrum shown in Fig. 40(b.2), it can be seen that the spikes occur at frequencies where the desirable spectrum is zero (or close to it). A reasonable explanation for this, is the fact that the shaker cannot vibrate with that amplitude, resulting in large error.

4.4 CONCLUSIONS

This chapter has investigated the replication of sleeper vertical vibration, induced due to the passage of a train, in a laboratory-based system. To be able to replicate the desired time waveform, a methodology to design the compensator filter which removes the dynamics of the system in which the filter is applied was proposed. The compensator filter was experimentally evaluated in laboratory. The results showed that using the compensator filter, the system which

has an electrodynamic shaker was able to emulate the sleeper vertical vibration in a laboratory-based system. In addition, it has been shown that the lower frequency of actuation of the compensator filter is 3 Hz, which allowed the sleeper vibration waveform induced by slowest trains capable to be replicated. Following, this laboratory-based system will be used to determine the harvested energy from vibration induced by a passing train and validate the energy harvesting model.

5 HARVESTING ENERGY FROM THE VIBRATION INDUCED DUE TO A PASS-BY TRAIN

5.1 INTRODUCTION

Harvesting energy from railway vibrations is a relatively new topic and a few research groups are investigating this subject. Most of them have focused their investigations into energy harvesting devices which convert the track vertical vibration into rotatory movement, using gears and rack-pinions, and then, into electrical energy (LIN; WANG; ZUO, 2018; PAN *et al.*, 2019; POURGHODRAT *et al.*, 2014; ZHANG *et al.*, 2016). Li *et al.* (2014b) and Gao *et al.* (2016) used a piezoelectric transducer and Gao *et al.*, (2017) and Gao *et al.*, (2018) used an electromagnetic transducer to scavenge energy from the track vibration. However, these published papers have focused their investigation into harvesting energy from the track deflection and a minor attention have been given to investigate at which frequency the energy harvester should be tuned to maximize its performance. Recently, Gatti *et al.* (2016) and Brennan and Gatti (2017a) investigated the linear single-degree-of-freedom mass-spring-damper oscillator to determine the energy that could be harvested from a passing train and the optimum parameters that maximize the performance of the device. It was determined that the natural frequency of the device should be equal to the frequency corresponding to the maximum acceleration amplitude and Cleante *et al.* (2019) showed that due to spacing between wheels and the spacing between bogies, unless the trackbed stiffness is very soft, the target frequency is the 7th trainload frequency. This was discussed in Chapter 2.

In Chapter 3, it was shown that the electromagnetic transducer is better suited to harvest energy from low frequency vibrations than a piezoelectric transducer. Moreover, it was shown that to maximize the performance of the device, the mechanical damping and the internal coil resistance should be as lower as possible.

In this Chapter, the use of an electromagnetic transducer to scavenge the energy from the sleeper vertical vibration induced by a passing train is investigated. Numerical and analytical investigations into the performance of a linear single-degree-of-freedom device are carried out and the amount of energy, together with the optimum load resistance, are determined. This analyse is similar to the one performed in (GATTI *et al.*, 2016), but includes the effects of the transducer. Following the analysis, the parameters of a Geophone SM-24

transducer are used in a numerical investigation to determine the optimum load resistance. This is validated with an experimental test.

5.2 THE SLEEPER VERTICAL VIBRATION AS THE SOURCE OF THE ENERGY HARVESTING DEVICE BASE EXCITATION

The vibration of a sleeper due to a passing train was discussed in Chapter 2 and in (CLEANTE *et al.*, 2019). This vibration is categorized as quasi-static excitation (LOMBAERT; DEGRANDE, 2009; THOMPSON, 2008). At the sleeper, Auersch (2005) and Sheng *et al.* (1999) showed that the quasi-static excitation is dominant and the largest levels of vibration occur at low frequencies. Using the sleeper deflection equation, Eq. (2), repeated here for convenience, given by

$$w_{\text{sleeper}}(x, t) = \frac{-\beta}{2k_{\text{trackbed}}} \sum_{i=1}^4 F_i e^{-\beta|St-x_i-d_i|} \left[\cos(\beta(St-x_i-d_i)) + \sin(\beta|St-x_i-d_i|) \right], \quad (111)$$

and using the Steventon site railway track parameters and the Inter-city 125 train parameters, shown in Tabs. 7 and 2, respectively, the sleeper vertical displacement is generated considering the passage of 10 passenger carriages at two speeds; 196 km/h, a typical train speed passing at Steventon site, and 118 km/h, a train speed at which the frequency of the 7th trainload frequency corresponds to the energy harvester undamped natural frequency of the harvester which is described in Section 5.4. The sleeper displacement is differentiated with respect to time to obtain the vertical velocity and acceleration. The time-histories and the power spectral densities (PSDs) of the sleeper vertical acceleration are shown in Fig. 42. At the top of each PSD graph, is shown another horizontal axis, which corresponds to the trainload frequencies, $f \times \frac{S}{L_{\text{car}}}$, i.e., the frequency axis normalized by the ratio between the carriage length and the train speed.

Table 7 – Characteristics railway track at Steventon site.

Rail type [Nm ²]	Trackbed [N/m ²]*	Rail pad [N/m]	Sleeper spacing [m]
CEN 60E1 ($EI = 6.24 \times 10^6$)	$k_{\text{trackbed}} = 1.39 \times 10^7$	Pandrol 6650 ($k_{\text{pad}} = 60 \times 10^6$)	0.65

Source: (TRIEPAISCHAJONSAK, 2012); *(CLEANTE *et al.*, 2019).

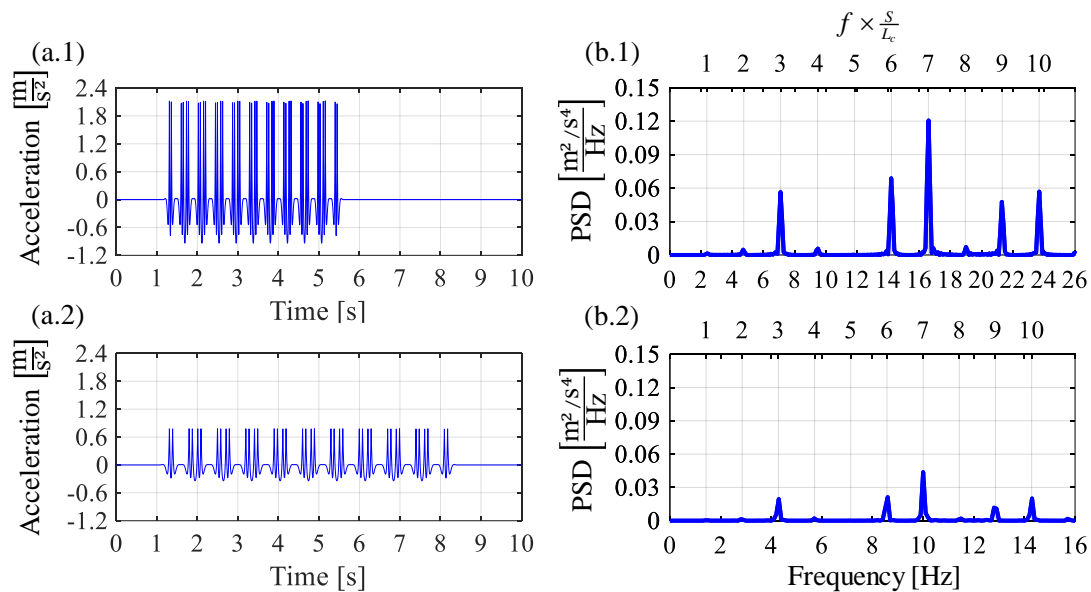
Table 8 – Train parameters.

Train class	Name	Car length [m] – L_{car}	Bogie length [m] – L_{wheel}	Distance between bogie centre [m] – L_{bogie}	Wheel load [kN]*
Mk3	Inter-city 125	23.0	2.6	16.0	21.9

Source: (TRIEPAISCHAJONSAK, 2012); *(CLEANTE *et al.*, 2019).

Note in Figs. 42(a.1) and 42(a.2) that the sleeper vibrates over a shorter time period for a faster train. This means that the device vibration may not reach steady-state, depending on the level of the transducer damping. In this case the transient response has a significant contribution to the total energy harvested (GATTI *et al.*, 2016). Also, note that the higher the train speed, the greater the level of sleeper vibration.

Figure 42. (a) Time-history and (b) power spectral density (PSD) of the sleeper vertical acceleration induced due to the passage 10 passenger carriages of an Inter-city 125 at a speed of 196 km/h (.1) and 118 km/h (.2).



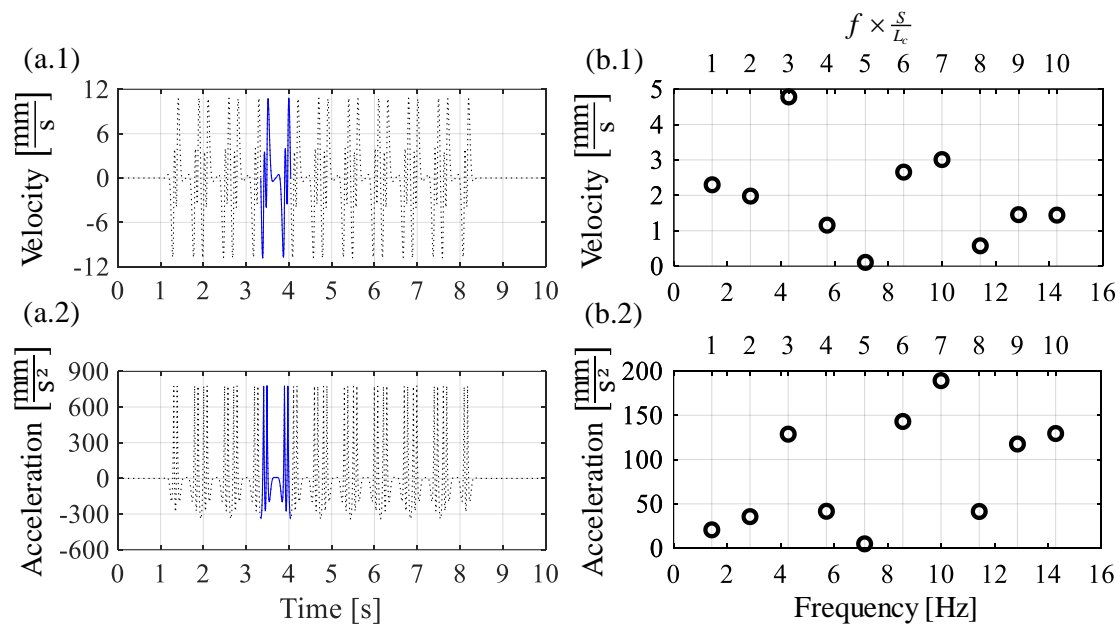
Source: author.

For energy harvesting purposes, the sleeper vibration is better analysed in the frequency domain. In Figs. 42(b.1) and 42(b.2) it can be seen that the slower train speed results in a smaller amplitude of the sleeper vibration, and also shifts the dominant peaks to lower frequencies. Moreover, it is seen that the largest acceleration is at the 7th trainload frequency, independent of the train speed. This frequency, with the largest acceleration amplitude, was found to be the

target frequency at which the harvester can, potentially, scavenge the most energy from the sleeper vibration induced by passing trains (CLEANTE *et al.*, 2016; GATTI *et al.*, 2016).

The sleeper vertical velocity and acceleration time-histories and their corresponding Fourier coefficients, due to the passage of an Inter-city 125 with a speed of 118 km/h are show in Fig. 43. In particular, Fig. 43(.1) shows the sleeper velocity and Fig. 43(.2) shows the sleeper acceleration. For each data, the amplitude of the first 10 Fourier coefficients were extracted only for the vibration corresponding to the passage of the 4th carriage, highlighted in Fig. 43(a.1) and (a.2) and shown in Fig. 43(b). Note in Fig. 43(b.1) that for the velocity, the 3rd trainload frequency has the largest amplitude and in Fig. 43(b.2), for the acceleration, as observed in the PSD of the sleeper vertical acceleration, the 7th trainload frequency is the frequency with the largest amplitude. Moreover, as shown in Chapter 2, the standard deviation of the Fourier coefficients between the full set of passenger carriages is small. Then, further investigation of the electromagnetic energy harvester performance can be carried out considering the amplitude of Fourier coefficients due to the passage of a single carriage.

Figure 43. (a) Time-history and (b) Fourier coefficients of the sleeper vertical velocity (.1) and acceleration (.2) due to the passage of 10 passenger carriages of an Inter-city 125 at a speed of 118 km/h. The black dotted line is the complete time-history and the blue solid line correspond to the vibration due to the passage of the 4th carriage.



Source: author.

5.3 THE LINEAR SINGLE-DEGREE-OF-FREEDOM ELECTROMAGNETIC ENERGY HARVESTER

In this Section, the performance of 5 devices when subjected to the passage of 10 passenger carriages of an Inter-city 125 at Steventon site with a speed of 118 km/h is investigated numerically and analytically. The devices are divided into three groups, where the first two groups are related to devices with no mechanical damping and the third is related to a device with a heavy mechanical damping. Group 1 is comprised of two devices with a small suspended mass, and Group 2 is comprised of two devices with a large suspended mass. In each of these two groups, the effects of the internal coil resistance are also investigated. Group 3 is comprised of a device with a small suspended mass, a heavy mechanical damping and with internal coil resistance. The methodology to investigate the optimization and the analytical expression is first presented, and the results are discussed in Section 5.3.3.

5.3.1 Optimization of a linear electromagnetic energy harvester

For the linear single-degree-of-freedom electromagnetic energy harvester, the governing equations of motion and current are given in Eqs. (34a) and (34b), which are repeated here for convenience, and are given by

$$m\ddot{x}_r(t) + c_m \dot{x}_r(t) + kx_r(t) + Ti(t) = -m\ddot{x}_b(t) \quad (112a)$$

$$L_o \dot{i}(t) + (R_l + R_o)i(t) - T\dot{x}_r(t) = 0. \quad (112b)$$

The study consists of evaluating, for each natural frequency, how much energy is harvested, the corresponding optimum load resistance damping ratio and load resistance, and the resulting maximum relative displacement when the device is subject to the sleeper vertical acceleration shown in Fig. 42(a.2).

Assuming the transducer parameters given in Tab. 9, a numerical integration of Eqs. (34a) and (34b), for each device, is performed in *Matlab* for a range of undamped natural frequency from 1 Hz up to 16 Hz with an increment of 0.1429 Hz, and for a range of load resistances, R_l , from 1 Ω up to 1 M Ω . The resulting current is substituted into the equation of the energy dissipated by the load resistance, Eq. (46), shown here for convenience as

$$E_{elec}(t) = \int_{t_0}^{t_e} v_l(t) i(t) dt = \int_{t_0}^{t_e} R_l i^2(t) dt = \int_{t_0}^{t_e} \frac{v_l^2(t)}{R_l} dt, \quad (113)$$

and integrated over the excitation period, t_e , which corresponds to the period of time at which the train is inducing vibration. This starts at time $t_0 = 1.1$ s and finishes at time $t_f = 8.25$ s. Then, the maximum energy harvested, its corresponding optimum load resistance and the resulting relative displacement, for each natural frequency, are determined. The optimization results for the devices of Groups 1 and 2 are shown, as the blue solid line, in Figs. 44 and 45, respectively, and in Tabs. 10 and 11, respectively. The optimization results for the device of Group 3 is shown in Fig. 46 and in Tab. 12.

Table 9 – The electromagnetic energy harvester parameters.

		Transducer parameters				
		m [kg]	ζ_m	B_l [V/(m/s)]	L_o [mH]	R_o [Ω]
Group 1	Device 1	0.011	0	25	67.3	0
	Device 2					369
Group 2	Device 3	1	0	25	67.3	0
	Device 4					369
Group 3	Device 5	0.011	0.2123	25	67.3	369

Source: author.

5.3.2 Analytical investigation

In this section, using the analytical expression derived in Chapter 3 and the Fourier Coefficients of the sleeper vertical vibration shown in Fig. 43(b), an investigation is carried out into determining, for the transducer undamped natural frequency corresponding to the each of the first 10 trainload frequencies, the amount of energy that the electromagnetic energy harvester can scavenge and its corresponding optimum load resistance. The reason for this investigation is to analyse the transducer performance when subject to a single excitation frequency.

5.3.2.1 Device with no mechanical damping and no internal coil resistance

From the approximate analytical expression of an ideal transducer, i.e., with no mechanical damping and no internal coil resistance, the performance of devices 1 and 3 are

evaluated. Substituting the parameters of devices 1 and 3, from Tab. 9, and the Fourier coefficients from Figs. 43(b.1) and 43(b.2) into Eqs. (73) and (74) which are repeated here for convenience, and are given by

$$E_{elec, \max}(t_e) \approx 0.0475m\ddot{X}_b^2 t_e^2, \quad (113)$$

$$\zeta_{R, \text{opt}} \approx \frac{1}{\pi n}, \quad R_{l, \text{opt}} = \frac{T^2}{4m} t_e \quad \text{and} \quad X_{r, \text{max}} = \frac{\ddot{X}_b}{4\omega_n} (1 - e^{-2}) t_e, \quad (114)$$

the transducer performance for each trainload frequency is calculated and the results are shown in Fig. 44.(1) and Tab. 10 for device 1, and Fig. 45.(3) and Tab. 11 for device 3. The results are discussed in Section 5.3.3.

5.3.2.2 Device with no mechanical damping and with an internal coil resistance

From the approximate analytical expression with internal coil resistance but with no mechanical damping, the performance of devices 2 and 4 are evaluated for the maximum energy harvested, the optimum load resistance damping ratio, the optimum load resistance and the maximum relative displacement. Substituting the parameters of devices 2 and 4 from Tab. 9 and the Fourier coefficients from Figs. 43(b.1) and 43(b.2) into Eqs. (65), (66) and (67), which are repeated here for convenience in the dimensional form, and are given by

$$E_{elec}(t_e) = \frac{m\omega_n \dot{X}_b^2}{4} \left(1 - \frac{3 + e^{-2\omega_n \zeta_{e, \text{opt}} t_e} - 4e^{-\omega_n \zeta_{e, \text{opt}} t_e}}{2\omega_n \zeta_{e, \text{opt}} t_e} \right) t_e \quad (115)$$

where $\zeta_{e, \text{opt}} = \frac{\zeta_{R, \text{opt}} \zeta_{R_o}}{\zeta_{R, \text{opt}} + \zeta_{R_o}}$ and $\zeta_{R_o} = \frac{T^2}{2m\omega_n R_o}$,

$$\zeta_{R, \text{opt}} \approx \frac{\sqrt{3}}{\omega_n t_e} \sqrt{1 - \frac{3 + e^{-2\omega_n \zeta_{R_o} t_e} - 4e^{-\omega_n \zeta_{R_o} t_e}}{2\omega_n \zeta_{R_o} t_e}}, \quad R_{l, \text{opt}} = \frac{T^2}{2m\omega_n \zeta_{R, \text{opt}}} \quad \text{and} \quad X_{r, \text{max}} = \frac{\ddot{X}_b}{2\omega_n^2 \zeta_{eq}} (1 - e^{-\zeta_{eq} \omega_n t_e}), \quad (116)$$

the transducer performance for each trainload frequency is calculated and the results are shown in Fig. 44.(2) and Tab. 10 for device 2, and Fig. 45.(4) and Tab. 11 for device 4. The results are discussed in Section 5.3.3.

5.3.2.3 Device with heavy mechanical damping and with an internal coil resistance

From the approximate analytical expression of an energy harvester with a heavy mechanical damping and internal coil resistance, the performance of device 5 is evaluated for each natural frequency corresponding to the first 10 trainload frequencies. The maximum energy harvested, the optimum load resistance damping ratio, the optimum damping ratio and the maximum relative displacement are determined. Substituting the parameters of device 5, from Tab. 9, and the Fourier coefficients, from Fig. 43 into Eqs. (53), (54) and (55), which are repeated here for convenience in the dimensional form, and are given by

$$E_{elec}(t_e) = \frac{t_e T^2 m^2 \ddot{X}_b^2}{8c_m (R_o c_m + T^2)}, \quad (116)$$

$$\zeta_{R,opt} = \frac{\zeta_m \zeta_{R_o}}{\zeta_m + \zeta_{R_o}}, \text{ and } R_{l,opt} = \frac{T^2}{c_m} + R_o, \quad (117)$$

the transducer performance for each trainload frequency is calculated and the results are shown in Fig. 46 and Tab. 12. The results are discussed in Section 5.3.3.

5.3.3 Passing train results

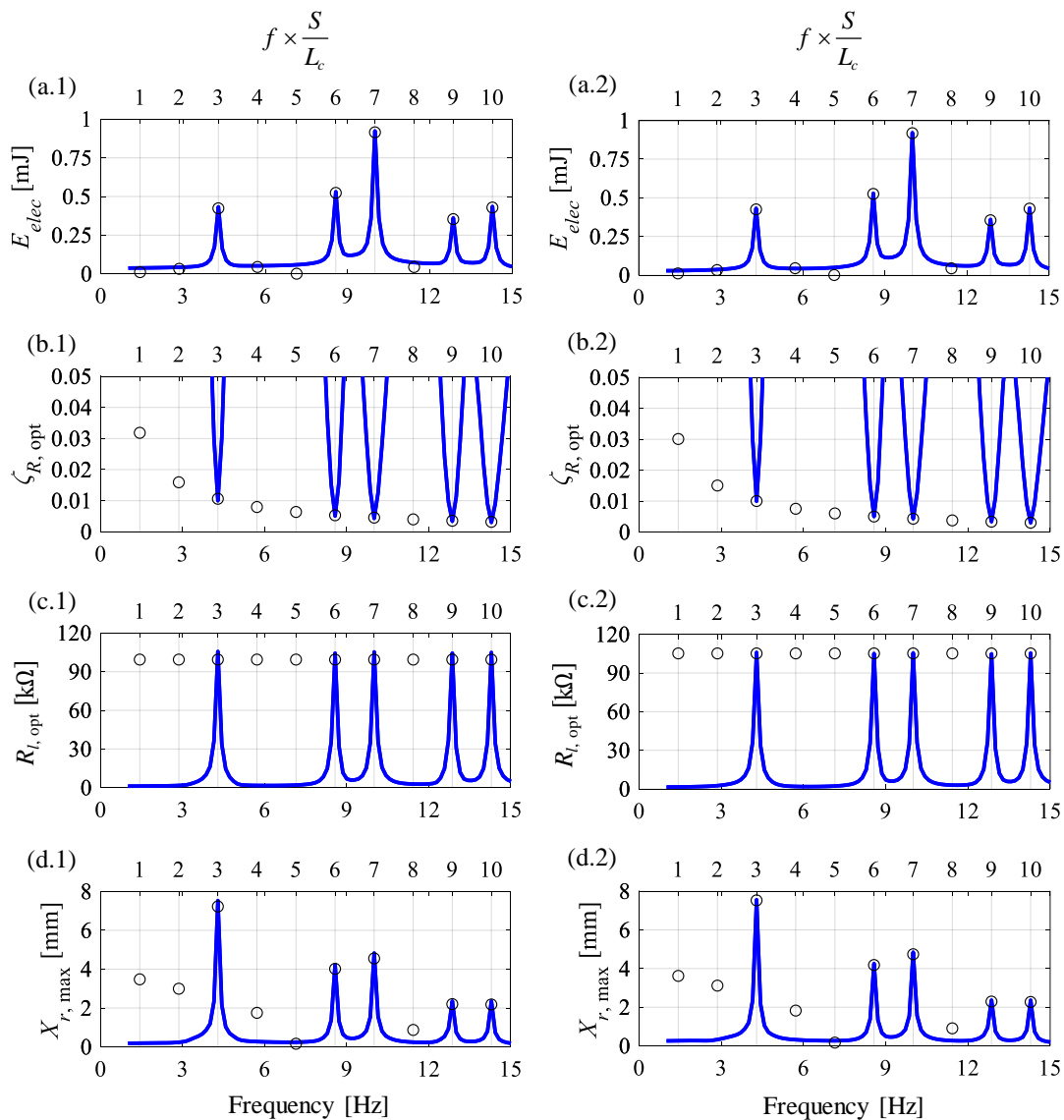
In this Section, the results obtained numerically and analytically, for each group of transducer devices, are discussed.

5.3.3.1 Results for Group 1: transducers with a suspended mass $m = 0.011$ kg and no mechanical damping

Figure 44 shows the numerical optimization (blue solid line) and the analytical (black circle) results for two electromagnetic energy harvesters with a small suspended mass, $m = 0.011$ kg. In particular, Fig. 44(.1) is the ideal device, i.e., with no mechanical damping and no internal coil resistance, and Fig. 44(.2) is the device with internal coil resistance. In Fig. 44(a.1) it is noted that the natural frequency at which the transducer harvests large levels of energy occurs at the frequency corresponding to the 7th trainload frequency. This is in accordance with (GATTI *et al.*, 2016) who observed that for a short period of excitation, the

device natural frequency should correspond to the frequency with the largest acceleration amplitude.

Figure 44. Results for each natural frequency of two electromagnetic energy harvester devices when subjected to a base vibration induced by the sleeper vertical vibration due to the passage of 10 passenger carriages of an Inter-city 125 travelling at Steventon site with a speed of 118 km/h. Device 1, (.1), comprises of $m=0.011$ kg, $\zeta_m=0$ and $R_o=0$ Ω ; Device 2, (.2), comprises of $m=0.011$ kg, $\zeta_m=0$ and $R_o=369$ Ω . (a) The maximum energy dissipated; (b) the optimum load resistance damping ratio; (c) the corresponding load resistance; and (d) the resulting relative displacement. The blue solid line denotes the numerical results and the black circles denote the analytical results. At the top of each graph is shown a second horizontal axis which corresponds to the trainload frequencies.



Source: author.

From Fig. 44(b.1), it is observed that to harvest the maximum energy available from the vibrating source, the optimum load resistance damping ratio is small. From Fig. 44(c.1), as expected to achieve the open-circuit condition, the optimum load resistance is large, mainly at frequencies with dominant acceleration amplitude. Additionally, Fig. 44(d.1) shows that the maximum relative displacement is high when the device damping is small. However, observe that the largest relative displacement occurs at the 3rd trainload frequency, which is the frequency with the largest velocity amplitude.

Figure 44(.2) shows the result when the transducer internal coil resistance is considered. It can be seen that the transducer performance is similar as observed in Fig. 44(.1), which is for the ideal transducer. For this particular device, due to the small suspended mass ($m = 0.011$ kg), the internal coil resistance damping ratio is high. It varies from $0.6 < \zeta_{R_o} < 12$ as the transducer natural frequency is decreased. As observed in Chapter 3, when $\zeta_{R_o} \gg \zeta_{R,opt}$, the equivalent electrical damping ratio is simply $\zeta_e \approx \zeta_R$ and the internal coil resistance can be neglected.

Analysing the results obtained using the analytical expression, which are the black circles, it is noted that at the frequencies corresponding to the 5 largest acceleration amplitudes, the results are similar to those found in the numerical optimization. The differences observed at the other frequencies are related with the small acceleration amplitude. While in the numerical optimization, the transducer is found to have high damping, broadening the device bandwidth to increase the contribution of the adjacent excitation frequencies, the analytical expression only takes into consideration a single excitation frequency.

A comparison between the numerical and analytical results obtained for the optimum device natural frequency is shown in Tab. 10. It is clear that devices 1 and 2 have similar results, which means that for this particular suspended mass, the internal coil resistance has a negligible effect on the device performance. Moreover, the analytical results are approximately the same as the results obtained numerically.

Table 10 – Results for the energy harvester with $m = 0.011$ kg at the natural frequency corresponding to the 7th trainload frequency.

		E_{elec} [mJ]	$\zeta_{R,opt}$	$\zeta_{eq,opt}$	$R_{l,opt}$ [k Ω]	$X_{b,max}$ [mm]
Numerical	Device 1 ($R_o = 0 \Omega$)	0.92	0.0043	0.0043	105.3	4.8
	Device 2 ($R_o = 369 \Omega$)	0.92	0.0043	0.0043	105.3	4.8
Analytical	Device 1 ($R_o = 0 \Omega$)	0.91	0.0045	0.0045	99.4	4.5
	Device 2 ($R_o = 369 \Omega$)	0.91	0.0045	0.0045	99.4	4.5

Source: author.

5.3.3.2 Results for Group 2: transducers with a suspended mass $m = 1$ kg and no mechanical damping

Figure 45 shows the optimization (blue solid line) and the analytical (black circles) results for an electromagnetic energy harvester with a suspended mass of $m = 1$ kg. A comparison between the numerical and analytical results obtained for the optimal device natural frequency, corresponding to the 7th trainload frequency is shown in Tab. 11.

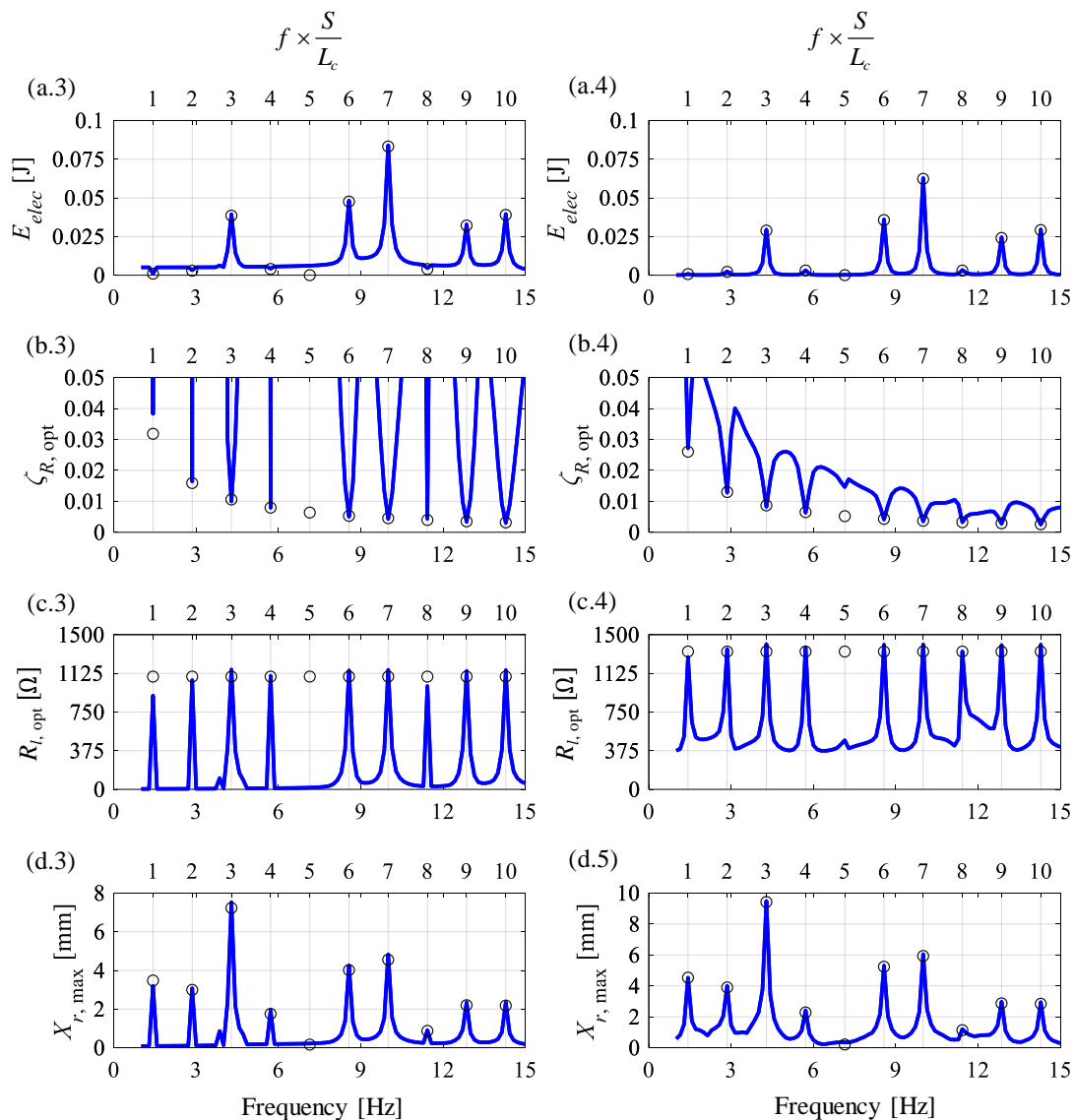
In particular, Fig. 45(.3) corresponds to the ideal device, i.e., with no mechanical damping and no internal coil resistance, and Fig. 45(.4) corresponds to the device considering the internal coil resistance. Note that despite the difference in magnitude of the energy harvested, Fig. 45(a.3), and of the optimum load resistance, Fig. 45(c.3), the results in Fig. 45(.3) shows that the transducer behaviour is similar to device 1, with a mass $m = 0.011$ kg. The maximum energy harvested occurs at the 7th trainload frequency. However, because the maximum energy harvested by the ideal linear transducer is directly proportional to the size of the suspended mass, as seen in Eqs. (113), the energy harvested by device 3 is $\frac{1}{0.011}$ times greater than by the device 1. Also, the load resistance is inversely proportional to the size of the suspended mass, as seen in Eqs. (116), and the load resistance is $\frac{1}{0.011}$ lower than the one found for device 1.

Figure 45(.4) shows the results for the electromagnetic energy harvester with internal coil resistance. Note in Fig. 45(a.4) that the device natural frequency corresponding to the 7th trainload frequency is still the target frequency. However, due to the size of the suspended mass, the effect due the internal coil resistance is relevant, dissipating part of the energy introduced from the vibrating source. Moreover, as seen in Tab. 11, for device 4 the optimum equivalent damping ratio is $\zeta_{eq,opt} = 0.0028$. Observe that this is smaller than the optimum equivalent damping ratio found for the ideal transducer, device 3. This is the detrimental effect of the internal coil resistance at which dissipates part of the energy introduced by the vibrating source and for this particular case, cause a reduction of 26% in the transducer performance.

In Fig. 45(b.4), it is seen that the optimum load resistance damping ratio is small for each trainload frequency. As seen in Tab. 11, the optimum load resistance damping ratio for the 7th trainload frequency for device 4 is smaller than for device 3. It is interesting to note that because the load resistance damping ratio cannot be higher than the internal coil resistance damping ratio, for the frequencies different from the corresponding trainload frequencies, the optimum damping is limited by the internal coil resistance damping ratio. Additionally, because

the equivalent damping ratio is lower for device 4, the maximum relative displacement found for device 3 is greater than for device 4, as seen in Fig. 45(d.3).

Figure 45. Results for each natural frequency of two electromagnetic energy harvester devices when subjected to a base vibration induced by the sleeper vertical vibration due to the passage of 10 passenger carriages of the Inter-city 125 travelling at Steventon site with a speed of 118 km/h. Device 3, (.3), comprises of $m=1$ kg, $\zeta_m=0$ and $R_o=0$ Ω ; Device 4, (.4), comprises of $m=1$ kg, $\zeta_m=0$ and $R_o=369$ Ω . (a) The maximum energy dissipated; (b) the optimum load resistance damping ratio; (c) the corresponding load resistance; and (d) the resulting relative displacement. The blue solid line denotes the numerical results and the black circles denote the analytical results. At the top of each graph is shown a second horizontal axis which corresponds to the trainload frequencies.



Source: author.

A comparison between the numerical and analytical results obtained for the optimum device natural frequency, corresponding to the 7th trainload frequency, are shown in Tab. 11. It is clear that the analytical results are approximately the same as the results obtained numerically. Also, due to the large size of the suspended mass, the internal resistance reduces the transducer performance. This can be seen by comparing the performance of device 4 with the ideal transducer, device 3. However, even with internal coil resistance, device 4 harvested 674 times more energy than the device 1, which is the ideal transducer for with a mass of $m = 0.011$ kg.

Table 11 – Results for the electromagnetic energy harvester with $m = 1$ kg at the natural frequency corresponding to the 7th trainload frequency.

		E_{elec} [J]	$\zeta_{R,opt}$	$\zeta_{eq,opt}$	$R_{L,opt}$ [Ω]	$X_{b,max}$ [mm]
Numerical	Device 3 ($R_o = 0 \Omega$)	0.84	0.0043	0.0043	1159	4.8
	Device 4 ($R_o = 369 \Omega$)	0.62	0.0035	0.0028	1405	6.0
Analytical	Device 3 ($R_o = 0 \Omega$)	0.83	0.0045	0.0045	1094	4.5
	Device 4 ($R_o = 369 \Omega$)	0.62	0.0037	0.0029	1336	5.9

Source: author.

5.3.3.3 Results for Group 3: electromagnetic energy harvester with a heavy mechanical damping

In this section, the numerical and analytical results for an electromagnetic energy harvester with heavy mechanical damping and with internal coil resistance, shown in Fig. 46 and in Tab. 12, are discussed. In particular, Fig. 46(a) shows the total energy harvested for each natural frequency, where it can be seen that the numerical results are different from the analytical results. The reason for this is similar to the other devices. The analytical equations only consider a single excitation frequency and the numerical optimization, to maximize the energy harvested, increases the contribution of the adjacent excitation frequency increasing the equivalent damping ratio. This is achieved by setting the load resistance damping ratio to be high. However, because the mechanical damping is high, differences are observed even for the frequencies with the largest acceleration amplitudes. This is shown in Fig. 46(b) and Fig. 46(c) which shows that the numerical optimum load resistance and the optimum load resistance are, respectively, greater and smaller than the results found by the analytical investigation.

By comparing the amount of energy harvested determined numerically and analytically from the device with a natural frequency corresponding to the 7th trainload frequency, it is seen

that when the adjacent excitation frequencies are considered, the energy harvested is about 2 times greater than from vibration induced by a single frequency. Also, note that the detrimental effect due to damping, the energy harvested by device 5 is about 38 times lower if compared it with the ideal transducer, device 1.

Table 12 – Results for the electromagnetic energy harvester with a heavy mechanical damping at the natural frequencies corresponding to the 3rd and the 7th trainload frequencies.

Target trainload frequency		E_{elec} [μ J]	$\zeta_{R,opt}$	$\zeta_{eq,opt}$	$R_{L,opt}$ [Ω]	$X_{b,max}$ [mm]
Numerical	3 rd	28	0.7675	0.6768	1902	0.27
	7 th	23.8	0.2379	0.4115	1900	0.13
Analytical	3 rd	13	0.19	0.40	5338	0.22
	7 th	11	0.18	0.37	2499	0.06

Source: author.

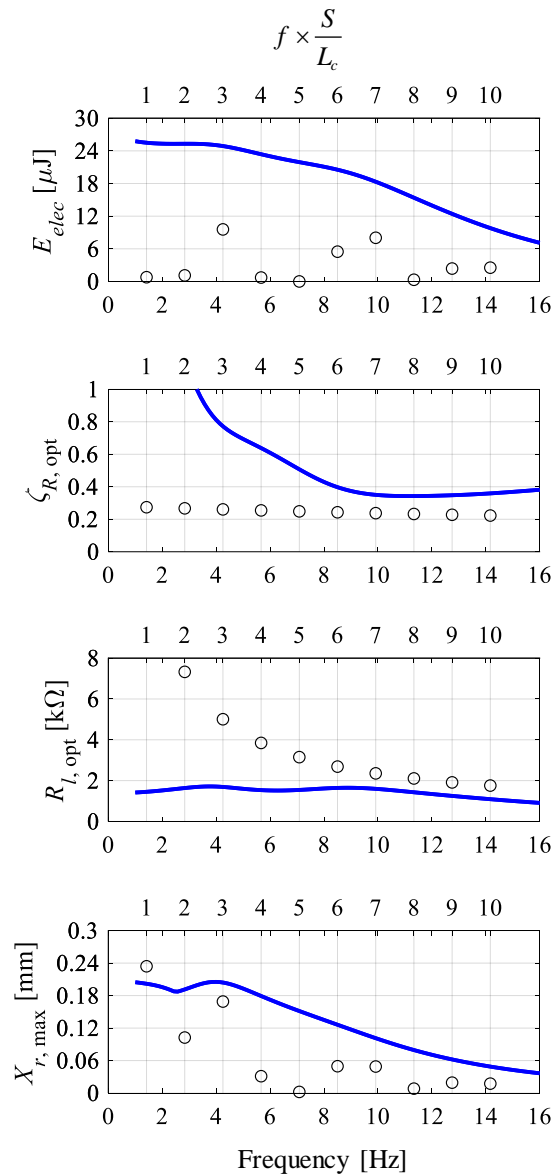
It is interesting to note in Fig. 46 that for both, numerical and analytical results, the frequency corresponding to the 3rd trainload frequency harvest more energy than the 7th trainload frequency.

When the transducer is operating in its ideal condition, the equivalent damping ratio is small, and the maximum energy harvested occurs with the device in the transient regime. Note from Eq. (113) that the dimensional expression for the maximum energy harvested, $E_{max} = 0.048m\ddot{X}_b^2 t_e^2$, is a function of the base acceleration, which suggests that the maximum energy will occur at the frequency with the largest acceleration amplitude. However, when the transducer equivalent damping ratio is high, $\zeta_{eq} \gg \frac{1}{\pi n}$, due to a high ζ_m or a small ζ_{R_o} , the maximum energy occurs with the device in the steady-state regime. From Eq. (116), it can be noted that the dimensional expression for the maximum energy harvested is in function of the base acceleration and of the mechanical damping. Therefore, when considering only the steady-state condition, the maximum energy equation, $E_{max} = \frac{mT\ddot{X}_b^2 t_e^2}{c_m(c_m R_o + T^2)}$, is a function of the multiplication between the base acceleration and velocity. For the case where $c_m R_o \gg T^2$, Eq. (116), is a function of the velocity and the maximum energy harvested will occur at the frequency with the largest velocity amplitude.

For this particular train and railway track, if the Fourier coefficients of the sleeper vertical velocity are multiplied by the Fourier coefficients of the sleeper vertical acceleration, Fig. 43(b.1) and 43(b.2), the magnitude of the 3rd trainload frequency is slightly larger than the

magnitude of the 7th trainload frequency. This is similar to the results found by the analytical expression for the maximum energy harvested shown in Tab. 12.

Figure 46. Results for each natural frequency of the electromagnetic energy harvester device 5, when subject to a base vibration induced by the sleeper vertical vibration due to the passage of 10 passenger carriages of the Inter-city 125 at a speed of 118 km/h: (a) the maximum energy dissipated; (b) the optimum load resistance damping ratio; (c) the corresponding load resistance; and (d) the resulting relative displacement. The blue solid line denotes the numerical results and the black circle denotes the analytical results. At the top of each graph is presented a second horizontal axis which corresponds to the trainload frequencies.



Source: author.

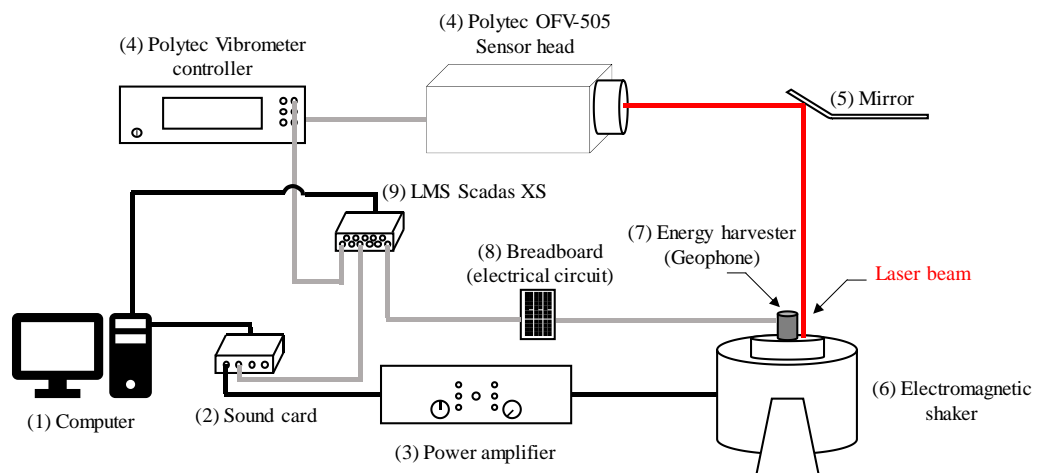
5.4 HARVESTING ENERGY FROM THE RAILWAY TRACK VIBRATION

In previous sections, the performance of a linear single-degree-of-freedom electromagnetic energy harvester has been investigated numerically and analytically. To validate the investigation carried out in Chapter 3, an experiment is performed using a geophone coupled to an electromagnetic shaker, which emulates the railway track vibration in a laboratory-based system.

5.4.1 The experimental setup

A schematic diagram of the experimental setup is shown in Fig. 47. It is comprised of (1) a computer, to generate the excitation signal and later, to post-process the measured data; (2) a Behringer UCA222 USB sound card, which comprises of two outputs and two inputs to convert from digital to analogue the excitation signal generated on the computer; (3) a Crow XL 2500, an analogue power amplifier, (4) a Polytec laser vibrometer OFV-505, to measure the shaker base velocity; (5) a mirror, to reflect in 90° the laser beam, (6) an electromagnetic shaker, (7) a Geophone SM-24, as the energy harvester, (8) a breadboard, to couple the electrical circuit and (9) a LMS Scadas XS to recorded the sound card output signal, the shaker velocity and the voltage across the energy harvester.

Figure 47. The schematic of the experimental setup.



Source: author.

The experiment involved three steps: 1 – identification of the geophone parameters; 2 – a numerical investigation of the Geophone as an energy harvester to determine the maximum

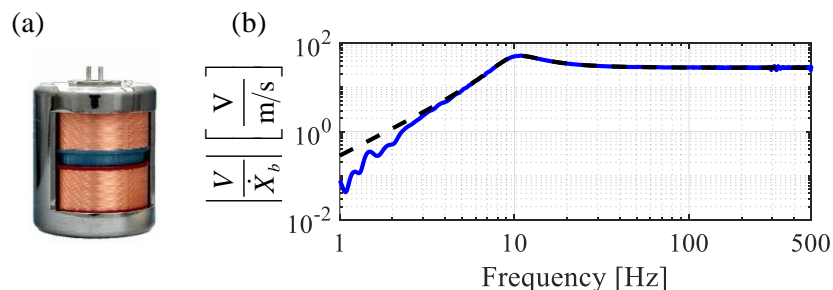
energy that can be scavenged and its corresponding optimum load resistance; 3 – using compensator filter proposed in Chapter 4, emulate the sleeper vertical vibration in the laboratory-based system and 4 – an experiment to harvest the energy from the sleeper vertical vibration induced due to a passing train emulated in a laboratory-based system.

5.4.2 The geophone

The Geophone SM-24, shown in Fig. 48(a), is the device chosen to be the energy harvester in this experiment. This geophone is a commercial electromagnetic transducer used as a sensor to measure seismic vibration. This device was chosen as it was already fabricated and attended to part of the desired experimental requirement. It had a low natural frequency which corresponds to the 7th trainload frequency of the sleeper vertical vibration induced due to a passing train.

To use the Geophone SM-24 as the energy harvester, the transducer parameters needed to be known, so that the correct electrical load could be connected. To determine the transducer parameters, an experiment was carried out to identify the FRF between the voltage across the geophone terminals and its base velocity. By a curve fitting optimization procedure, the parameters of the transducer could be identified.

Figure 48. (a) Example of the Geophone SM-24 and (b) Frequency Response Function (FRF) between the voltage across the geophone terminals and its base velocity. Blue solid line (—) is the FRF obtained experimentally and the black dashed line (--) is the FRF obtained from the optimum curve fitting.



Source: author.

The experimental setup, described in Fig. 47, was performed with the geophone in the open-circuit condition. The shaker was excited with a random signal of 60 s duration. The voltage across the geophone and the shaker velocity signal were sampled at a frequency of

$F_s = 1024$ Hz. The shaker velocity was measured using a Polytec laser vibrometer OFV-505, and the signal were acquired using the LMS Scadas XS. The FRF between the voltage across the geophone terminals and its base was calculated in *Matlab* using the *tfestimate* function and shown in Fig. 48(b) as a blue solid line.

The transducer parameters were identified by minimising the difference (in a mean squares sense) between the measured and the analytical expression for the FRF when the transducer is in open-circuit which is given by,

$$\left| \frac{V}{\dot{X}_b} \right| = \frac{j\omega^2 mBl}{2m\omega_n \zeta_m \omega + j(\omega^2 m - k)}, \quad (118)$$

where Bl is the electromagnetic sensitivity, ζ_m is the mechanical damping ratio, k is the stiffness, m is the suspended mass and is fixed to $m = 0.011$ kg (ION PRODUCTS, 2009), $\omega_n = \sqrt{k/m}$ is the undamped natural frequency, ω is the angular excitation frequency and $j = \sqrt{-1}$.

Using the *Matlab* function *fmincon*, the parameters ζ_m , k and Bl of the Geophone were determined by calculating, for a frequency range of 7 Hz up to 100 Hz, the minimum sum of the difference between the measured and Eq. (118). To identify the transducer internal impedance, a digital Minipa Et-2082c multimeter was used to measure the internal resistance and the internal inductance. The identified parameters are shown in Tab. 13.

Table 13 – The Geophone SM-24 specification.

Parameter	Value
Mass (m) [kg]*	0.011
Undamped natural frequency (f_n) [Hz]	9.91
Mechanical damping ratio (ζ_m)	0.2731
Sensitivity (Bl) [V/N]	28
Internal coil resistance (R_o) [Ω]	365
Internal coil inductance (L_o) [mH]	64.2

Source: author and *(ION PRODUCTS, 2009).

Equation (118) is plotted, for the geophone parameters given in Tab. 13, in Fig. 48(b). It can be seen that there is good agreement between the measured and the analytical. From Tab. 13, it is observed that the mechanical damping ratio is high. As discussed before, the Geophone SM-24 is a sensor transducer and it is clear that it is not the best device to use as an energy

harvester. Moreover, note that the device undamped natural frequency is 9.91 Hz, which suggests that an Inter-city 125 train with a speed of 117.2 km/h is the target train whose its 7th trainload frequency coincides with the device natural frequency. However, due to the heavy mechanical damping, a train passing with a speed of 273.5 km/h whose its 3rd trainload frequency coincides with the device natural frequency is also evaluated.

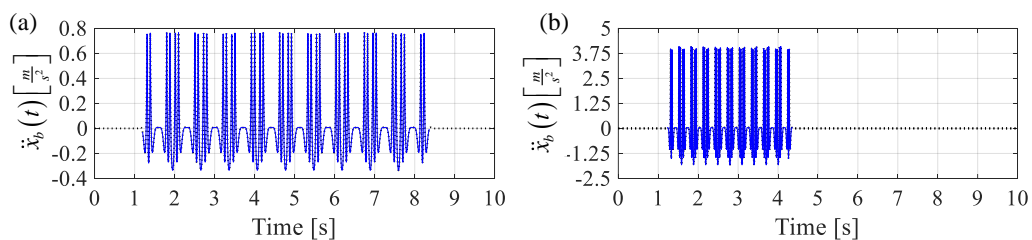
5.4.3 Harvesting energy from the sleeper vibration induced due to a pass-by train: numerical

In this Section, a numerical investigation is carried out to determine the optimum load resistance to be attached to the electrical circuit and the total energy harvested by the Geophone SM-24, shown in Fig. 48, when it is subject to the sleeper vertical vibration due to the passage of an Inter-city 125 train travelling at the Steventon site with the speeds of 117.3 km/h and 273.5 km/h. Although this transducer is not designed for energy harvesting, it is used to validate the model, which can then be used to determine the optimum design parameters for an energy harvester.

5.4.3.1 The vibrating source

The sleeper vibration is generated in *Matlab*, for the respective train speeds, by substituting the Steventon site railway track parameters and the parameters of 10 passenger carriages of an Inter-city 125 train, given in Tabs. 7 and 2, into the analytical model given in Eq. (111). Examples of the sleeper vertical acceleration time-histories due to the train passing at the speeds of 117.3 km/h and 273.5 km/h are shown in Fig. 49.

Figure 49. The sleeper vertical acceleration induced due to the passage of an Inter-city 125 train travelling at Steventon site with the speeds of (a) 117.32 km/h and (b) 273.5 km/h. The black dotted line (.....) is the complete time-history and the blue solid line (—) comprises only the excitation period.



Source: author.

5.4.3.2 Numerical optimization and energy harvested

An investigation into the performance of the Geophone energy harvester when subject to the sleeper vertical vibration induced by a passing train. Using the Geophone SM-24, whose natural frequency is 9.91 Hz, an optimization is carried out to determine, from a load resistance range of 1 Ω up to 1 M Ω , the optimum load resistance, the energy harvested and the resulting relative displacement when the transducer natural frequency coincides with the 7th trainload frequency of the Inter-city 125 train passing with the speed of 117.3 km/h and when coincides with the 3rd trainload frequency of the Inter-city 125 train passing with the speed of 273.5 km/h.

Substituting the sleeper vertical accelerations, shown in Fig. 49, and the Geophone parameters, given in Tab. 13, into Eqs. (34a) and (34b), the governing equations of motion and current are numerically integrated. The resulting current is substituted into Eq. (113), given by

$$E_{elec}(t) = \int_{t_0}^{t_e} v_l(t) i(t) dt = \int_{t_0}^{t_e} R_l i^2(t) dt ,$$

which is then integrated over the time at which the train is inducing vibration, i.e., from $t_0 = 1.1$ s to $t_f = 8.25$ s for a train travelling at 117.3 km/h and from $t_0 = 1.3$ s to $t_f = 4.47$ s for a train travelling at 273.5 km/h. The optimum load resistances together with the total harvested energies are shown in Tab. 14. The resulting voltage across the load resistance and the resulting geophone relative displacement when the optimum load resistance is attached to the energy harvester are shown in Fig. 50 for the train passing with the speed of 117.3 km/h and in Fig. 51 for the train passing with the speed of 273.5 km/h.

Table 14 – The numerical results for the Geophone SM-24 as the energy harvesting device when its base is subjected by the vibration induced due to the passage of an Inter-city 125 at Stevenston site.

Train speed [km/h]	Target trainload frequency	E_{elec} [μ J]	$\zeta_{R_{opt}}$	R_l [Ω]	$ X_{b,max} $ [mm]
117.2	7 th	19.7	0.2935	1944	0.11
273.47	3 rd	116.2	0.4993	1044	0.28

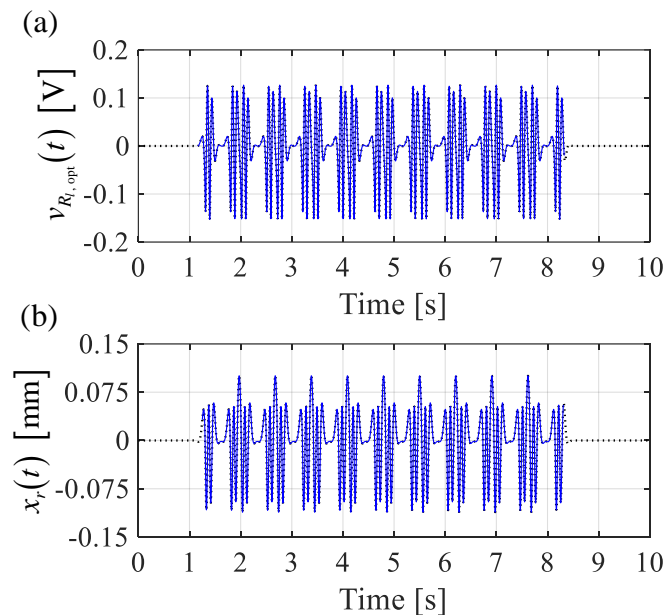
Source: author.

Note from Tab. 14 that the faster train harvest more energy than the slower train. There are two main reasons for this. As discussed in Chapter 2 the sleeper vibration is linear related

to the train speed. Therefore, the faster train generates large levels of vibration than the slower trains. Also, as discussed in Section 1.3.3.3, due to high damping, the transducer is operating in the steady-state regime, which changes the target frequency from the frequency with the largest acceleration amplitude to the frequency with the largest velocity amplitude. For the case studied, the Geophone SM-24, is the 3rd trainload frequency.

For the train passing with the speed of 117.3 km/h, it was found that with a load resistance of $R_{l,opt}=1944 \Omega$, a total energy of $E_{elec}=19.7 \mu\text{J}$ is harvested for a maximum relative displacement of $X_{b,max}=0.11 \text{ mm}$. For the train passing with the speed of 273.5 km/h, it was found that with a load resistance of $R_{l,opt}=1044 \Omega$, a total of $E_{elec}=116.2 \mu\text{J}$ is harvested for a maximum relative displacement of $X_{b,max}=0.28 \text{ mm}$. For both train speeds, the maximum relative displacement is not greater than the maximum allowable coil displacement, which is 2 mm (ION PRODUCTS, 2009).

Figure 50. The energy harvester results with an attached load resistance of $R_l=1944 \Omega$ when subjected to sleeper vibration induced by an Inter-city 125 passing train with a speed of 117.2 km/h: (a) the voltage across the load resistance and (b) the relative displacement. The black dotted line (.....) is the complete time-history and the blue solid line (—) comprises only the excitation period.

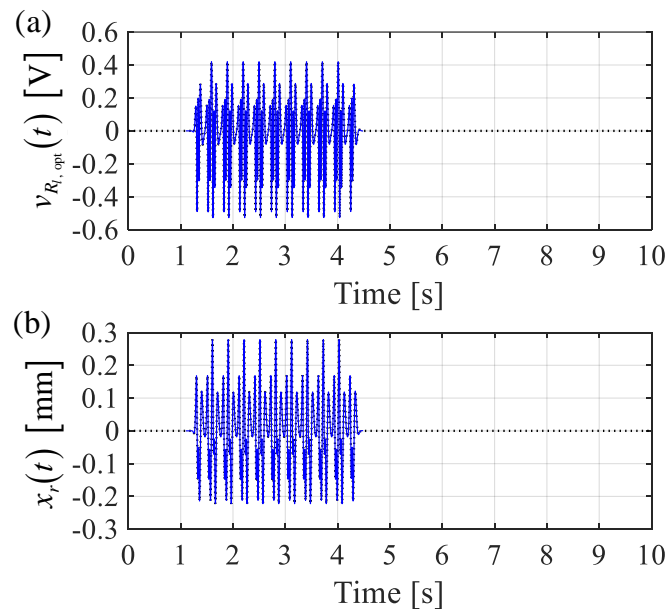


Source: author.

From Figs. 50 and 51 it is clear that the mechanical damping in the geophone limits the harvester performance. For the transducer to achieve its maximum performance, a small load

resistance is required, which, in terms of an equivalent load resistance damping ratio is high. Observe that after the base excitation ceases, the device motion, and consequently the voltage across the load resistance, abruptly goes to zero. Also, note that the combination of a small peak-to-peak voltage and a high load resistance results in a small energy harvested for both train speeds.

Figure 51. The energy harvester results with an attached load resistance of $R_l = 1144 \Omega$ when subjected to sleeper vibration induced by an Inter-city 125 passing train with a speed of 273.5 km/h: (a) the voltage across the load resistance and (b) the relative displacement. The black dotted line (.....) is the complete time-history and the blue solid line (—) comprises only the excitation period.



Source: author.

5.4.4 Harvesting energy from the sleeper vibration induced due to a passing train: experiment

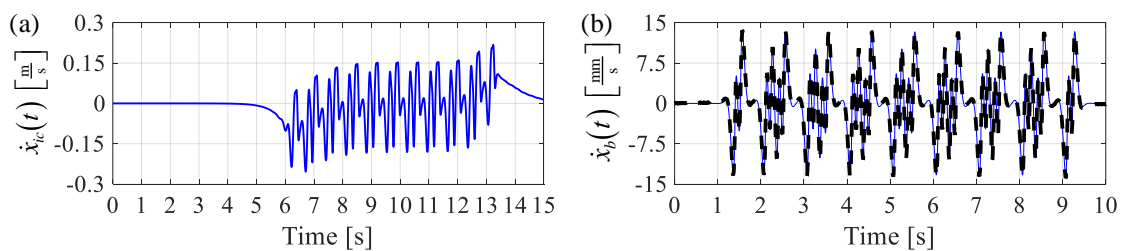
In this Section, an experiment is performed to validate the results found in the previous section. The experimental setup is shown in Fig. 47. The experiment comprises of harvest the energy from the emulated sleeper vertical vibration, induced by a passing train, on the electromagnetic shaker, using the Geophone SM-24 as the electromagnetic energy harvester. The train is the same used in the numerical investigation and comprises of 10 passenger carriages of an Inter-city 125 train travelling at Steventon site with the speeds of 117.3 km/h and 273.5 km/h.

5.4.4.1 The sleeper vibration time waveform replicated on the electromagnetic shaker

To emulate the sleeper vibration on the electromagnetic shaker, the dynamics of the system comprising the computer, the sound card, the power amplifier and the electromagnetic shaker, shown in Fig. 47, are removed using the compensator filter designed in Chapter 4. The proposed compensator filter is based on the estimated system FRF mobility. Therefore, the excitation signals with the system dynamic compensation are generated in *Matlab* by creating the desirable sleeper vertical velocity induced due to an Inter-city 125 train passing with the speeds of 117.2 km/h and 273.5 km/h and convolving it with the compensator filter.

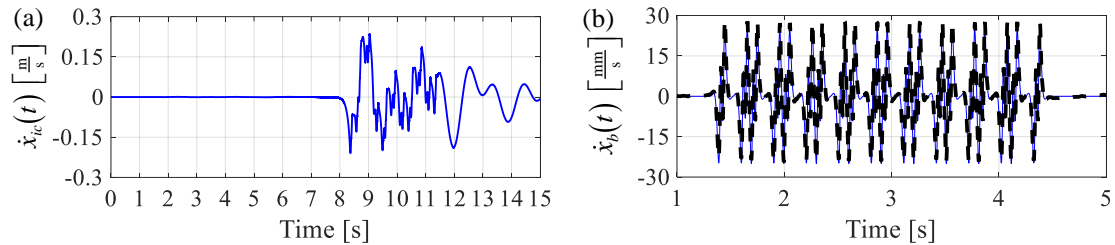
The compensated excitation signals with a time duration of 15 s and a sampling frequency of $F_s = 1024$ Hz are shown in Figs. 52 and 53 together with the measured shaker velocity and their desirable shaker response for the train passing with the speeds of 117.3 km/h and 273.5 km/h, respectively. It can be seen that the compensator filter was able to remove the system dynamics and emulate with a relatively good precision, the time waveform of the sleeper vertical vibration on the electromagnetic shaker.

Figure 52. Time waveform replication of the sleeper vertical velocity induce due to an Inter-city 125 passing with the speed of 117.3 km/h. (a) The compensated excitation signal and (b) the desired shaker velocity (blue solid line, —) and the measured shaker velocity (black dashed line, - -).



Source: author.

Figure 53. Time waveform replication of the sleeper vertical velocity induced due to the passage on an Inter-city 125 with a speed of 273.5 km/h. (a) The compensated excitation signal and (b) the desired shaker velocity (blue solid line, —) and the measured shaker velocity (black dashed line, - -).



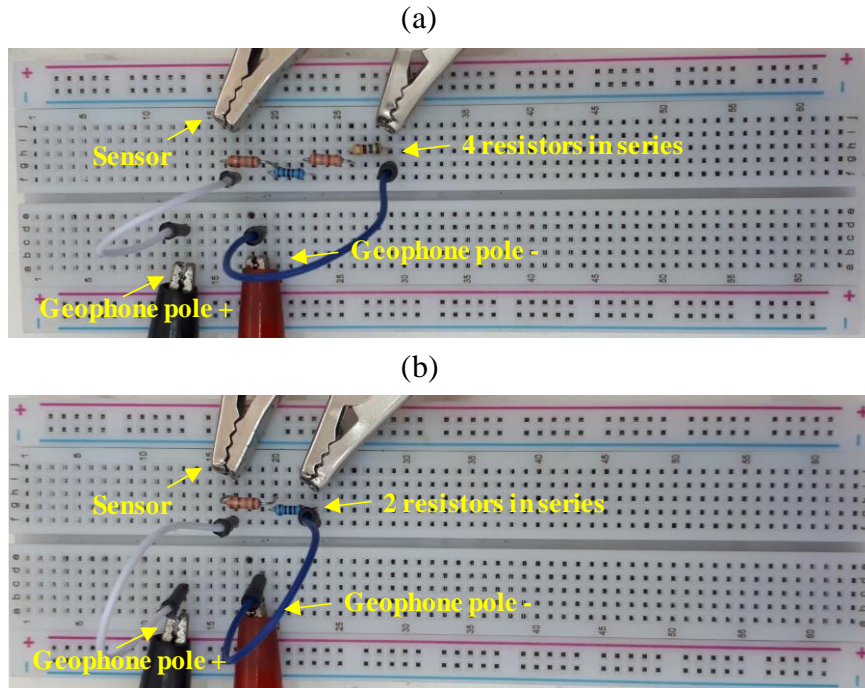
Source: author.

5.4.4.2 The electrical circuit

From the energy supplied by the sleeper vibration, only the part dissipated by the load attached to the electrical energy harvester circuit representative of the energy that can be harvested. The aim here is not to convert the sleeper vibration into electrical energy but to validate the energy harvesting model by measuring the voltage across the load and calculating its total dissipated energy. Therefore, the electrical circuits are mounted on a breadboard and consist of a load connected in series with the geophone and a sensor connected in parallel with the load. Because the geophone inductance is neglected for this application, the load is simply a resistor with the optimum resistance for each passing train, which is given in Tab. 14. The voltage across the load is measured using the acquisition system.

For the train passing with the speed of 117.3 km/h, whose the target frequency is the 7th trainload frequency, the load is comprised of four resistors in series, which gives an equivalent resistance of $R_{l,eq} = 1903 \Omega$. An example of this electrical circuit is shown in Fig. 54(a). For the train passing with the speed of 273.5 km/h, whose the target frequency is the 3rd trainload frequency, the load is comprised of two resistors in series, which gives an equivalent resistance of $R_{l,eq} = 1173 \Omega$. An example of this electrical circuit is shown in Fig. 54(b). Note that both load resistances are slightly different from the optimal found in Tab. 14. This is due to the difficulty of finding the equivalent resistance for that value.

Figure 54. The schematic of the energy harvester electrical circuit to scavenge the maximum energy for the train with a speed of (a) 117.3 km/h with a $R_{l,eq} = 1903 \Omega$ and (b) 273.5 km/h with a $R_{l,eq} = 1173 \Omega$.



Source: author.

5.4.4.3 The harvested energy from the sleeper vibration emulated on an electromagnetic shaker

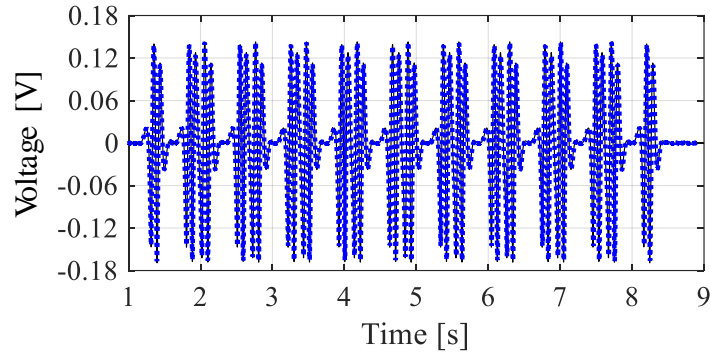
When the system shown in Fig. 47 is excited with the compensated excitation signals, given in Figs. 52(a) and 53(a), the electrodynamic shaker behaves similar to the sleeper, inducing the sleeper vibrations due to a passing train, to the base of the transducer. The measured voltage across the load resistances are shown in Fig. 55 for the train passing with the speed of 117.3 km/h and Fig. 56 the train with the speed of 273.5 km/h.

Substituting the resulting voltages and its corresponding load resistances into the energy harvested equation, given by

$$E_{elec}(t) = \int_{t_0}^{t_f} \frac{V_l^2(t)}{R_l} dt$$

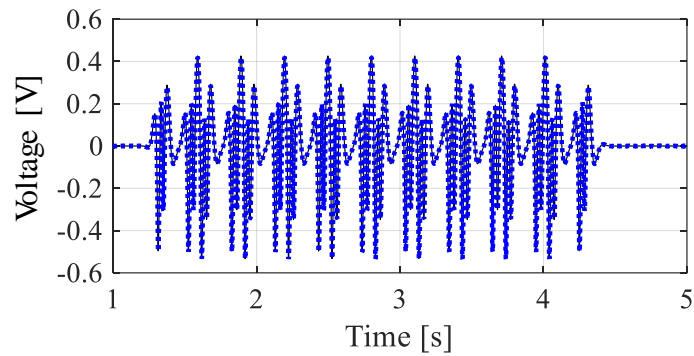
and calculating the integral from $t_0 = 1.1$ s to $t_f = 8.25$ s for a train with the speed of 117.3 km/h and from $t_0 = 1.3$ s to $t_f = 4.47$ s for a train with the speed of 273.5 km/h, the total harvested energy by the Geophone SM-24 is given in Tab. 15.

Figure 55. The voltage across the optimum load resistance, $R_{l,eq} = 1903 \Omega$, when the energy harvester is subjected to the sleeper vertical vibration induced due to an Inter-city 125 train passing with the speed of 117.3 km/h. The black solid line (—) is the voltage predicted by the numerical investigation and the blue dotted line (.....) is the measured.



Source: author.

Figure 56. The voltage across the optimum load resistor, $R_{l,eq} = 1173 \Omega$, when the energy harvester is subjected to the sleeper vertical vibration induced due to an Inter-city 125 train passing with the speed of 273.5 km/h. The black solid line (—) is the voltage predicted by the numerical investigation and the blue dotted line (.....) is the measured.



Source: author.

Table 15 – The harvested energy by the linear electromagnetic transducer subject to the sleeper vibration due to a passing train emulated in a laboratory-based system.

Train speed [km/h]	Target trainload frequency	$E_{elec,meas}$ [μ J]	R_l [Ω]	$E_{elec,predict}$ [μ J]	$R_{l,opt}$ [Ω]
117.2	7 th	19.3	1903	19.7	1944
273.47	3 rd	113.3	1173	116.2	1144

Source: author.

It can be seen in Figs. 55 and 56 that the measured voltages across the equivalent load resistances are similar to the voltages predicted by the numerical model. Moreover, it is shown

in Tab. 15, that the total harvested energies are approximately the same to those predicted by the numerical model. The small differences observed are believed to be due to the emulation of the sleeper vibration on the electromagnetic shaker, which is not precise, and due to the small difference between the required load resistance and that used.

From the sleeper vibration induced due the passage of an Inter-city 125 train travelling at Steventon site with a speed of 117.3 km/h, whose the 7th trainload frequency coincides with the transducer undamped natural frequency, the Geophone SM-24 with a load resistance of $R_{l,eq} = 1903 \Omega$ was able to harvest 19.3 μJ of energy. Due to the passage of the Inter-city 125 with a speed of 273.5 km/h, the Geophone SM-24 with a load resistance of $R_{l,eq} = 1173 \Omega$ was able to harvest 113.3 μJ of energy.

5.5 CONCLUSIONS

This Chapter has investigated the linear electromagnetic energy harvester to scavenge energy from the sleeper vibration induced due to a passing train. It was found that the maximum energy is harvested when the transducer equivalent damping ratio is set to be very small and its natural frequency coincides with the frequency where there is the largest acceleration. However, if the equivalent damping ratio is high, the device may be operating in a different regime than the transient and its best performance may occur at a natural frequency different from the frequency with the largest acceleration amplitude. Moreover, it was shown that the harvested energy is directly proportional to the size of the suspended mass. However, the increase in mass increases the dissipated energy by the internal coil resistance and also increases the maximum relative displacement, which may be a limiting factor to the transducer.

Additionally, in this Chapter, an experimental setup was proposed to harvest the energy from the sleeper vibration induced due to a passing train emulated on a laboratory-based system with the aim to validate the energy harvester model. The sleeper vibration induced due to an Inter-city 125 train passing at Steventon site with the speeds of 117.3 km/h and 273.5 km/h were emulated on an electromagnetic shaker and used to excite the base of a Geophone SM-24, used as the energy harvester transducer. The experimental results were found to be approximately the same as the results found numerically. For the energy harvester subjected by the vibration induced due to the train with the speed of 117.3 km/h, it was found that a load resistance of 1903 Ω was able to harvest 19.3 μJ of energy. For the energy harvester subjected

by the vibration induced due to the train with the speed of 273.5 km/h, it was found that a load resistance of 1173 Ω was able to harvest 113.3 μJ of energy.

6 FINAL REMARKS

This thesis has presented a study into the harvesting of energy from sleeper vibration due to a passing train. It consists of six chapters, the summaries of which are given below. The detailed conclusions are given at the end of each chapter, and these are also summarised in this chapter.

Chapter 2 described an investigation into why the highest amplitude of the sleeper vertical acceleration due to the passage of a train is generally the 7th trainload frequency. A simple infinite Euler-Bernoulli beam resting on a Winkler foundation has been used to develop the quasi-static model of a train moving along a track in the time and frequency domains.

A general conclusion from the work in Chapter 2 is that the spectrum due to the passage of one wheel is only dependent on the track features which act as a bandpass filter, restricting the quasi-static vibration at low frequencies. However, it is the wheel spacing in a bogie that is of particular importance, as this partitions the bandpass filter effect into two frequency ranges, and in general, it is the highest of these ranges in which the largest acceleration amplitude occurs. In the case of an extremely soft track support stiffness then it is possible, in principle at least, for the largest amplitude to occur below the 4th trainload frequency, typically at the 3rd.

Chapter 3 described an investigation to determine the best electromechanical transducer to harvest the low excitation frequencies, induced due to a passing train, and an approximate analytical model for the energy dissipated by the load resistance attached to the transducer. A two-port network model was used to characterize the linear SDOF mass-spring-damper electromagnetic and piezoelectric energy harvesters. It was found, from a simple comparison, that at low frequency the electromagnetic transducer has a better performance than the piezoelectric transducer.

An approximate analytical model for the energy dissipated by the load resistance attached to an electromagnetic transducer due to time-limited excitation has been derived by incorporating the analogous electrical dampers into the equation found in (Gatti *et al.* 2016) and used to investigate the optimum load resistance. In general, it was shown that the mechanical damping and the internal coil resistance has a detrimental effect to reduce the harvester performance. In order to harvest the maximum energy introduced from the vibrating source, an ideal transducer, i.e., with no mechanical damping and no internal coil resistance, with a small load resistance damping ratio (large load resistance) is required.

Chapter 4 has investigated the replication of the sleeper vertical vibration, induced due to the passage of a train, in a laboratory-based system. A methodology to design, in the time domain, a filter which removes the dynamics of the system in which the filter is applied was presented and a laboratory-based system to emulate the sleeper vertical vibration in the electrodynamic shaker was proposed. The experimental test showed good agreement between the desirable and the measured time waveforms. In addition, it has been shown that the lower frequency of actuation of the compensator filter is of 3 Hz, which allowed the 7th trainload frequency of the sleeper vibration induced by slowest trains capable to be replicated.

Chapter 5 has investigated, numerically and analytically, the performance of a linear electromagnetic energy harvester when subjected to the sleeper vibration, induced due to a passing train, into determining the device optimum parameters and the total harvested energy.

In general, the analytical investigation showed similar results as the numerical. It was found that the transducer maximum performance occurs with the device operating in the transient regime and the maximum energy harvested by the load resistance occurs when the transducer is tuned to the frequency with the largest acceleration amplitude. The optimal load resistance damping ratio was found to be small, which result in large load resistance. It was shown that more energy is harvested for a larger mass. It was also shown that the internal coil resistance has a detrimental effect to reduce the harvester efficiency and its effect is more pronounced when the size of the suspended mass is large. When the mechanical damping is high, it was shown that the transducer is no longer in the transient regime and the load resistance harvest the maximum energy when the transducer is tuned to the frequency with the largest velocity amplitude. The energy harvester model was validated using a geophone electromagnetic transducer to harvest the energy from the sleeper vertical vibration induced by a passing train emulated in a laboratory-based system.

6.1 RECOMMENDATION FOR FUTURE WORK

From the studies and conclusions presented in this thesis, the following future work may be suggested:

- To design a prototype of a linear electromagnetic energy harvesting device with small mechanical damping to fully validate the energy harvester model;

- To investigate the effects of introducing an electrical circuit to convert the alternating current to the direct current and determine how much energy can be stored from the sleeper vibration induced due to a passing train;
- To develop a statistical model to predict the railway speed line trends to investigate the robustness of the energy harvester;
- To improve the laboratory-based system by reducing the lowest frequency of actuation which would allow the sleeper vertical vibration waveform induced by slowest trains able to be replicated;
- To investigate the non-linearity in transducers to broadband the device target frequency improving the energy harvester performance.

REFERENCES

- AHMADIZADEH, M.; MOSQUEDA, G.; REINHORN, A. M. Compensation of actuator delay and dynamics for real-time hybrid structural simulation. **Earthquake Engineering & Structural Dynamics**, Oxford, v. 37, n. 1, p. 21–42, 2008.
- AMIN KARAMI, M.; INMAN, D. J. Powering pacemakers from heartbeat vibrations using linear and nonlinear energy harvesters. **Applied Physics Letters**, Melville, v. 100, n. 4, p. 042901, 2012.
- AMIRTHARAJAH, R.; CHANDRAKASAN, A. P. Self-powered signal processing using vibration-based power generation. **IEEE Journal of Solid-State Circuits**, Piscataway, v. 33, n. 5, p. 687–695, 1998.
- ANTON, S. R.; SODANO, H. A. A review of power harvesting using piezoelectric materials (2003–2006). **Smart Materials and Structures**, Bristol, v. 16, n. 3, p. R1, 2007.
- AUERSCH, L. The excitation of ground vibration by rail traffic: theory of vehicle–track–soil interaction and measurements on high-speed lines. **Journal of Sound and Vibration**, London, v. 284, n. 1–2, p. 103–132, 2005.
- AUERSCH, L. Ground vibration due to railway traffic—The calculation of the effects of moving static loads and their experimental verification. **Journal of Sound and Vibration**, London, v. 293, n. 3, p. 599–610, 2006.
- AVCI, O.; ABDELJABER, O.; KIRANYAZ, S.; HUSSEIN, M.; INMAN, D. J. Wireless and real-time structural damage detection: a novel decentralized method for wireless sensor networks. **Journal of Sound and Vibration**, London, v. 424, p. 158–172, 2018.
- BLOOMBERGNEF. **Global electricity demand to increase 57% by 2050**. [s. l.], 2018. Available in: <https://about.bnef.com/blog/global-electricity-demand-increase-57-2050/>. Access in: Oct. 12, 2019.
- BRENNAN, M. J.; GATTI, G. Harvesting energy from time-limited harmonic vibrations: mechanical considerations. **Journal of Vibration and Acoustics**, New York, v. 139, n. 5, p. 051019-051019–6, 2017a.
- BRENNAN, M. J.; GATTI, G. Harvesting energy from time-limited harmonic vibrations: mechanical considerations. **Journal of Vibration and Acoustics**, New York, v. 139, n. 5, p. 051019, 2017b.
- CHEN, C.; RICLES, J. M. Analysis of actuator delay compensation methods for real-time testing. **Engineering Structures**, Oxford, v. 31, n. 11, p. 2643–2655, 2009.
- CLEANTE, V. G.; BRENNAN, M. J.; GATTI, G.; THOMPSON, D. J. Energy harvesting from the vibrations of a passing train: effect of speed variability. **Journal of Physics: Conference Series**, Bristol, v. 744, p. 012080, 2016.
- CLEANTE, V. G.; BRENNAN, M. J.; GATTI, G.; THOMPSON, D. J. On the target frequency for harvesting energy from track vibrations due to passing trains. **Mechanical Systems and Signal Processing**, London, v. 114, p. 212–223, 2019.
- CORNELIS, B.; TOSO, A.; VERPOEST, W.; PEETERS, B. **Improved MIMO FRF estimation and model updating for robust Time Waveform Replication on durability test rigs**. 16 p., 2014. Available in: http://past.isma-isaac.be/downloads/isma2014/papers/isma2014_0704.pdf. Access in: Nov. 26, 2019.

DAGDEVIREN, C.; YANG, B. D.; SU, Y.; TRAN, P. L.; JOE, P.; ANDERSON, E.; XIA, J.; DORAISWAMY, V.; DEHDASHTI, B.; FENG, X.; LU, B.; POSTON, R.; KHALPEY, Z.; GHAFFARI, R.; HUANG, Y.; SLEPIAN, M. J.; ROGERS, J. A. Conformal piezoelectric energy harvesting and storage from motions of the heart, lung, and diaphragm. **Proceedings of the National Academy of Sciences**, Washington, v. 111, n. 5, p. 1927–1932, 2014.

DAL BO, L.; GARDONIO, P. Energy harvesting with electromagnetic and piezoelectric seismic transducers: Unified theory and experimental validation. **Journal of Sound and Vibration**, London, v. 433, p. 385–424, 2018.

DE PASQUALE, G.; SOMÀ, A.; ZAMPIERI, N. Design, simulation, and testing of energy harvesters with magnetic suspensions for the generation of electricity from freight train vibrations. **Journal of Computational and Nonlinear Dynamics**, New York, v. 7, n. 4, p. 041011, 2012.

ERTURK, A.; INMAN, D. J. An experimentally validated bimorph cantilever model for piezoelectric energy harvesting from base excitations. **Smart Materials and Structures**, Bristol, v. 18, n. 2, p. 025009, 2009.

FRÝBA, L. **Vibration of solids and structures under moving loads**. London: Thomas Telford, 1999. 494 p.

GANG, S.; ZHENG, S.-T.; YE, Z.-M.; HUANG, Q.-T.; CONG, D.-C.; HAN, J.-W. Adaptive inverse control of time waveform replication for electrohydraulic shaking table. **Journal of Vibration and Control**, London, v. 17, n. 11, p. 1611–1633, 2011.

GAO, M.; LI, Y.; LU, J.; WANG, Y.; WANG, P.; WANG, L. Condition monitoring of urban rail transit by local energy harvesting. **International Journal of Distributed Sensor Networks**, Thousand Oaks, v. 14, n. 11, 16 p., 2018. Available in: <https://journals.sagepub.com/doi/full/10.1177/1550147718814469>. Access in: Nov. 26, 2019.

GAO, M.; WANG, P.; CAO, Y.; CHEN, R.; CAI, D. Design and verification of a rail-borne energy harvester for powering wireless sensor networks in the railway industry. **IEEE Transactions on Intelligent Transportation Systems**, Piscataway, v. 18, n. 6, p. 1596–1609, 2017.

GAO, M. Y.; WANG, P.; CAO, Y.; CHEN, R.; LIU, C. **A rail-borne piezoelectric transducer for energy harvesting of railway vibration**. Research article. 2016. Available in: <https://www.jvejournal.com/article/16938>. Access in: Jan. 17, 2019.

GATTI, G.; BRENNAN, M. J.; TEHRANI, M. G.; THOMPSON, D. J. Harvesting energy from the vibration of a passing train using a single-degree-of-freedom oscillator. **Mechanical Systems and Signal Processing**, London, v. 66–67, p. 785–792, 2016.

GRASSIE, S. L.; GREGORY, R. W.; HARRISON, D.; JOHNSON, K. L. The dynamic response of railway track to high frequency vertical excitation. **Journal of Mechanical Engineering Science**, London, v. 24, n. 2, p. 77–90, 1982.

GREENRAIL. **Greenrail company**. 2020. Available in: <http://www.greenrailgroup.com/en/home/>. Access in: Nov. 26, 2019.

HADAS, Z.; SMILEK, J.; RUBES, O. Energy harvesting from passing train as source of energy for autonomous trackside objects. **MATEC Web of Conferences**, [s. l.], v. 211, p. 05003, 2018. Available In: https://www.researchgate.net/publication/328195720_Energy_harvesting_from_passing_train_as_source_of_energy_for_autonomous_trackside_objects. Access: Oct. 26, 2019.

HANSEN, S. E.; POURGHODRAT, A.; NELSON, C. A.; FATEH, M. On-track testing of a power harvesting device for railroad track health monitoring. *In: HEALTH MONITORING OF STRUCTURAL AND BIOLOGICAL SYSTEMS*, 2010. : International Society for Optics and Photonics, 2010, San Diego. **Proceedings of the [...]**. San Diego: SPIE, 2010. Available in: <https://www.spiedigitallibrary.org/conference-proceedings-of-spie/7650/76500Y/On-track-testing-of-a-power-harvesting-device-for-railroad/10.1117/12.848831.short>. Access in: Jan. 21, 2019.

HARMS, T.; SEDIGH, S.; BASTIANINI, F. Structural health monitoring of bridges using wireless sensor networks. **IEEE Instrumentation & Measurement Magazine**, Piscataway, v. 13, n. 6, p. 14–18, 2010.

HARRIS, C. M.; PIERSOL, A. G. **Harris' shock and vibration handbook**. [Michigan] : McGraw-Hill, 2002. 1568 p.

HEMOUR, S.; ZHAO, Y.; LORENZ, C. H. P.; HOUSSAMEDDINE, D.; GUI, Y.; HU, C.-M.; WU, K. Towards low-power high-efficiency RF and microwave energy harvesting. **IEEE Transactions on Microwave Theory and Techniques**, Piscataway, v. 62, n. 4, p. 965–976, 2014.

HIROKANE, J.; SAGA, T.; MURAMATSU, T.; SHIRAKAWA, I. History of contribution of photovoltaic cells to telecommunications. *In: SECOND REGION 8 IEEE CONFERENCE ON THE HISTORY OF COMMUNICATIONS*, 2010, Madrid. **Proceedings of the [...]**. Madrid: IEEE, 2010. 6 p.

HU, X.; WANG, B.; JI, H. A wireless sensor network-based structural health monitoring system for highway bridges: a wireless sensor network-based SHM system for highway bridges. **Computer-Aided Civil and Infrastructure Engineering**, Hoboken, v. 28, n. 3, p. 193–209, 2013.

IANNACCI, J. **RF-MEMS technology for high-performance passives: the challenge of 5G mobile applications**. Available in: <https://iopscience.iop.org/book/978-0-7503-1545-6>. Access in: Nov. 8, 2019.

ION PRODUCTS. **Sensor geophones**, ION, 2009. Available in: http://www.iongeo.com/virtuals/ResourceArchives/content/documents/Resource%20Center/Brochures%20and%20Data%20Sheets/Brochures/BR_SEN_Geophones_091509.pdf. Access in: 12 out. 2019.

IWANAGA, M.; BRENNAN, M.; SCUSSEL, O.; ALMEIDA, F. On the design of a digital filter to compensate for the shaker dynamics in a virtual pipe test rig. *In: INTERNATIONAL SYMPOSIUM IN PROBLEMS OF MECHANICS, DINAME2019*, 15, 2019, Búzios. **Conference of the [...]** Búzios: ABCM, 2019. Available in: <http://abcm.org.br/anais-de-eventos/DIN2019/0159>. Access in: Set. 8, 2019.

JIA, D.; LIU, J. Human power-based energy harvesting strategies for mobile electronic devices. **Frontiers of Energy and Power Engineering in China**, Beijing, v. 3, n. 1, p. 27–46, 2009.

JU, S.-H.; LIN, H.-T.; HUANG, J.-Y. Dominant frequencies of train-induced vibrations. **Journal of Sound and Vibration**, London, v. 319, n. 1, p. 247–259, 2009.

KHALIGH, A.; ONAR, O. C. **Energy harvesting: solar, wind, and ocean energy conversion systems**. Boca Raton: CRC Press, 2010.

KNOTHE, K.; GRASSIE, S. L. Modelling of railway track and vehicle/track interaction at high frequencies. **Vehicle System Dynamics**, Abingdon, v. 22, n. 3–4, p. 209–262, 1993.

- KULAH, H.; NAJAFI, K. Energy scavenging from low-frequency vibrations by using frequency up-conversion for wireless sensor applications. **IEEE Sensors Journal**, Piscataway, v. 8, n. 3, p. 261–268, 2008.
- LE PEN, L.; MILNE, D.; THOMPSON, D.; POWRIE, W. Evaluating railway track support stiffness from trackside measurements in the absence of wheel load data. **Canadian Geotechnical Journal**, Ottawa, v. 53, n. 7, p. 1156–1166, 2016.
- LI, J.; JANG, S.; TANG, J. Design of a bimorph piezoelectric energy harvester for railway monitoring. **Journal of the Korean Society for Nondestructive Testing**, Seoul, v. 32, n. 6, p. 661–668, 2012.
- LI, J.; JANG, S.; TANG, J. **Implementation of a piezoelectric energy harvester in railway health monitoring**. 2014a. Available in: <https://www.spiedigitallibrary.org/conference-proceedings-of-spie/9061/90612Q/Implementation-of-a-piezoelectric-energy-harvester-in-railway-health-monitoring/10.1117/12.2045224.short>. Access in: Fev. 24, 2018.
- LI, J.; JANG, S.; TANG, J. **Implementation of a piezoelectric energy harvester in railway health monitoring**. 2014b. Available in: <https://www.spiedigitallibrary.org/conference-proceedings-of-spie/9061/90612Q/Implementation-of-a-piezoelectric-energy-harvester-in-railway-health-monitoring/10.1117/12.2045224.short>. Access in: Jan. 17, 2019.
- LIN, T.; PAN, Y.; CHEN, S.; ZUO, L. Modeling and field testing of an electromagnetic energy harvester for rail tracks with anchorless mounting. **Applied Energy**, Oxford, v. 213, p. 219–226, 2018.
- LIN, T.; WANG, J. J.; ZUO, L. Efficient electromagnetic energy harvester for railroad transportation. **Mechatronics**, Oxford, v. 53, p. 277–286, 2018.
- LOMBAERT, G.; DEGRANDE, G. Ground-borne vibration due to static and dynamic axle loads of InterCity and high-speed trains. **Journal of Sound and Vibration**, London, v. 319, n. 3–5, p. 1036–1066, 2009.
- LU, X.; FLINT, I.; NIYATO, D.; PRIVAULT, N.; WANG, P. Performance analysis of simultaneous wireless information and power transfer with ambient RF energy harvesting. *In: IEEE WIRELESS COMMUNICATIONS AND NETWORKING CONFERENCE - WCNC, 2015, New Orleans. Proceedings of the [...]* New Orleans: IEEE 2015. p. 1303-1308.
- LYNCH, J. P. A summary review of wireless sensors and sensor networks for structural health monitoring. **The Shock and Vibration Digest**, Thousand, v. 38, n. 2, p. 91–128, 2006.
- MARIAN, V.; ALLARD, B.; VOLLAIRE, C.; VERDIER, J. Strategy for microwave energy harvesting from ambient field or a feeding source. **IEEE Transactions on Power Electronics**, Piscataway, v. 27, n. 11, p. 4481–4491, 2012.
- MIAN, Z. F. **Wireless railroad monitoring**. Troy: International Electronic Machines Corporation, 2013. US 8,423,240 B2. Depositor: 29 jun. 2009. Concession: 16 abr. 2013. Available in: <https://patents.google.com/patent/US8423240B2/en>. Access in: Out. 20, 2019.
- MIAO, P.; MITCHESON, P. D.; HOLMES, A. S.; YEATMAN, E. M.; GREEN, T. C.; STARK, B. H. Mems inertial power generators for biomedical applications. **Microsystem Technologies**, Heidelberg, v. 12, n. 10, p. 1079–1083, 2006.
- MILNE, D. R. M.; LE PEN, L. M.; THOMPSON, D. J.; POWRIE, W. Properties of train load frequencies and their applications. **Journal of Sound and Vibration**, London, v. 397, p. 123–140, 2017.

MORAIS, R.; MATOS, S. G.; FERNANDES, M. A.; VALENTE, A. L. G.; SOARES, S. F. S. P.; FERREIRA, P. J. S. G.; REIS, M. J. C. S. Sun, wind and water flow as energy supply for small stationary data acquisition platforms. **Computers and Electronics in Agriculture**, Amsterdam, v. 64, n. 2, p. 120–132, 2008.

NAKANO, K.; ELLIOTT, S. J.; RUSTIGHI, E. A unified approach to optimal conditions of power harvesting using electromagnetic and piezoelectric transducers. **Smart Materials and Structures**, Bristol, v. 16, n. 4, p. 948–958, 2007.

NELSON, C. A.; PLATT, S. R.; ALBRECHT, D.; KAMARAJUGADDA, V.; FATEH, M. Power harvesting for railroad track health monitoring using piezoelectric and inductive devices. *In: ACTIVE AND PASSIVE SMART STRUCTURES AND INTEGRATED SYSTEMS*, 2008, San Diego. **Proceedings of the [...]**. San Diego: International Society for Optics and Photonics, 2008. Available in: <https://www.spiedigitallibrary.org/conference-proceedings-of-spie/6928/69280R/Power-harvesting-for-railroad-track-health-monitoring-using-piezoelectric-and/10.1117/12.775884.short>. Access in: Jan. 17, 2019.

NELSON, C. A.; PLATT, S. R.; HANSEN, S. E.; FATEH, M. **Power harvesting for railroad track safety enhancement using vertical track displacement**. Available in: <http://proceedings.spiedigitallibrary.org/proceeding.aspx?doi=10.1117/12.815544>. Access in: Oct. 20, 2019.

PAN, Y.; LIN, T.; QIAN, F.; LIU, C.; YU, J.; ZUO, J.; ZUO, L. Modeling and field-test of a compact electromagnetic energy harvester for railroad transportation. **Applied Energy**, Oxford, v. 247, p. 309–321, 2019.

POBERING, S.; SCHWESINGER, N. A novel hydropower harvesting device. *In: INTERNATIONAL CONFERENCE ON MEMS, NANO AND SMART SYSTEMS, ICMENS*, 2004, Canada. **Proceedings of the [...]**. Canada: IEEE, 2004. 6 f. Available in: <https://ieeexplore.ieee.org/stamp/stamp.jsp?tp=&arnumber=1508997>. Access in: Nov. 27, 2019.

POURGHODRAT, A.; NELSON, C. A.; HANSEN, S. E.; KAMARAJUGADDA, V.; PLATT, S. R. Power harvesting systems design for railroad safety. **Proceedings of the Institution of Mechanical Engineers, Part F: Journal of Rail and Rapid Transit**, London, v. 228, n. 5, p. 504–521, 2014.

POURGHODRAT, A.; NELSON, C. A.; PHILLIPS, K. J.; FATEH, M. Improving an energy harvesting device for railroad safety applications. *In: ACTIVE AND PASSIVE SMART STRUCTURES AND INTEGRATED SYSTEMS*, 2011, San Diego. **Proceedings of the [...]**. San Diego: Spie, 2011. Available in: <https://www.spiedigitallibrary.org/conference-proceedings-of-spie/7977/79770U/Improving-an-energy-harvesting-device-for-railroad-safety-applications/10.1117/12.880631.short>. Access in: Jan. 17, 2019.

PRIEST, J. A.; W. POWRIE. Determination of dynamic track modulus from measurement of track velocity during train passage. **Journal of Geotechnical and Geoenvironmental Engineering**, Reston, v. 135, n. 11, p. 1732–1740, 2009.

RAO, S. S. **Mechanical vibrations**. 5. ed. Upper Saddle River: Pearson, 2010.

ROUNDY, S. On the Effectiveness of Vibration-based Energy Harvesting. **Journal of Intelligent Material Systems and Structures**, London, v. 16, n. 10, p. 809–823, 2005.

ROUNDY, S.; WRIGHT, P. K.; RABAEY, J. A study of low level vibrations as a power source for wireless sensor nodes. **Computer Communications**, Amsterdam, v. 26, n. 11, p. 1131–1144, 2003.

SAHA, C. R.; O'DONNELL, T.; WANG, N.; MCCLOSKEY, P. Electromagnetic generator for harvesting energy from human motion. **Sensors and Actuators A: Physical**, Amsterdam, v. 147, n. 1, p. 248–253, 2008.

SARI, I.; BALKAN, T.; KULAH, H. A wideband electromagnetic micro power generator for wireless microsystems. *In: INTERNATIONAL SOLID-STATE SENSORS, ACTUATORS AND MICROSYSTEMS CONFERENCE, TRANSDUCERS, 2007, Lyon. Proceedings of the [...].* Lyon: IEEE, 2007. p. 275-278.

SHEN, G.; ZHU, Z.; LI, X.; LI, G.; TANG, Y.; LIU, S. Experimental evaluation of acceleration waveform replication on electrohydraulic shaking tables: a review. **International Journal of Advanced Robotic Systems**, London, v. 13, n. 5, 25 p., 2016.

SHEN, G.; ZHU, Z.-C.; LI, X.; WANG, Q.-G.; LI, G.; TANG, Y. Acceleration waveform replication on six-degree-of-freedom redundant electro-hydraulic shaking tables using an inverse model controller with a modelling error. **Transactions of the Institute of Measurement and Control**, London, v. 40, n. 3, p. 968–986, 2018.

SHENG, X.; JONES, C. J. C.; PETYT, M. Ground vibration generated by a load moving along a railway track. **Journal of Sound and Vibration**, London, v. 228, n. 1, p. 129–156, 1999.

SHENG, X.; JONES, C. J. C.; THOMPSON, D. J. A comparison of a theoretical model for quasi-statically and dynamically induced environmental vibration from trains with measurements. **Journal of Sound and Vibration**, London, v. 267, n. 3, p. 621–635, 2003.

SHENG, X.; JONES, C. J. C.; THOMPSON, D. J. A theoretical study on the influence of the track on train-induced ground vibration. **Journal of Sound and Vibration**, London, v. 272, n. 3–5, p. 909–936, 2004.

SHIN, K.; HAMMOND, J. K. **Fundamentals of signal processing for sound and vibration engineers**. Chichester: John Wiley & Sons, 2008.

STEPHEN, N. G. On energy harvesting from ambient vibration. **Journal of Sound and Vibration**, London, v. 293, n. 1–2, p. 409–425, 2006a.

STEPHEN, N. G. On the maximum power transfer theorem within electromechanical systems. **Proceedings of the Institution of Mechanical Engineers, Part C: Journal of Mechanical Engineering Science**, London, v. 220, n. 8, p. 1261–1267, 2006b.

TAN, H.-P.; LEE, P. W. Q.; SEAH, W. K. G.; EU, Z. A. Impact of power control in wireless sensor networks powered by ambient energy harvesting (WSN-HEAP) for railroad health monitoring. *In: INTERNATIONAL CONFERENCE ON ADVANCED INFORMATION NETWORKING AND APPLICATIONS WORKSHOPS, 2009, Bradford. Proceedings of the [...].* Bradford: IEEE, 2009. Available in: <http://ieeexplore.ieee.org/document/5136748/>. Access in: Oct. 20, 2019.

THOMPSON, D. **Railway noise and vibration: mechanisms, modelling and means of control**. [S.l.]: Elsevier, 2008.

TIANCHEN, Y.; JIAN, Y.; RUIGANG, S.; XIAOWEI, L. Vibration energy harvesting system for railroad safety based on running vehicles. **Smart Materials and Structures**, Bristol, v. 23, n. 12, p. 125046, 2014.

TRIEPAISCHAJONSAK, N. **The influence of various excitation mechanisms on ground vibration from trains**. 2012. Thesis (Doctor PHD) - University of Southampton, Southampton, 2012. Available in: <https://eprints.soton.ac.uk/348966/>. Access in: Feb. 24, 2018.

TRIEPAISCHAJONSAK, N.; THOMPSON, D. J.; JONES, C. J. C.; RYUE, J.; PRIEST, J. A. Ground vibration from trains: experimental parameter characterization and validation of a numerical model. **Proceedings of the Institution of Mechanical Engineers, Part F: Journal of Rail and Rapid Transit**, London, v. 225, n. 2, p. 140–153, 2011.

ULIANOV, C.; HADAŠ, Z.; HYDE, P.; SMILEK, J. Novel energy harvesting solutions for powering trackside electronic equipment. *In*: MARINOV, M.; PIIP, J. (ed.). **Sustainable rail transport**. Cham: Springer International Publishing, 2020. p. 229–255.

WANG, J.; LIN, T.; ZUO, L. High efficiency electromagnetic energy harvester for railroad application. *In*: DESIGN FOR MANUFACTURING AND THE LIFE CYCLE CONFERENCE, 18, ASME/IEEE INTERNATIONAL CONFERENCE ON MECHATRONIC AND EMBEDDED SYSTEMS AND APPLICATIONS 2013, Portland. **Proceedings of the [...]**. Portland: 2013. V. 4. Available in: <https://asmedigitalcollection.asme.org/IDETC-CIE/proceedings/IDETC-CIE2013/55911/Portland,%20Oregon,%20USA/256087>. Access in: Nov. 12, 2019.

WANG, J.; SHI, Z.; XIANG, H.; SONG, G. Modeling on energy harvesting from a railway system using piezoelectric transducers. **Smart Materials and Structures**, Bristol, v. 24, n. 10, 14 p., 2015. Available in: <https://iopscience.iop.org/article/10.1088/0964-1726/24/10/105017/pdf>. Access in: Nov. 27, 2019.

WANG, P.; WANG, Y. F.; GAO, M. Y.; WANG, Y. Energy harvesting of track-borne transducers by train-induced wind. **Journal of Vibroengineering**, Kaunas, v. 19, n. 3, p. 1624–1640, 2017.

WANG, P.; YANG, F.; GAO, M.; WANG, Y. Study on an elastic lever system for electromagnetic energy harvesting from rail vibration. **Journal of Vibroengineering**, Kaunas, v. 21, n. 2, p. 384–395, 2019.

WILLIAMS, C. B.; YATES, R. B. Analysis of a micro-electric generator for microsystems. **Sensors and Actuators A: Physical**, Amsterdam, v. 52, 1-3, p. 8–11, 1996.

WISCHKE, M.; MASUR, M.; KRÖNER, M.; WOIAS, P. Vibration harvesting in traffic tunnels to power wireless sensor nodes. **Smart Materials and Structures**, Bristol, v. 20, n. 8, 9 p., 2011. Available in: <https://iopscience.iop.org/article/10.1088/0964-1726/20/8/085014/pdf>. Access in: Nov. 27, 2019.

WOOLLETT, R. S. Effective coupling factor of single-degree-of-freedom transducers. **The Journal of the Acoustical Society of America**, Melville, v. 40, n. 5, p. 1112–1123, 1966.

YAO, J.; WAN, Z.; ZHAO, Y.; YU, J.; QIAN, C.; FU, Y. Resonance suppression for hydraulic servo shaking table based on adaptive notch filter. **Shock and Vibration**, New York, v. 2019, p. 1–12, 2019.

YI, J. W.; SHIH, W. Y.; SHIH, W.-H. Effect of length, width, and mode on the mass detection sensitivity of piezoelectric unimorph cantilevers. **Journal of Applied Physics**, Melville, v. 91, n. 3, p. 1680–1686, 2002.

YI, S.; YANG, B.; MENG, G. Ill-conditioned dynamic hysteresis compensation for a low-frequency magnetostrictive vibration shaker. **Nonlinear Dynamics**, Dordrecht, v. 96, n. 1, p. 535–551, 2019.

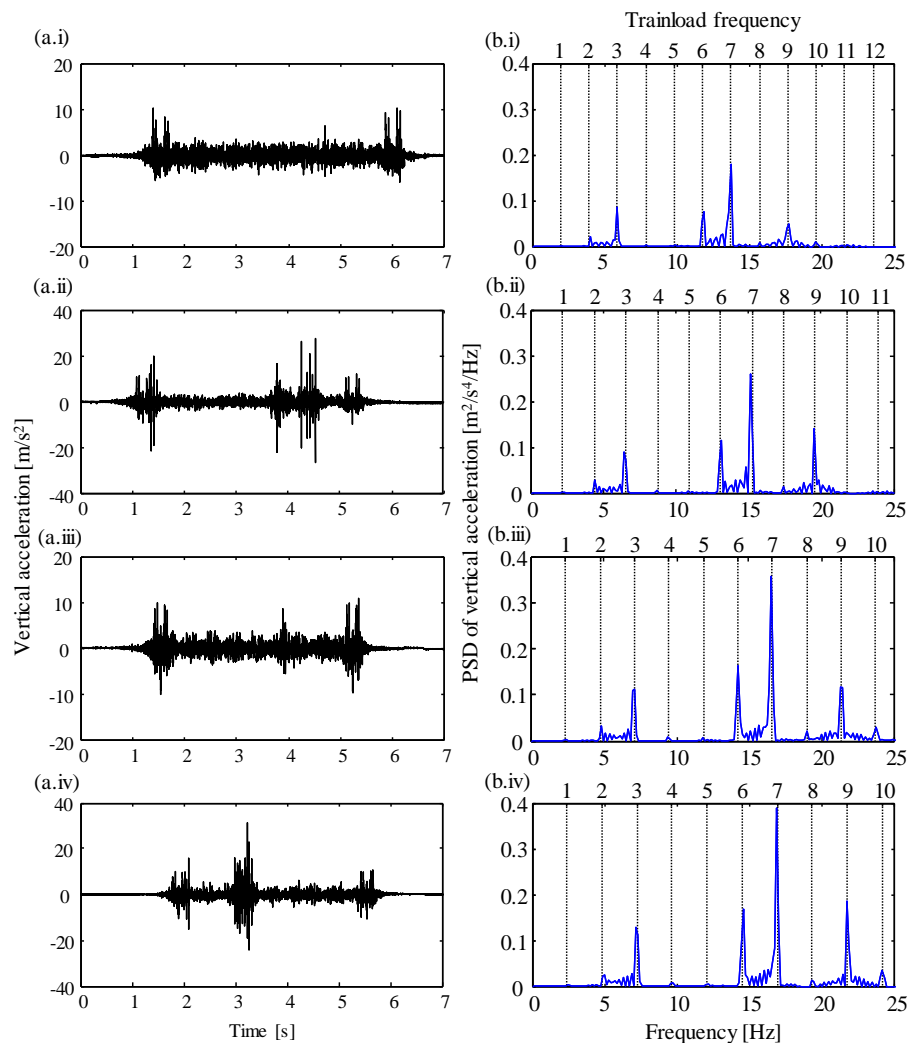
YUN, C. B.; LOU, Y. Z.; DUAN, Y. F.; TANG, Z. F. Smart monitoring and assessment for safe and resilient civil infrastructure. *In*: AUSTRALASIAN CONFERENCE ON THE MECHANICS OF STRUCTURES AND MATERIALS, ACMMS, 25, 2018, Brisbane. **Proceedings of the [...]**. Brisbane: Springer Singapore, 2020. p. 931–940.

ZHANG, X.; ZHANG, Z.; PAN, H.; SALMAN, W.; YUAN, Y.; LIU, Y. A portable high-efficiency electromagnetic energy harvesting system using supercapacitors for renewable energy applications in railroads. **Energy Conversion and Management**, London, v. 118, p. 287–294, 2016.

APPENDIX A

In this appendix, the set of sleeper vertical acceleration measurements induced by an Inter-city 125 composed of 2 power cars and 8 passenger cars passing at speeds of 162 km/h, 178 km/h, 195 km/h and 200 km/h, is presented. The time-histories and the power spectral densities are shown in Fig. A1(a) and (b) respectively. At the top of Figs. A1(b) there is another axis representing the trainload frequencies, i.e. the frequency normalized by the ratio between length of the carriage and the train speed.

Figure A1. Sleeper vertical acceleration (a) time-history; and (b) Power Spectral Density (at the top there is another axis corresponding to frequency normalized by the ratio between train speed and passenger carriage) due to the passage of an Inter-city 125 at different speeds: (i) 162 km/h; (ii) 178 km/h; (iii) 195 km/h; and (iv) 200 km/h.



Source: author.